Dynamics of Convergent Migration and Mean Motion Resonances in Planetary Systems

by

Jacob A. Ketchum

A dissertation submitted in partial fulfillment
of the requirements for the degree of
Doctor of Philosophy
(Physics)
in The University of Michigan
2014

Doctoral Committee:

Professor Fred C. Adams, Co-Chair
Professor Anthony M. Bloch, Co-Chair
Professor Dante E. Amedei
Professor August Evrard
Professor Lee W. Hartmann
Professor James T. Liu

To Becca and Sammy

ACKNOWLEDGEMENTS

I am extremely fortunate to have had the support, encouragement, and/or patience from the following people throughout my life, which ultimately made this thesis possible:

First and foremost; Thank you Fred: You have been everything and more than anybody could ever ask for in a mentor and a friend. You believed in me even when it was difficult for me to believe in myself. What you have done for me, I am forever in your debt.

Thanks Tony: You have helped me understand mechanics and dynamics on a much deeper level than I ever thought possible.

Thanks to my committee members for crucial feedback, comments, and useful discussions that served to improve this thesis.

Thanks to my freshman physics professor, Alex Azima, for fostering the budding physicist in me and teaching me how to really use calculus.

Thanks to my brother, Scott Ketchum, for introducing me to some interesting philosophical aspects concerning physics. This really provided the spark in curiosity that led to my pursuit of a formal education in physics.

Thanks to my parents for allowing me to discover myself and to pursue my own interests.

Thanks to my friends and colleagues for keeping me grounded.

And last, but certainly not least, I am forever grateful for my wife, Becca, with her unconditional love, support, and patience. I couldn't have done this without you.

TABLE OF CONTENTS

LIST OF FIGURES

Figure

LIST OF APPENDICES

Appendix

ABSTRACT

Dynamics of Convergent Migration and Mean Motion Resonances in Planetary Systems

by

Jacob A. Ketchum

Co-Chairs: Fred C. Adams, Anthony M. Bloch

Recent observations of solar systems orbiting other stars show that exoplanets display an enormous range of physical properties and that planetary systems display a diverse set of architectures, which motivate further studies in planetary dynamics. Part of the richness of this dynamical problem arises from the intrinsic complexity of N-body systems, even in the absence of additional forces. The realm of physical behavior experienced by such systems is enormous, and includes mean motion resonances (MMR), secular interactions, and sensitive dependence on the initial conditions (chaos). Additional complications arise from other forces that are often present: During the early stages of evolution, circumstellar disks provide torques that influence orbital elements, and turbulent fluctuations act on young planets. Over longer time scales, solar systems are affected by tidal forces from both stars and planets, and by general relativistic corrections that lead to orbital precession. This thesis addresses a subset of these dynamical problems, including the capture rates of planets into MMR, collision probabilities for migrating rocky planets interacting with Jovian planets, and the exploration of the "nodding" phenomenon (where systems move in and out of MMR). This latter effect can have important implications for interpreting transit timing variations (TTV), a method to detect smaller planets due to their interaction with larger transiting bodies.

CHAPTER I

Introduction

The past two decades has led to tremendous progress in our understanding of extrasolar planets and the processes involved in planet formation. These advances involve both observations, which now include hundreds of planetary systems outside our own Solar System, as well as formation theories (see, e. g., Udry et al., 2007, for a review). With nearly a thousand alien worlds detected, extrasolar planets have completed their migration into the mainstream of astronomy.

The initial discoveries (Mayor & Queloz, 1995; Marcy & Butler, 1996) showed that the orbital elements of extrasolar planets are significantly different from those of Solar System planets (see Figure 1.9). Some giant planets are found in short period orbits ($P_{orb} \approx 4$ days; semi-major axes $a \approx 0.05$ AU), while others have longer period orbits with a range of eccentricity, $0 \leqslant e \leqslant 0.9$. Subsequent discoveries indicate that such planetary systems are common and display a rich variety of architectures (Marcy & Butler, 2000; Hatzes et al., 2000; Perryman, 2000; Udry et al., 2007).

The variety of architectures found in the current catalogue of exoplanets has motivated further studies in planetary dynamics. The consensus of such dynamical studies is that planets likely move (usually inward) while they are forming in a process known as planet migration (e.g., see Papaloizou & Terquem 2006 and Papaloizou et al. 2007 for reviews). This migration is a direct consequence of the tumultuous environments from which planets are formed, and occurs as a result of interactions with disk gas, dust and debris, and other planets as well as from gravitational tides. Both analytic results and numerical simulations are needed to study these complex N-body systems.

The first part of this introduction chapter contains a brief review of the observational data as well as a summary of the observational techniques used to collect the current data set of exoplanets. The discussion of observations is followed by a section on orbital dynamics, starting with a review of the known solution to the 2-body problem, and ending with an introduction to the 3-body problem and the disturbing

function. There, some important formulae for treating resonant phenomena via prolonged gravitational interactions with additional massive bodies are introduced and discussed in brief. Finally, I review some important concepts related to exoplanet and extrasolar planetary system formation, which provide the framework for the dynamical models used in attempts to understand observed system architectures. The material contained within this introduction chapter will hopefully add context to the theoretical tools developed and employed throughout this thesis.

1.1 Observations

Detecting an exoplanet is no straightforward task. Most of the planets discovered to date have not been viewed directly – rather, their existence is inferred from the effects they have on light emitted by their host stars. Therefore, nearly all of the observed properties of extrasolar planets and exoplanet systems to date rely upon our knowledge of stars and the sensitivities of the instruments built to detect changes in the light emitted from them. Despite having access primarily to mere indirect evidence, there are a great number of extrasolar planets that have been confirmed – that is, based on our knowledge of stellar physics and understanding of the different observational instruments, we are confident that observational signals are due to the influence of planets orbiting distant stars, and not some other astrophysical object or phenomena.

There are many different observational techniques used to study extrasolar planets. The physical and dynamical properties of planets detected by each technique is limited by both the effect being measured and the sensitivities of the instrument making the measurements. As it turns out, no single technique is sensitive to the full range of effects arising from all possible planet properties and dynamics configurations. However, all of the different techniques taken together comprise a decent complement of the planetary parameter space, allowing an honest and more complete census of planetary systems (see Figure 1.1). This section contains a brief summary of the past and present detection techniques used to collect the current catalog of known exoplanets. For a more thorough overview on the methods of planet detection, I refer the reader to Wright & Gaudi (2013).

1.1.1 Radial Velocity (RV) Method

Hundreds of exoplanets have been discovered via precision doppler spectroscopy of the host star's line-of-sight radial velocities. All objects in a gravitationally bound

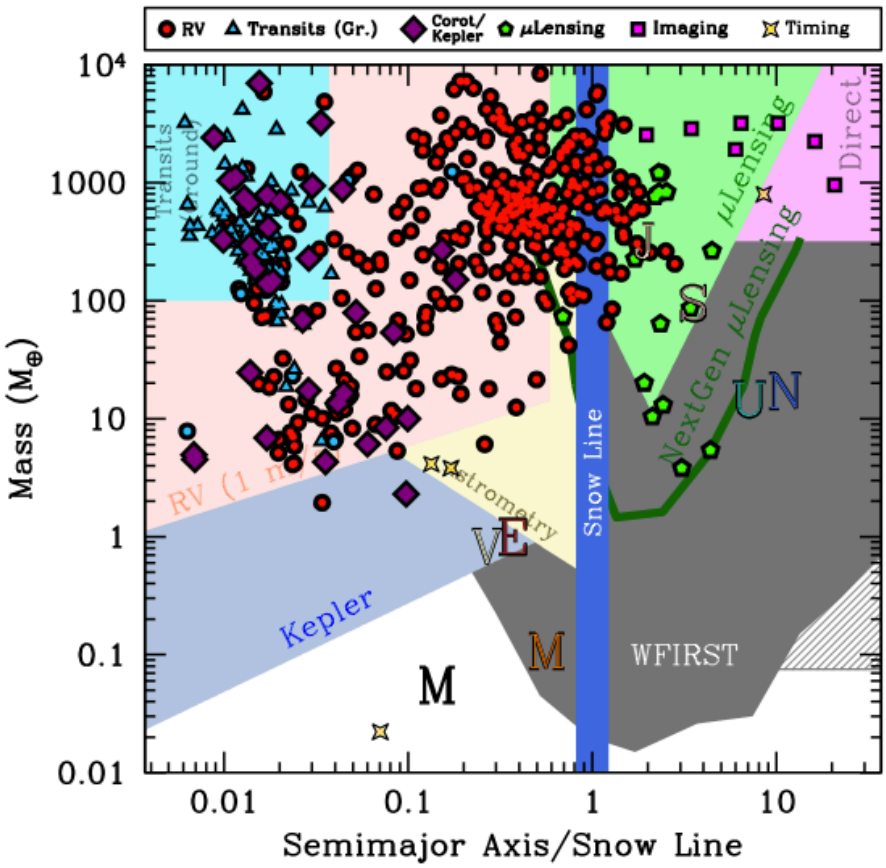

Figure 1.1: Observational sensitivity ranges. This figure shows a scatter plot for the masses (in Earth masses) and orbital distances (normalized by each system's snow line) for known exoplanets as of December 2011. The different shaded regions highlight the range of sensitivities for the different detection methods and different planet finding programs. Nearly the entire plane shown here is covered only by the full complement of detection methods and planet finding programs. This demonstrates that a diverse set of observational techniques are currently required to get a more accurate galactic planetary census. Figure taken from Wright & Gaudi (2013).

system orbit a common center of mass. In the simple 2-body Keplerian case, the planet and star both have elliptical orbits with the center of mass at one focus. Doppler shifts in select stellar spectral lines are measured, and from these measurements, radial velocities corresponding to a few $\times 10^1$ m/s are routinely measured. To compare this measurement to the Solar System, Jupiter causes the Sun to move at 13m/s, and Earth imparts radial velocities of about 0.4m/s. For example, the RV signal of the star 51 Peg is shown in Figure 1.2, which provided evidence for the first exoplanet orbiting a main sequence star (Mayor & Queloz, 1995). The amplitude

of the signal gives the minimum mass of the planet $m_p \sin i$, whereas the particular shape of the sinusoid gives the period T, eccentricity e, and longitude of periastron ω of the planet's orbit (see Appendix A for more information on the shape of a Keplerian RV curve). However, to detect an exoplanet using this method, the duration of the observation program should be on order of several orbital periods to sufficiently constrain the shape of the RV curve. Given that RV planet finding programs began around 20 years ago, this necessity places a current upper limit on the semi-major axes of $\sim$ 10AU for planets discovered through RV measurements.

Current state of the art instruments achieve RV precisions $\sim$ 1.0 m/s (e.g., Dumusque et al., 2012; Pepe et al., 2011, using HARPS) and (Keck/HIRES, Howard et al., 2011) – about the speed of a comfortable walking pace. However, such precise measurements require exquisitely calm stellar conditions in order to attain clear spectral readings. For many stars, it is simply not possible to detect signals at such low radial velocities – the surface of these stars exhibit stellar atmospheric fluctuations and/or magnetic activity (star spots), effects that doppler broadens spectral lines, leading to noise levels that dominate and bury possible stellar reflex motions induced by less massive exoplanets. It should be noted that Earth analog detections require RV measurements of $\sim$ 0.1 m/s, a signal off limits for most stars given their surface activity.

1.1.2 Transit Method

A transit event occurs when one astrophysical body moves into the line of sight of another, or more particularly, when an exoplanet moves into the line of sight of its host star. Figure 1.3 shows a sketch of the geometry involved in a simplified transit scenario. Here, a spherical planet with radius R_p moves in a slightly inclined circular orbit about a spherical star with radius R_*. The dashed ellipse shows the orbital trajectory of the planet about the star projected into the plane of the sky. If the planet's orbital plane lies within $\theta \approx \sin^{-1}(R_*/a)$ radians of the line of sight, then the trajectory intersects the disk of the star, blocking a fraction of starlight proportional to the fractional area of the stellar disk being blocked by the planet, $\Delta F/F = (R_p/R_*)^2$. This flux decrement happens once per orbit, so that the time between successive transits yields the planet's orbital period. Upon initial ingress of the transit (at location 1) the planet begins to block some light emitted from the stellar surface, and so the observed flux of photons from the star decreases. At full ingress (location 2) the full disk of the planet has moved within the disk of the star, and the observed flux decrement is maximal. At egress of the transit (location 3)

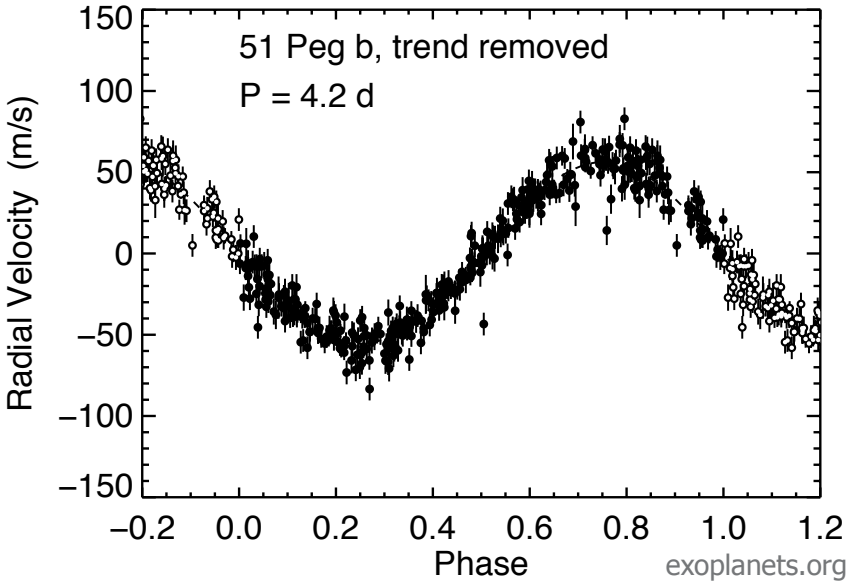

Figure 1.2: Radial velocity time series, de-trended, of 51 Peg. Radial velocity time series, phase-folded, with center of mass motion removed (de-trended) for the first exoplanet discovered orbiting a main sequence star, 51 Peg b (Mayor & Queloz, 1995). Image courtesy of exoplanet.org database.

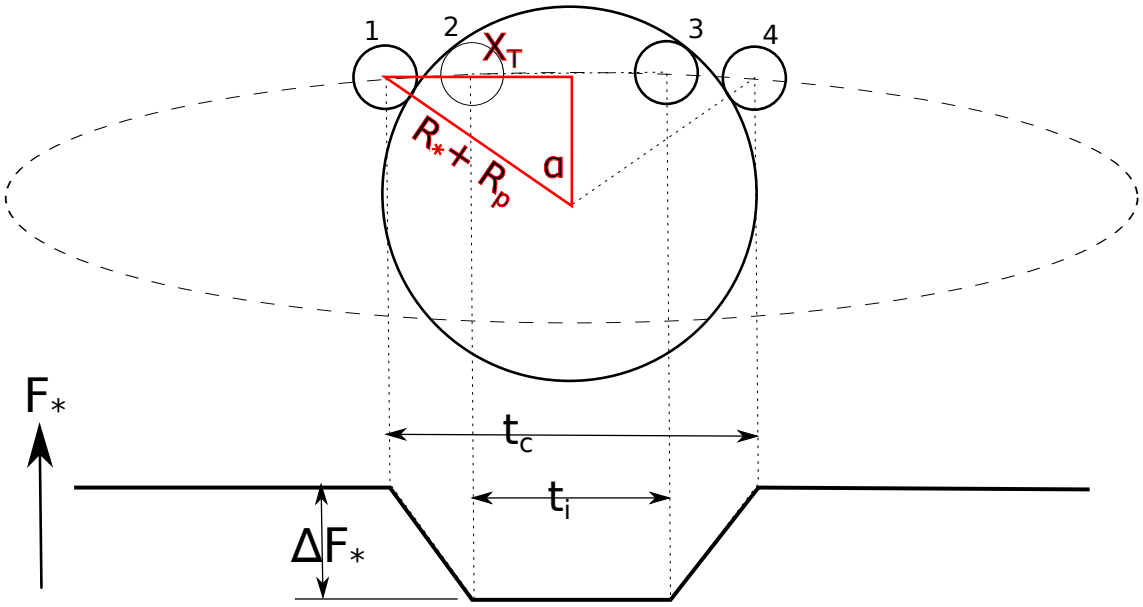

Figure 1.3: Geometry for exoplanet transiting a stellar disk and schematic of stellar flux decrement. A simplified diagram depicting the geometry of a planet's ingress and egress eclipse during a stellar transit and the schematic representation of the stellar luminosity decrement during the transit event. The star and planet are assumed to be spherical and the two bodies orbit the common center of mass in circular orbits. The dashed ellipse represents the circular orbit of the planet around the star projected into the plane of the sky. Below is a schematic representation of the stellar luminosity received at different moments during the transit. The transit depth ΔF_* is on the order of 0.1 - 1% during transit.

the disk of the planet begins to move out of the star's disk, and the observed flux increases until the planet reaches location 4, whereupon the observed flux returns to normal. See Appendix B for a more thourough discussion about the timing involved during a transit event.

To detect a transit, one must search for stars that exhibit such periodic dips in stellar luminosity (for example, see Figure 1.4). The orbiting object's radius, semi-major axis, and inclination can be determined from the shape, depth, and period of flux decrement. The object's mass, however, cannot be deduced from the transit as a generic mass-radius relation for planets has been elusive (see Figure 1.12 and note the wide range in radii for a given mass). For this reason, transit signals found in large surveys such as Kepler are considered "planet candidates" (or Kepler objects of interest, KOI) until follow up measurements, typically using the radial velocity

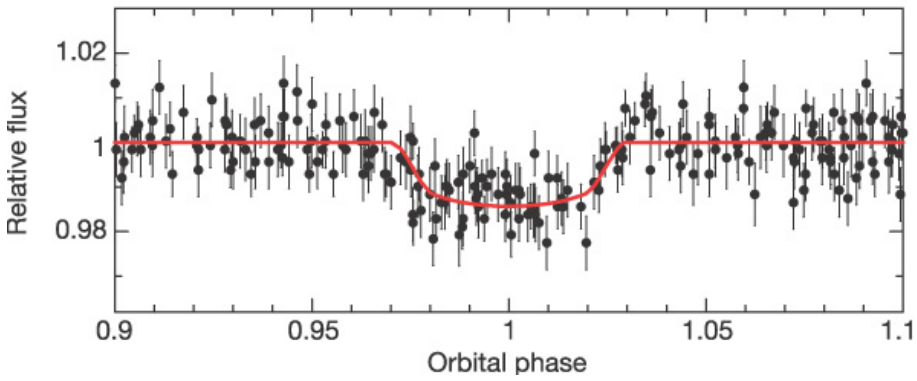

Figure 1.4: Relative flux of first planet discovered through transit detection. Relative flux of first planet discovered (OGLE-TR-56 b) by means of transit detection (Konacki et al., 2003). The swath of points depicted in this figure is a result of phase-folding the photometric observations made at varying intervals.

method, can determine the mass. In this case, since the orbit inclination is approximately known ($\cos i \approx 1$), radial velocity measurements return the actual mass of the planet, m_p.

Space based instruments are sensitive to changes in stellar luminosity down to a level of $\Delta F \approx 0.01\%$. Tranist surveys more readily turn up objects with relatively large radii ($R_p \approx 0.04 R_*$) that orbit in close proximity to their host stars.

In addition to the planet's radius and the orbital period, many other details can be determined from the transit, including the orbital inclination relative to the star's equator via the Rositer McLaughlin effect (Winn, 2011). In special instances of inflated Hot Jupiters, information about the planet's atmosphere, composition, and even weather can be determined (e.g., see Grillmair et al., 2008; Knutson et al., 2008).

Transit timing variations (TTVs) have been suggested as a promising way to infer the existence of smaller, otherwise undetectable planets (Agol et al., 2005; Holman & Murray, 2005). TTVs are slight differences of the intervals between successive transit events, which could be due to the gravitational influence of an otherwise unseen planet. TTVs are greatest when the perturbing planet is in or near a mean motion resonance with the transiting planet. So far over 50 Kepler planets have been discovered via the TTV method (exoplanets.org). For example, Kepler 36 b and c is an interesting system in a short period, 7:6 resonance. With such short orbital periods, resonant interactions are very strong between these two planets, which act

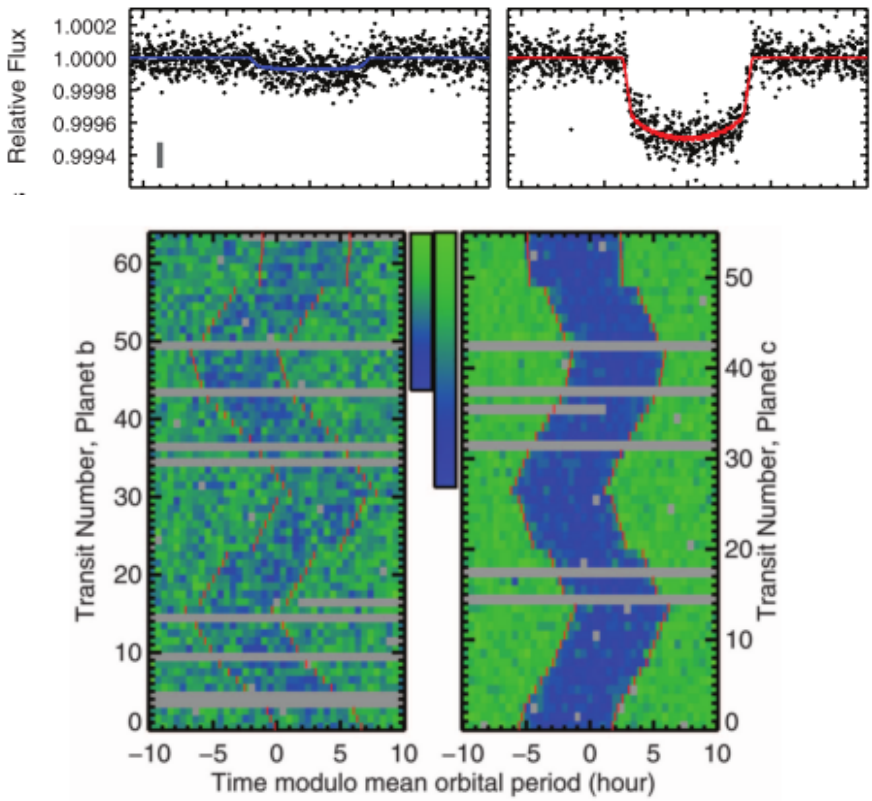

Figure 1.5: Sample TTV observational data (Kepler 36). Phase-folded photometric data (top) and transit timing variations (bottom) for Kepler 36. Current methods used to search for TTVs in the raw photometric data uncovered the smaller planet (b) in this system. Figure taken from Carter et al. (2012).

to disrupt the periodicity of transit events. Consequently, large TTVs are found in the photometric data for this system (Carter et al., 2012) – so large, in fact, that the smaller of the two planets was initially overlooked (see Figure 1.5).

1.1.3 Gravitational Microlensing

Gravitational lensing occurs when a gravitational point source in the foreground bends the trajectory of photons emitted from a background point source. The source's signal is magnified and the intensity is amplified by an amount that is inversely proportional to the angular separation on the sky of the source and the lensing object (Sackett, 1999). When both the background source and the lens are stars, the relative proper motion of the two objects can be swift enough that the angular separation changes appreciably over a short time – anywhere from a few days to a few months

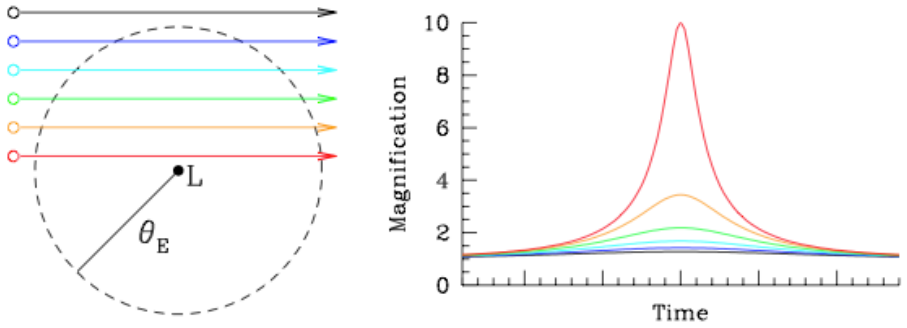

Figure 1.6: Microlensing light curve for point source lens. **Left**: Close up sketch of a gravitational lensing encounter between a background source (multiple, colored horizontal lines) and the foreground lens (center point labeled "L"). The Einstein ring is shown as a dashed circle. **Right**: Light curve for each of the color coded trajectories shown in the left panel. The magnification peaks more strongly for trajectories with smaller impact parameter. The timescale for the event is typically between a few weeks to a few months. Note the magnification symmetry of the lensing event. Figure originally appears in Sackett (1999)

– and so too will the intensity of the source star change on a similar timescale. The primary lensing event produces a light curve that is symmetric in time like that shown in Figure 1.6, where the peak intensity is inversely proportional to the impact parameter of the encounter. When the lensing star is host to a planet, then the presence of the additional planetary mass can change the light curve's profile and further increase the magnification of the source star. Additional spikes in source intensity occur as the source passes through a complicated locus of points called the caustic, which arises due to the two-point geometry of the lens. The particular profile of the light curve can be quite complicated, and depends upon the planet to lens star mass ratio and the angular separation between the two. The additional features of the light curve profile are sort of "optimal" for planets that reside near the Einstein ring, in a region called the lensing zone, during the microlensing event. This translates to an on-sky distance on the order of several AU.

There exist serious limitations when using microlensing for planet searches. First, for there to be a signal in the first place requires a fortunate alignment of celestial objects. For this reason, photometric surveys aimed toward a dense field of background stars are more likely to have higher success rates. Further, this method also suffers from a short window of time where observations can be made, leaving follow up measurements difficult if not impossible to make. Additionally, frequent pho-

tometric measurements of the source intensity must be made in order to accurately determine the profile of the light curve, hence accurately determine the planet's properties. Despite these limitations, 18 exoplanets have been discovered via gravitational microlensing.

1.1.4 Astrometry

This technique involves detecting stellar motion transverse to the line-of-sight with photometric measurements. The maximum transverse displacement of a star about the system's center of mass due to a planet in a circular orbit around it is

$$2r = 2\mu \left[\left(\frac{T}{2\pi} \right)^2 \mathcal{G} M_* \right]^{1/3} ,$$

where $\mu \equiv m/M_*$ is the planet to star mass ratio, T is the orbital period, and $\mathcal{G}$ is the gravitational constant. On the sky, the total angle subtended by transverse motion is given by $\psi = 2r/d$, where d is the distance from Earth to the system. Astrometric measurements are thus more sensitive to planets that are comparatively massive relative to their host stars, have long period orbits, and systems in relatively close proximity to Earth. For a 1 m_{jup} planet in a 1 year circular orbit around a 1 $M_\odot$ star, the astrometric motion of the star is about 1 mas at a distance of 2 pc, and about 1 μas at 2 kpc. The best ground based instruments top out at around 10 μas resolution, and space based instrumentation reaches about 1 μas resolution. Not one exoplanet to date has been discovered through astrometry; however, astrometric measurements are helpful when trying to independently verify the existence of an exoplanet discovered with another technique.

1.1.5 Direct Imaging

Some planet searches have focused on directly detecting the photons arriving from the surfaces of exoplanets themselves, rather than through inference by influential effects on stellar photons. The number of photons reaching Earth from a given exoplanet pales in comparison to the number of photons coming from its host star. So, when we look at an extrasolar planetary system, observations are awash with stellar photons, often leaving a difficult task to separate and resolve the few photons emanating from and scattering off an exoplanet's atmosphere. One way to separate the photons by source is to physically shield stellar photons, leaving the few photons originating from the planet's surface to be studied. Another way to distinguish the

source of photons is to look for planets that are physically separated from their host stars by large distances.

Direct imaging efforts are generally less difficult for high planet to stellar flux ratios, and for larger angular separations between the host star and the directly imaged exoplanet. Consequently, very long period planets have been detected this way, and estimates are made to determine the planet masses. The most ideal configuration for detecting planets with this method is with high inclination (almost perpendicular incidence), so a radial-velocity follow up will not yield information about mass. The mass is usually inferred from follow-up astrometric measurements of traversal stellar wobbles. Information about the planet's atmospheric composition and conditions can also be discerned.

1.1.6 Current State of Known Exoplanets and Exoplanetary Systems

1.1.6.1 Exoplanet Masses and Numbers from the Observations

In all, the current catalogue of known extrasolar planets contains nearly 755 planets orbiting about 602 neighboring main sequence stars (note: the accounting behind these numbers depend on the source: as of November, 12, 2013, exoplanet.eu cites 1040 total exoplanets, whereas exoplanets.org cites about 755 total confirmed exoplanets, but also includes a separate accounting that includes 3455 Kepler objects of interest (KOI) which brings the potential grand total to 4210 exoplanets.) Of these 755 known exoplanets, 431 were discovered by RV measurements, 299 planets found by transit (where ≈ 56 of these were uncovered via transit timing variations), 18 by microlensing, and 7 by direct imaging. The detection rate for exoplanets has increased exponentially through the years since the first discoveries (see the top panel of Figure 1.7). The uptick in the frequency of discoveries that occurs around 2010 is due to Kepler, a space based telescope searching for transiting planets, turning on. Over 3000 planet candidates found by Kepler have been labeled objects of interest, and it is expected that many of these will be promoted to confirmed planets after follow up measurements can confirm their masses. While there has been an exponential increase in the discovery rate of planets, the mass detection limit of exoplanets has been pushed steadily lower throughout the years as well (see the bottom panel of Figure 1.7). Early on, instrumentation was successful at finding Jovian and sub-Jovian mass planets ($M > 0.1M_J$). In 2004, the first Super Earth detections were made ($M \approx 10M_\oplus \lesssim 0.03M_J$), and the envelope keeps being pushed steadily downward to the point where we are almost able to detect Earth mass planets today

($M \approx 0.003 M_J$). As such, most exoplanet data at our disposal concerns gas giant planets, and data concerning terrestrial type exoplanets are relatively scant.

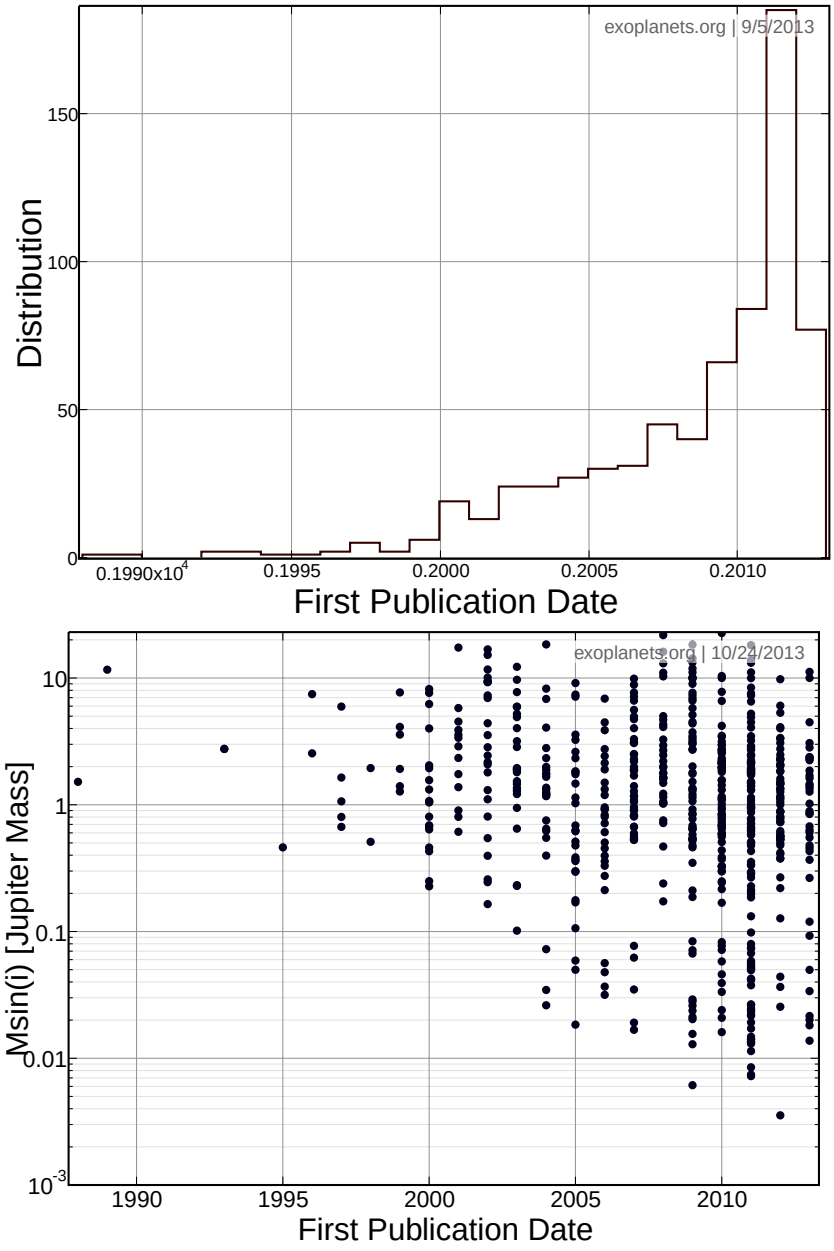

Figure 1.7: Discovery rate and planetary mass sensitivities by year. **Top**: Histogram showing the growth in the number of exoplanets discovered per year since 1988. The discovery is marked by the date of first publication on a planet finding. **Bottom**: Scatterplot showing the minimum mass of confirmed planets versus the year of discovery. The lower envelope of the collection of points represents a proxy for instrument sensitivity to planet mass through history. Both figures from exoplanets.org.

1.1.6.2 Statistics of Host Stars

Since most exoplanets are observed indirectly through observations of their host stars, it would be good to include some information about the stars from the current sample. The catalog of confirmed exoplanets has been sampled from stars ranging in distance from near the center of the galaxy to the local neighborhood (see top panel of Figure 1.8). Also, current planet detection methods are sensitive to stars that are very much like the Sun (see bottom panel of Figure 1.8). This fact may raise questions about the completeness of the current catalog of exoplanets. The initial mass function of stars in the galaxy peaks around $M \approx 0.2 M\odot$, so it makes one wonder if the current sample of exoplanets is representative of the entire population of planets in the galaxy. Many questions about observational biases could be explored from the viewpoint of any one of the Figures presented in this section. However, it is beyond the scope of this thesis to dwell on such matters.

1.1.6.3 Dynamical Features of Observed Systems

Figure 1.9 shows a scatter plot of the eccentricity vs. semi major axis for the list of currently known exoplanets. Perhaps the most striking feature is that in contrast to solar system planets, exoplanets have been found with a large range of semi-major axes $10^{-2} \lesssim a \lesssim 10^{1}$ AU and eccentricities $0 \leqslant e \lesssim 0.95$. The range and scatter in semi-major axis presents difficulties for *in situ* planet formation models, where planets form from the material in a disk in the vicinity of where the planet is found. Planets with small semi-major axes tend to have lower eccentricities – the reason is two-fold due to proximity to the host star. First, all orbits' eccentricities are limited by the physical size of the host star – the radius of periapse for an orbit cannot be any smaller than the stellar radius. Second, gravitational tidal forces are strong at such close proximity to the star, and these tides tend to circularize eccentric orbits on a timescale of Gyr, further reducing the range of eccentricities observed.

1.1.6.4 Multiple Planet Statistics

Of the 602 stars currently known to host exoplanets, 100 of them contain more than one planet with a combined total of 242 exoplanets in all. These numbers are expected to increase as follow up RV measurements are made on the vast catalogue of Kepler's objects of interest. Figure 1.10 shows a current histogram of the frequency of multi-planet systems binned according to the number of planets detected per system.

Figure 1.11 shows the current data on the frequency of period ratios of all possible

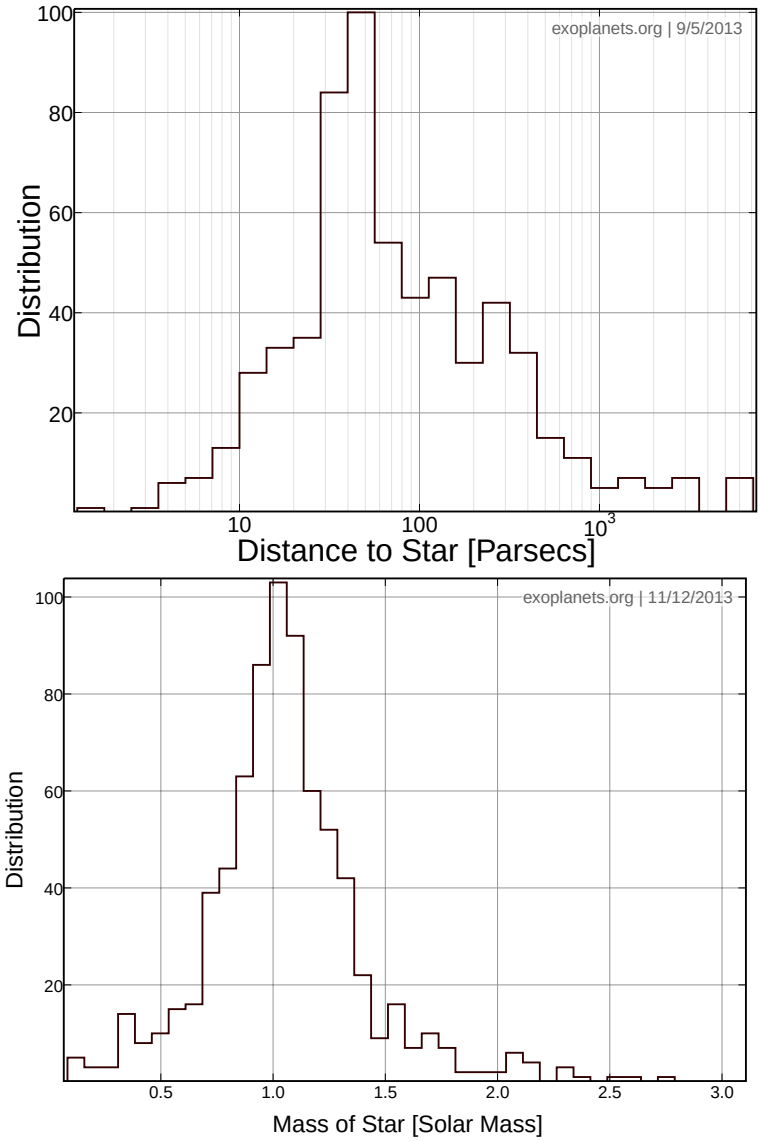

Figure 1.8: Masses and distances to current known host stars. **Top**: Number of exoplanet systems logarithmically binned by Distance in parsecs to host star from the Solar system – shows detections made spanning distances going from the local Solar neighborhood all the way to the Galactic center. **Bottom**: Mass of host stars – showing peak detection sensitivity to Solar mass stars. Typical host star masses fall in the range $0.5M\odot \lesssim M \lesssim 1.5M\odot$. Both figures courtesy of exoplanets.org.

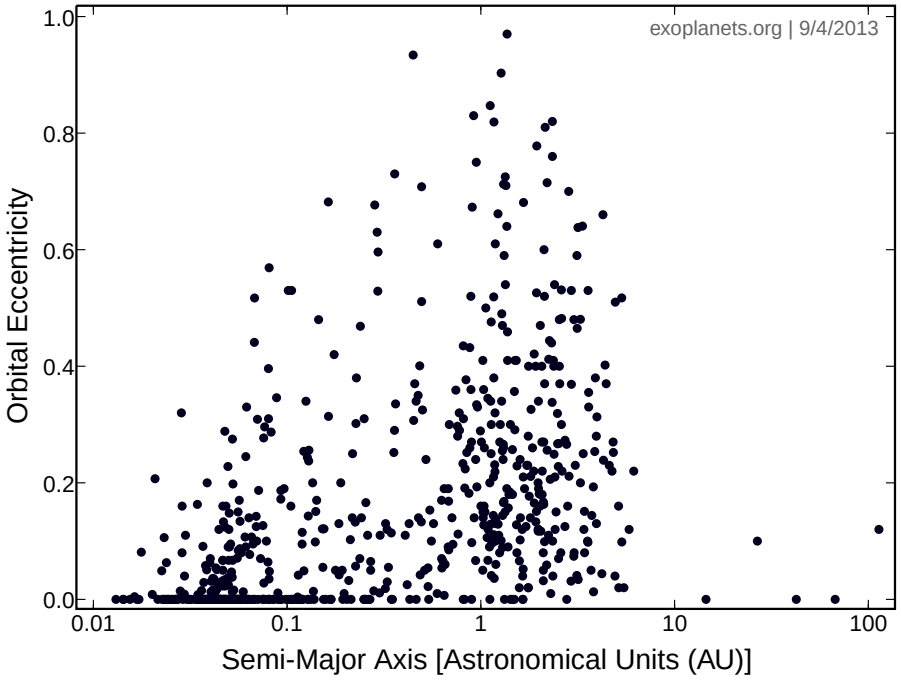

Figure 1.9: Scatter plot of the eccentricity vs. semi-major axis for the list of currently known exoplanets. Note that exoplanets are found with a wide range of semi-major axes $10^{-2} \lesssim a \lesssim 10^{1}$ AU and eccentricities $0 \leqslant e \lesssim 0.95$. The upper left portion on the graph coincides with collisional trajectories with the surface of the star, while the far right coincide with very long orbital periods. Graph generated with exoplanets.org

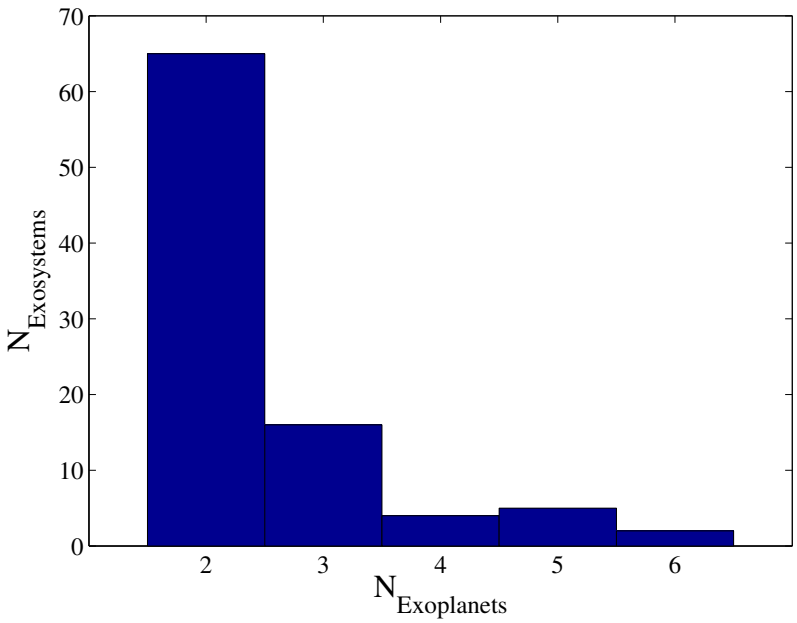

Figure 1.10: Multiple-planet system histogram. A current histogram of the frequency of multi-planet exosystems binned according to the number of confirmed planets detected per system. Already, there are 100 multiple-planet systems containing a combined total of 240+ exoplanets. These numbers are expected to rise dramatically as follow up RV measurements are made on the vast catalogue of Kepler's planet candidates.

pairings between planets in multiple-planet systems. There is an excess above a randomly uniform distribution of period ratios just wide of the 3:2, 2:1, and 3:1 period ratios, and a dearth of ratios just narrow, suggesting that resonant behavior may be contributing to or have contributed to the structure of these systems. Note that this figure shows only "small" period ratio values, not the whole range of period ratios present within the data.

1.1.6.5 Physical Properties of Exoplanets

Figure 1.12 shows the mass versus radius data currently available for exoplanets. Exoplanet radii are found from transit measurements, while mass measurements typically come from RV measurements. It is interesting to note that Jovian mass planets do not follow the trend in radii that lower mass planets tend to follow. The inflated radii of the larger Jovian planets can be somewhat accounted for with stellar irradiation and anomalous heating mechanisms. The smaller jovian planets remain somewhat of a mystery, although very massive cores and electron degeneracy are likely

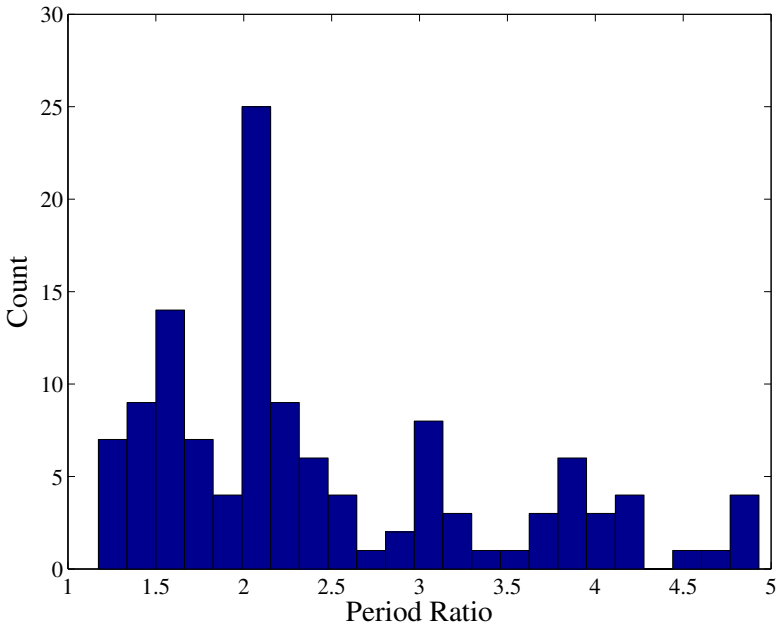

Figure 1.11: All pair-wise period ratios of exoplanets in multiple-planet systems. Current data on the frequency of period ratios of all possible pairings between planets in multiple-planet systems. There are excesses above a randomly uniform distribution of period ratios near the 3:2, 2:1, and 3:1 period ratios, suggesting that resonant behavior may be contributing to or have contributed to the structure of these systems. Note that this figure shows only "small" period ratio values, and not the full range of period ratios present within the data (which reaches values as high as 1000:1).

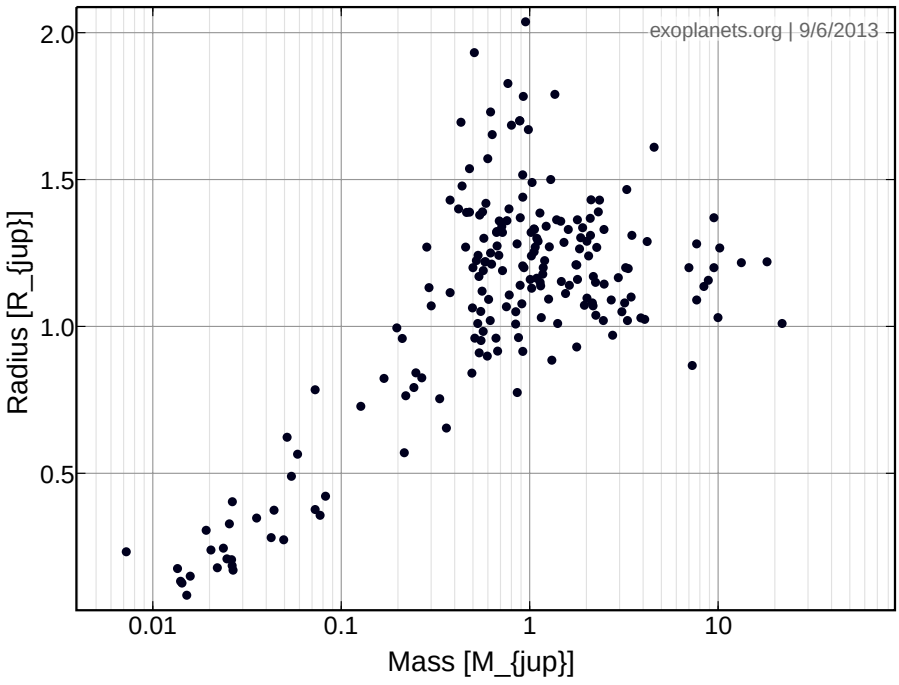

Figure 1.12: Current available Mass vs Radius data on exoplanets. Mass versus radius data currently available for exoplanets. Radius information comes from transit measurements, while mass measurements typically come from RV measurements. Figure generated with exoplanets.org database.

to play significant roles in determining the physical characteristics of these strange planets.

1.2 Dynamics

Next, we will review some of the basic dynamics that will be used in this thesis. Part of the richness of this dynamical problem arises from the intrinsic complexity of N-body systems, even in the absence of additional forces. The realm of physical behavior experienced by such systems is enormous, and includes mean motion resonances (MMR), secular interactions, and sensitive dependence on the initial conditions (chaos). Additional complications arise from other forces that are often present: During the early stages of evolution, circumstellar disks provide torques that influence orbital elements, and turbulent fluctuations act on young planets. Over longer time scales, solar systems are affected by tidal forces from both stars and planets, and by general relativistic corrections that lead to orbital precession.

1.2.1 2-Body Problem: Dynamics and Orbital Elements for Keplerian Systems

The basis of solar system dynamics is enshrined in Kepler's three laws of orbital motion. These laws, which were empirically deduced from solar system observations (for all the planets known at the time – Mercury, Venus, Mars, Jupiter, and Saturn) spanning several decades of the late 16th century, can be summarized as follows:

1. Planets orbit the sun following elliptical paths, with the sun at one focus.

2. The line joining the sun and a planet sweeps out equal areas in equal times independent of the planet's position along its orbit.

3. The square of a planet's orbital period is proportional to the cube of the semi-major axis.

After Kepler established these laws upon empirical grounds, Newton then invented the theoretical framework which, as a direct consequence, contained all three laws. Treatments of the gravitational two body problem can be found in most elementary mechanics text books, but it shall be useful to review the solution here. The equations of motion for two point particles of mass m_1 and m_2 under mutual gravitational attraction are

$$m_1\ddot{\mathbf{r}}_1 = \mathcal{G}m_1m_2\frac{\mathbf{r}}{r^3} \ , \tag{1.1}$$

and

$$m_2\ddot{\mathbf{r}}_2 = -\mathcal{G}m_1m_2\frac{\mathbf{r}}{r^3} \ , \tag{1.2}$$

where $\mathbf{r} = \mathbf{r_2} - \mathbf{r_1}$ is the displacement vector between the two particles. We can write the two equations of motion as one equation in the displacement vector $\mathbf{r}$,

$$\ddot{\mathbf{r}} = -\mu\frac{\mathbf{r}}{r^3} \ , \tag{1.3}$$

where $\mu \equiv \mathcal{G}(m_1 + m_2)$ is used throughout this section. Here, we see that the vector product $\mathbf{r} \times \ddot{\mathbf{r}} = d/dt(\mathbf{r} \times \dot{\mathbf{r}}) = d/dt(\mathbf{L}) = 0$, so the angular momentum vector is a constant. This result automatically gives three integrals of motion (one for each component of the angular momentum vector), and informs us that the motion is confined to a plane. Since there are only 4 degrees of freedom in a plane (in Cylindrical coordinates $r, \dot{r}, \theta, \dot{\theta}$), only one integral of motion remains, which will come shortly. First, let us focus our attention back on the solution to equation (1.3). In cylindrical

coordinates, we get two equations — one equation for the radial component,

$$\ddot{r} - r\dot{\theta}^2 + \frac{\mu}{r^2} = 0 \ , \tag{1.4}$$

and one for the azimuthal component

$$\frac{1}{r}\frac{d}{dt}\left(r^2\dot{\theta}\right) = 0 \ . \tag{1.5}$$

The azimuthal equation (1.5) gives the constant magnitude of the angular momentum vector, defined as $h \equiv r^2\dot{\theta}$. The radial part (given in equation [1.4]) is a non-linear differential equation in time, and its solution cannot be expressed as elementary functions (more on the radial coordinate as a function of time to follow). However, we can solve for the radial displacement as a function of θ by making the substitution $r = 1/u$, so that $\dot{r} = -h\ du/d\theta$. The equation resulting from this substitution is

$$\frac{d^2u}{d\theta^2} + u = p^{-1} \ ,$$

with positive definite constant $p \equiv h^2/\mu$. The solution to this ordinary differential equation is a conic section in cylindrical coordinates

$$r(\theta) = \frac{p}{1 + e\cos(\theta - \varpi)} \ . \tag{1.6}$$

where e, the eccentricity, and ϖ, the longitude of periapse, are constants of integration. The type of conic section described by r is determined by the value of the eccentricity. For elliptical (circular) trajectories, $p = a(1 - e^2)$, where a is the semi-major axis (radius) of the orbit. For a parabolic trajectory, $p = 2q$, where q is the distance of closest approach between the two particles. For hyperbolic trajectories, $p = a(e^2 - 1)$. The set of coordinates given by (a, e, ϖ) describe the shape and orientation of the particles' trajectory in the orbital plane, and θ defines the location of the particle in its orbit. One glaring limitation of these 4 variables is, since the solution to equations (1.4) and (1.5) did not involve time explicitly, they too do not contain any information about time. Kepler understood this limitation, and figured out a way to calculate the planet's position at a given time. The relation that makes this possible is called Kepler's equation,

$$M = E - e\sin E \ , \tag{1.7}$$

where E is the eccentric anomaly, related to the true anomaly $f \equiv \theta - \varpi$ by the relation

$$\tan\frac{E}{2} = \sqrt{\frac{1+e}{1-e}}\tan\frac{f}{2} \ , \tag{1.8}$$

and the mean anomaly

$$M \equiv n(t - t_0) \ , \tag{1.9}$$

defined in terms of the mean motion $n \equiv 2\pi/T$, where T is the orbital period, and the time of periapse passage t_0. The eccentric anomaly E is the angle subtended by the major axis to the line connecting the center point of a circle which circumscribes the ellipse and the planet's projection perpendicular to the major axis onto the circle (see Figure 1.13). Although Kepler's equation provides the link between time and position for a planet in a Keplerian orbit, the equation is transcendental in E. As a result, there exists no simple expression for the position as a function of time. Representations involving complicated infinite sums can be formulated to obtain analytic expressions, but they are often divergent for larger eccentricities ($e \gtrsim 0.6 - 0.7$). While analytic expressions of Kepler's equation are limited to certain values of the eccentricity, we can numerically solve equation (1.7) exactly for any eccentricity value.

All together, the orbit and position of the planet is given by six components $(a, e, M, \varpi, i, \Omega)$, which are the semi-major axis, eccentricity, mean anomaly, longitude of perihelion, inclination, and longitude of ascending node, respectively. These six components (or any combination of a variety of equivalent components – for instance, it is customary to use the mean longitude $\lambda \equiv M + \varpi$ in place of M in this set) comprise the set of orbital elements used to describe an orbit in a 2-body Keplerian system. The three angles (ϖ, i, Ω) set the orientation of the orbit's reference frame relative to the line of sight, and the remaining components (a, e, M) locate the position of the planet in the orbit's frame of reference. Figure 1.13 shows a face on view of an elliptical orbit, showing the locations of the angles ϖ, θ, f, and E discussed in the text above. Figure 1.14 shows the orbit in 3-d space, and shows the locations of the angles i and Ω. Two reference lines are used to orient the ellipse: the line of sight (called the reference direction in the figures), and the line of the ascending node. The line of ascending node is given by the intersection between the reference plane and the orbital plane. The line of sight is self-explanatory.

The orbital period of a Keplerian orbit, T, can be found by inserting the radial equation (1.6) into the definition for angular momentum h,

$$h = r^2\dot{\theta} = \frac{p^2}{(1 + e\cos\theta)^2}\frac{d\theta}{dt} \ .$$

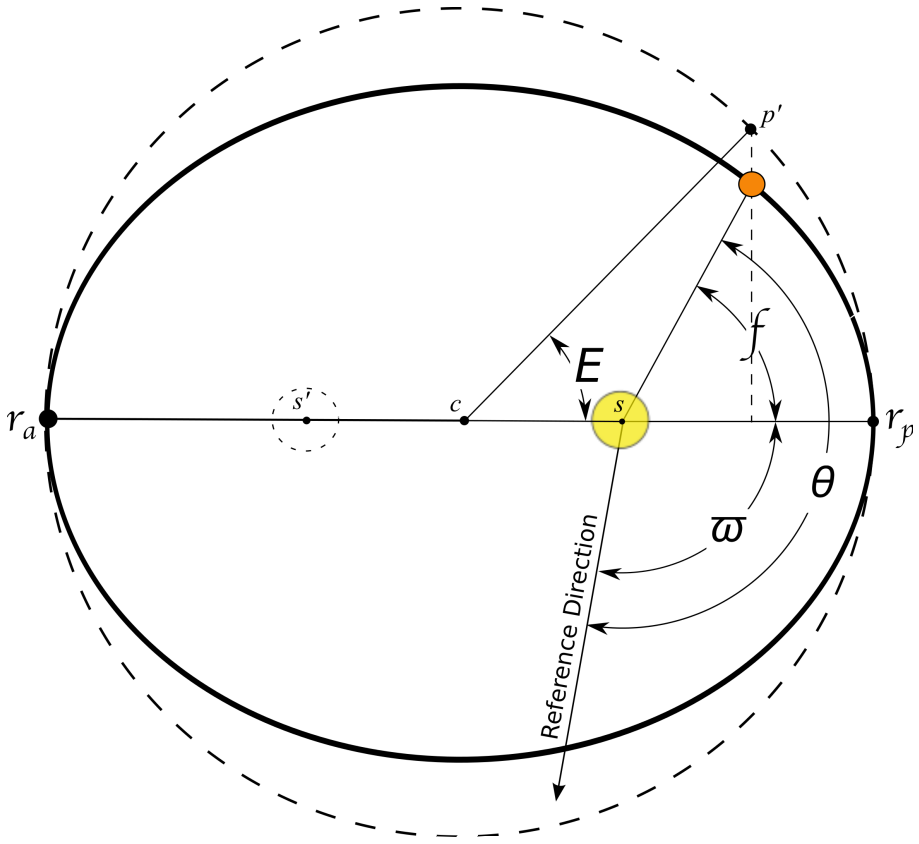

Figure 1.13: Elliptical Keplerian orbit. Figure shows longitude of periapse ϖ, true longitude θ, true anomaly $f \equiv \theta - \varpi$, and the eccentric anomaly E used in Kepler's equation (1.7). The eccentric anomaly, $E = \angle\, r_p c\, p'$, is the angle subtended by the major axis (horizontal line) to the line connecting the center point (point c) of a circle (dashed curve) which circumscribes the ellipse and the planet's projection perpendicular to the major axis onto the circle (point p'). E is a mathematical construct used in Kepler's equation to give a planet's position as a function of time.

Next, integrate the left side over the orbital period and the right over a full 2π radians,

$$\int_0^T \frac{h}{p^2} dt = \int_0^{2\pi} \frac{d\theta}{(1 + e\cos\theta)^2} \ .$$

The integrand on the left is constant, and so the resulting trivial integral is hT/p^2. The integral on the right, however, is non-trivial, and is solved using the Cauchy residue theorem in the complex plane. Its solution, after some work that I will not show here, is $2\pi(1-e^2)^{-3/2}$. Solving for T and using the valid definition of $p \equiv a(1-e^2)$ for a closed orbit, and squaring both sides gives the mathematical expression for Kepler's

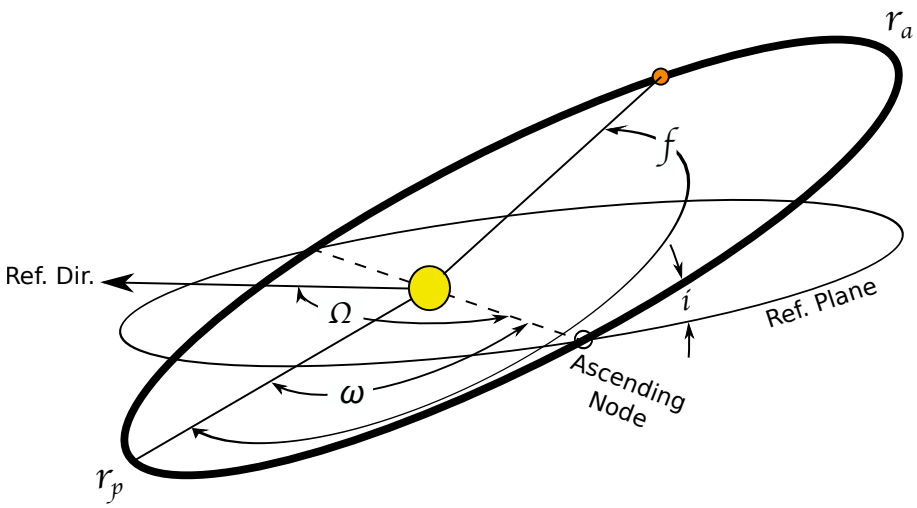

Figure 1.14: 3-d view of Keplerian orbit and relevant orbital elements therein. 3-dimensional view of a Keplerian orbit demonstrating the arguement of periapse ω, longitude of ascending node Ω, true anomaly f, and the inclination angle i in relation to the reference plane and directions of the system. The thick-lined ellipse marks the orbital trajectory, while the thin-lined ellipse represents the projection of this trajectory into the reference plane.

third law,

$$T^2 = \frac{(2\pi)^2}{\mu} a^3 \ .$$

Often in the literature and in this thesis, Kepler's third law is written in terms of the orbiting particle's mean motion, defined by $n \equiv 2\pi/T$,

$$n^2 a^3 = \mu \ . \tag{1.10}$$

To finish the treatment of the 2-body problem, it will be useful to derive the remaining integral of motion – the energy integral. First, take the scalar product of equation (1.3) with $\dot{\mathbf{r}}$

$$\dot{\mathbf{r}} \cdot \left(\ddot{\mathbf{r}} + \mu \frac{\mathbf{r}}{r^3} \right) = 0 \ . \tag{1.11}$$

After expanding the right hand side, the first term is the time derivative for the kinetic energy per unit mass, $\dot{\mathbf{r}} \cdot \ddot{\mathbf{r}} = d(\dot{\mathbf{r}} \cdot \dot{\mathbf{r}}/2)/dt = d(v^2/2)/dt$. The second term is the time derivative for the gravitational potential per unit mass, $d(-\mu/r)/dt$. Integrating the whole equation with respect to time,

$$\frac{v^2}{2} - \frac{\mu}{r} = \mathcal{E} \ , \tag{1.12}$$

where the energy per unit mass $\mathcal{E}$ is a constant, and hence an integral of the motion. We get an expression for $v^2 = \dot{\mathbf{r}}\cdot\dot{\mathbf{r}}$ using the vector component form of the displacement vector, $\dot{\mathbf{r}} = \dot{r}\hat{\mathbf{r}} + r\dot{\theta}\hat{\theta}$,

$$v^2 = \dot{r}^2 + (r\dot{\theta})^2 \ .$$

Insert the time derivative of equation (1.6) into the first term on the right hand side and use the angular momentum, $h \equiv r\dot{\theta}^2$, in the second term, which gives

$$v^2 = \left(\frac{h}{p}\right)^2 \left(\frac{2p}{r} - (1-e^2)\right) \ .$$

Recall that $h^2 = p\mu$, where p is positive definite. Inserting the above result back into equation (1.12) gives an expression for the total energy of a Keplerian orbit

$$\mathcal{E} = -(1-e^2)\frac{\mu}{2p} \ . \tag{1.13}$$

For eccentricities $0 \leqslant e < 1$, corresponding to a circular ($p = a$) or an elliptical ($p = a(1-e^2)$) orbit, the energy is negative, $\mathcal{E} = -\mu/2a$, and the orbit is bound. For eccentricities $e > 1$, corresponding to an unbound hyperbolic ($p = a(e^2-1)$) trajectory, the energy is positive, $\mathcal{E} = \mu/2a$. In the special case of a parabolic trajectory ($e = 1$), the orbital energy $\mathcal{E} = 0$.

Finally, it should be noted that the set of orbital elements, $(a, e, i, \lambda, \varpi, \Omega)$, do not comprise a canonical set of variables. In cases where it is beneficial to work with coordinates and their conjugate momenta, such as in Hamiltonian treatments, it is helpful to work in Poincarè variables, given by the following

$$\begin{aligned} &\lambda = M + \varpi \ , \quad \gamma = -\varpi \ , && z = -\Omega \ , \\ &\Lambda = \beta\sqrt{\mu a} \ , \quad \Gamma = \Lambda\left(1 - \sqrt{1-e^2}\right) \ , && Z = (\Lambda - \Gamma)(1 - \cos i) \ , \end{aligned} \tag{1.14}$$

where $\beta \equiv m_1 m_2/(m_1 + m_2)$ is the reduced mass. Here, λ, γ, and z are Poincarè coordinates, while Λ, Γ, and Z are their respective conjugate momenta. These variables are not unique, and many other sets exist for Hamiltonian treatments used throughout the literature on planetary dynamics. The Hamiltonian, equal to the orbital energy given in equation (1.13), in these coordinates is

$$\mathcal{H} = -\frac{\mu^2\beta^3}{2\Lambda^2} \ . \tag{1.15}$$

Thus, since the Hamiltonian for the 2-body Keplerian system depends only upon the momentum Λ, all of the Poincarè variables are constant in time except for λ:

$$\frac{d\lambda}{dt} = \frac{\partial \mathcal{H}}{\partial \Lambda} = \frac{\mu^2 \beta^3}{\Lambda^3} = \sqrt{\frac{\mu}{a^3}} \ . \tag{1.16}$$

This last result is Kepler's third law, where $d\lambda/dt = n$, the mean motion of the planet, and is equivalent to equation (1.10). This Hamiltonian treatment of the problem shows that all other orbital elements in a 2-body system remain constant in time.

1.2.2 Lagrange's Planetary Equations of Motion

We showed in the previous section that the orbital trajectory for a planet in a purely Keplerian system remains steady and fixed – that is to say that the orbital elements (excluding λ) absent external forces, i.e. forces beyond those of the mutual gravitational attraction of the two bodies, remain constant in time. The presence of forces beyond those of the central force of Newtonian gravity on an orbiting planet in the Kepler problem can be treated as perturbations to the regular elliptical motion, yielding time dependent orbital elements. In this case, the particular values of the orbital elements describing a planet's orbit at any given time are referred to as *osculating elements*. The time derivatives of the osculating elements are given by the following 6 coupled non-linear differential equations (Murray & Dermott, 1999) (see Brouwer & Clemence, 1961, for a full derivation)

$$\begin{aligned}
\frac{di}{dt} &= -\left(na^2\sqrt{1-e^2}\right)^{-1}\left[\tan i/2\left(\frac{\partial \mathcal{R}}{\partial \varpi} + \frac{\partial \mathcal{R}}{\partial \lambda}\right) + \csc i \frac{\partial \mathcal{R}}{\partial \Omega}\right] \ , \\
\frac{d\Omega}{dt} &= \left(na^2\sqrt{1-e^2}\sin i\right)^{-1}\frac{\partial \mathcal{R}}{\partial i} \ , \\
\frac{da}{dt} &= \frac{2}{na}\frac{\partial \mathcal{R}}{\partial \lambda} \ , \\
\frac{de}{dt} &= \frac{\sqrt{1-e^2}}{na^2 e}\left[\left(1-\sqrt{1-e^2}\right)\frac{\partial \mathcal{R}}{\partial \lambda} - \frac{\partial \mathcal{R}}{\partial \varpi}\right] \ , \\
\frac{d\varpi}{dt} &= \frac{\sqrt{1-e^2}}{na^2 e}\frac{\partial \mathcal{R}}{\partial e} + \frac{\tan i/2}{na^2\sqrt{1-e^2}}\frac{\partial \mathcal{R}}{\partial i} \ , \\
\frac{d\epsilon}{dt} &= -\frac{2}{na}\frac{\partial \mathcal{R}}{\partial a} + \frac{\sqrt{1-e^2}\left(1-\sqrt{1-e^2}\right)}{na^2 e}\frac{\partial \mathcal{R}}{\partial e} + \frac{\tan i/2}{na^2\sqrt{1-e^2}}\frac{\partial \mathcal{R}}{\partial i} \ ,
\end{aligned} \tag{1.17}$$

where $\epsilon \equiv \lambda + nt$ is the mean longitude at epoch and $\mathcal{R}$ is the disturbing function to the gravitational potential of the primary. In general, the disturbing function can

be thought of as a position-dependent scalar potential that is a local perturbation on the dominant potential of the primary mass. Because of the generality of these equations, they are applicable where position-dependent forces beyond central 2-body Newtonian gravitational forces are present, for example in N-body systems, extended mass distributions, or gravitational correction terms from general relativity. To make practical use of the above equations, a slightly different form of the disturbing function must be used for each of these contexts. The following section contains a brief introduction to the three body problem and the applicable disturbing function.

1.2.3 3-Body Problem: Equations of Motion and the Disturbing Function

In this section, we will briefly cover the relevant theory and force equations used throughout this work. The contents of this chapter is a standard 3-body treatment in existing literature, and comprehensive treatments can be found in many published texts (e.g. Murray & Dermott, 1999; Brouwer & Clemence, 1961, etc.).

Consider three point masses, $m_0,\ m_1,\ m_2$ such that $m_1,\ m_2 \ll m_0$, located at $\mathbf{r}_i$ with respect to the origin of some inertial reference frame. The bodies move under their mutual gravitational influence according to the follow system of force equations,

$$\begin{aligned}
\ddot{\mathbf{r}}_0 &= \mathcal{G}m_1\frac{\mathbf{r}_1-\mathbf{r}_0}{(r_1-r_0)^3} + \mathcal{G}m_2\frac{\mathbf{r}_2-\mathbf{r}_0}{(r_2-r_0)^3}\ , \\
\ddot{\mathbf{r}}_1 &= \mathcal{G}m_0\frac{\mathbf{r}_0-\mathbf{r}_1}{(r_0-r_1)^3} + \mathcal{G}m_2\frac{\mathbf{r}_2-\mathbf{r}_1}{(r_2-r_1)^3}\ , \\
\ddot{\mathbf{r}}_2 &= \mathcal{G}m_0\frac{\mathbf{r}_0-\mathbf{r}_2}{(r_0-r_2)^3} + \mathcal{G}m_1\frac{\mathbf{r}_1-\mathbf{r}_2}{(r_1-r_2)^3}\ .
\end{aligned} \tag{1.18}$$

Define the relative position vectors of the secondaries from the primary as $\mathbf{R}_i = \mathbf{r}_0 - \mathbf{r}_i$ for $i = 1, 2$, and the above equations of motion can be rewritten is *astrocentric coordinates*,

$$\begin{aligned}
\ddot{\mathbf{R}}_1 &= -\mathcal{G}(m_0+m_1)\frac{\mathbf{R}_1}{{R_1}^3} - \mathcal{G}m_2\left(\frac{\mathbf{R}_1}{{R_1}^3} + \frac{\mathbf{R}_1-\mathbf{R}_2}{(R_1-R_2)^3}\right)\ , \\
\ddot{\mathbf{R}}_2 &= -\mathcal{G}(m_0+m_2)\frac{\mathbf{R}_2}{{R_2}^3} - \mathcal{G}m_1\left(\frac{\mathbf{R}_2}{{R_2}^3} + \frac{\mathbf{R}_2-\mathbf{R}_1}{(R_2-R_1)^3}\right)\ .
\end{aligned} \tag{1.19}$$

Since the vectors $\mathbf{R}_1$ and $\mathbf{R}_2$ originate at the primary, the resultant equations given in (1.19) are in a non-inertial reference frame. It is, however, inertial in the limit that m_1/m_0 and m_2/m_0 goes to 0.

The terms on the right hand side are gradients of potentials, where the first term on the right hand side proportional to $\mathcal{G}(m_0+m_i)$ represents the gradient of the usual

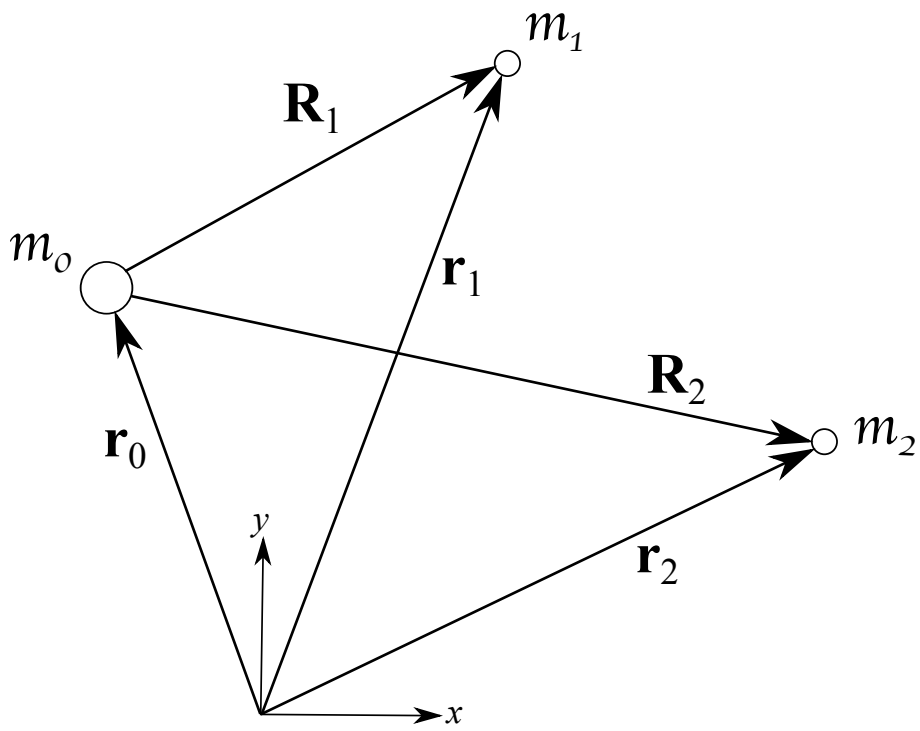

Figure 1.15: 3-body vector geometry. Diagram of the vector geometry of the 3-body problem as discussed in the text

potential from the two body Keplerian problem. The second term proportional to $\mathcal{G}m_j$ arises with the presence of an additional body, and is the gradient of the disturbing function. More specifically, the disturbing function for the inner secondary is given by

$$\mathcal{R}_1 = \mathcal{G}m_2 \left(\frac{1}{|\mathbf{R}_2 - \mathbf{R}_1|} - \frac{\mathbf{R}_1 \cdot \mathbf{R}_2}{{R_1}^3} \right) , \tag{1.20}$$

and for the outer secondary is given by

$$\mathcal{R}_2 = \mathcal{G}m_1 \left(\frac{1}{|\mathbf{R}_1 - \mathbf{R}_2|} - \frac{\mathbf{R}_1 \cdot \mathbf{R}_2}{{R_2}^3} \right) , \tag{1.21}$$

and effectively contain the source of gravitational perturbation to the simpler two body problem. These expressions can be expanded in a Fourier series, written in terms of Legendre polynomials accordingly,

$$\mathcal{R}_1 = \frac{\mathcal{G}m_2}{R_2} \sum_{\ell=2}^{\infty} \left(\frac{R_1}{R_2} \right)^{\ell} P_\ell(\cos\theta) , \tag{1.22}$$

$$\mathcal{R}_2 = \frac{\mathcal{G}m_1}{R_2}\sum_{\ell=2}^{\infty}\left(\frac{R_1}{R_2}\right)^{\ell} P_\ell(\cos\theta) + \mathcal{G}m_1\frac{R_1}{{R_2}^2}\cos\theta - \mathcal{G}m_1\frac{R_2}{{R_1}^2}\cos\theta \ , \tag{1.23}$$

where θ is the angle between position vectors $\mathbf{R}_1$ and $\mathbf{R}_2$, and $P_\ell(x)$ is the ℓ $^{\text{th}}$ Legendre polynomial.

From this point, it is only a matter of applying coordinate transformations in order to write the disturbing function in terms of familiar osculating elements. The transformation is shown within numerous references, where equations (1.22) and (1.23) both take the general form

$$\mathcal{R} = \sum \mathcal{S}\cos(\phi) \ , \tag{1.24}$$

where the strength function $\mathcal{S} \equiv \mathcal{S}(a_1, a_2, e_1, e_2, s_1, s_2)$ is a function of the two secondaries' semi-major axis, eccentricity, and inclination angle ($s_1 \equiv \sin i_1$), and the argument of the cosine, ϕ, is a function of the two bodies' osculating angles given by

$$\phi \equiv j_1\lambda_1 + j_2\lambda_2 + j_3\varpi_1 + j_4\varpi_2 + j_5\Omega_1 + j_6\Omega_2 \ , \tag{1.25}$$

where λ, ϖ, and Ω are the planet's mean longitude, longitude of periapse, and longitude of ascending node, respectively. The coefficients j_i of the osculating angles in ϕ are constrained to add to zero, $\sum j_i = 0$, which follows from azimuthal invariance of the primary's potential. The strength function, $\mathcal{S}$, is an infinite sum for each set of the j_i coefficients in ϕ, and the leading order term in each sum is proportional to ${e_1}^{|j_3|}{e_2}^{|j_4|}{s_1}^{|j_5|}{s_2}^{|j_6|}$.

When the argument of the cosine in the disturbing function is approximately stationary for many successive orbits, then the planet will encounter approximately the same perturbing potential at regular periodic time intervals. In other words, the perturbing planet subjects the test body to regular forcings at regular intervals, which in turn excites corresponding modes of the test body's orbital motion. In this situation, the system is said to be in some sort of resonance – the type of resonance determined by the set of j_i coefficients that satisfy a stationary cosine argument in the disturbing function. Since the full disturbing function is composed of an infinite number of combinations of j_i values, it may contain many resonant terms for any given orbital configuration of the 3-body system. Here, I will focus on two types of resonances talked about in this thesis: secular resonances and mean motion resonances.

A stationary cosine argument entails that $\dot{\phi} \approx 0$, which for coplanar 3-body systems means that

$$\dot{\phi} = j_1(\dot{\epsilon}_1 + n_1) + j_2(\dot{\epsilon}_2 + n_2) + j_3\dot{\varpi}_1 + j_4\dot{\varpi}_2 \ ,$$

where $\lambda \equiv \epsilon + nt$. Secular resonances occur when $\dot{\phi} \approx 0$ and the mean motions, n_1 and n_2, do not contribute to ϕ (i.e., $j_1 = j_2 = 0$). Hence, in a secular resonance

$$\dot{\phi}_s = j_3\dot{\varpi}_1 + j_4\dot{\varpi}_2 \approx 0 \ . \tag{1.26}$$

Since the j_i coefficients must sum to 0 for each argument in the disturbing function, then $j_3 = -j_4$. There are an infinite number of integers that can satisfy this requirement, and hence an infinite number of secular resonant modes that can be excited in any 3-body system. However, the strength of each secular mode is proportional to $\mathcal{S} \propto e_1^{|j|} e_2^{|j|}$, and so for systems with small eccentricities, the strongest secular modes will be those with $j_3 = 1$. Furthermore, the motion of the resonance angle ϕ_s is approximated by inserting the appropriate form of the disturbing function (equation [1.22] or [1.23]) into the expressions for $\dot{\varpi}_1$ and $\dot{\varpi}_2$ given in Lagrange's planetary equations (1.17), and substituting those resulting expressions into the right hand side for $\dot{\phi}_s$ given in equation (1.26).

Mean motion resonances occur when the planets' mean motions are in a low integer ratio with one another. Another way to say it is the planets have small integer commensurate orbital periods, $T_1/T_2 \approx |j_2|/|j_1|$. Hence, in a MMR $j_1 n_1 \approx j_2 n_2$, and

$$\dot{\phi}_{2:1} = j_1(n_1 + \dot{\epsilon}_1) + j_2(n_2 + \dot{\epsilon}_2) + j_3\dot{\varpi}_1 + j_4\dot{\varpi}_2 \ .$$

For the sake of demonstration, take $j_1 = -1$ and $j_2 = 2$, corresponding to the 2:1 MMR. There are still yet infinitely many 2:1 resonances angles, because there are an infinite number of integers that satisfy $j_3 = -(j_4 + 1)$. But, again, the strength function for each 2:1 resonance angle is proportional to $\mathcal{S} \propto e_1^{|j_4+1|} e_2^{|j_4|}$. Therefore, for small eccentricities, either $j_4 = 0, -1$ contributes the leading order term in the disturbing function. This thesis will consider several aspects of MMR, including the probability of entering resonances, the dependence on migration rates, and the degree to which turbulence can compromise resonance states.

When eccentricities are small, linear expansions of the disturbing function are sufficient for many treatments. When eccentricities get large, non-linear behaviors begin to dominate, and linearizations of the disturbing function (like the brief treatment of resonances given above) may no longer be effective.

1.3 Extrasolar System Formation as an Extension of Star Formation

While definitive proof is currently out of reach, a growing body of theoretical and observational evidence overwhelmingly suggests that planets are formed in disks (Santos et al., 2004; Kennedy & Kenyon, 2008; Mordasini et al., 2009), which arise as a direct consequence of the star formation process (Shu et al., 1987; McKee & Ostriker, 2007). Stars form in clouds of molecular hydrogen and dust, containing about a million solar masses worth of material in a space of tens of thousands of cubic parsecs (Hartmann, 2002). Densities within the cloud are large enough to undergo gravitational collapse, although magnetic fields and turbulent motions provide enough pressure support to inhibit free fall (for example, see McKee et al., 1993; Nakano, 1998, and references therein). Within a giant molecular cloud, pockets of gas slowly lose pressure support via magnetic diffusion, and other processes(Mac Low & Klessen, 2004). They grow increasingly dense before finally succumbing to gravitational collapse. Out of a molecular cloud, thousands of such cloud cores are spawned, each core containing several solar masses of material (see Larson, 1985; McKee, 1989, and references therein). On the outer parts of any given cloud core, the collapse flow is radial. However, each cloud has a small initial rotation, and angular momentum must be conserved, so, near the center, material falls onto a rotating disk (Terebey et al., 1984; Williams & Cieza, 2011). Buried deep near the mid-plane of the accretion disk, shrouded by an opaque froth of turbulent dust and gas, the conditions are believed to be ripe for planet formation.

After the star is formed, material from the accretion disk continues to feed the young protostar until the disk runs out of gas – a milestone that typically occurs after an elapsed time of 3 to 10 Myr for most stars. Radiation coming from the star strips the disk of its gas from the inside out, and external radiation evaporates the outer disk. Accretion removes additional material. Eventually, a disk of solid debris is left behind. Evidence for disks are found associated with objects called T-Tauri stars, identified as such by the infrared excesses in the spectral energy distribution due to thermal emissions of a surrounding disk of hot dust (Shu et al., 1987; Adams et al., 1987; Hartmann & Kenyon, 1987).

However, not all features of an exoplanet system are set by the local stellar environment at the time of birth. The local stellar neighborhood can have a major influence on the architecture of a budding solar system (see Adams, 2010, and references therein). For instance, close packed stars can interrupt young systems gravitationally

through close encounters and flybys (for instance, see Laughlin & Adams, 1998; Levison et al., 2004). More commonly, massive stars can drive winds and supply radiation that prematurely deplete the essential gas and dust of nearby nascent stars, stunting the seeds of planetary growth before they have the chance to gain a sufficient foothold (see Hollenbach et al., 1994; Armitage, 2000; Adams et al., 2004, for instance). Furthermore, the orbits of planetesimals and rocks that inhabit the disk over long times are intrinsically chaotic. Exoplanet system formation hence is a stochastic process, where simulations of the best formation models can only yield probabilities for the number of planets and orbital architectures resulting from any particular set of initial conditions.

1.3.1 Planet Formation

Although many advances in understanding have been made within the last several decades, a complete theory of planet formation covering the full scale of physical quantities (from 10^{-4} to 10^{10} cm in size, 10^{-10} to 10^{30} g in mass of solids, spanning a time of $\sim 10^{15}$ seconds) has yet to be established. The most agreed upon theory of planet formation is referred to as the Nebular Hypothesis of solar system formation. The philosopher Immanuel Kant once theorized that planets in our solar system coalesced from a large cloud of dust and debris. Pierre-Simon Laplace developed this idea mathematically such that planets materialized locally from a thin disk of solids with roughly the same orbital parameters as they are found today. While this picture of planet formation is attractive for its intuitive simplicity, it is an idealization of the processes likely involved in forming planets. Many other theories of solar system formation have been presented in the time since Kant and Laplace (Woolfson, 1993; Kenyon, 2002; Tsiganis et al., 2005; Morbidelli et al., 2007; Durisen et al., 2007), each with varying degrees of success.

There are two processes by which planets are believed to be formed; (i) core accretion and (ii) gravitational instability. As mentioned in the previous section, the clock for planet formation is set by the star formation process. Accordingly, the conditions for planet formation last only as long as an appreciable basin of material resides in the disk. Thus, the planets are formed contemporarily with their galactic chauffeur.

The core accretion model (Bodenheimer & Pollack, 1986; Pollack et al., 1996) embodies the essence of Kant's idea about planet formation. This model involves the build up of a planetary core through the sequential growth of the dust and debris in a circumstellar disk, from dust to grains, grains to pebbles, pebbles to rocks,

and so on until a planetary core is finally achieved (for a review, see Papaloizou & Terquem, 2006). Once this incremental growth process can viably sustain bodies with mass approximately equal to that of Mercury – the seeds of planetary growth – gravitational focusing causes accelerated feeding upon local disk material. In cases where a sufficient amount of mass remains in the protoplanetary disk, this planet seed can feed on the surrounding gas. Initially, the rate of gas accretion is slow, leading to a modest increase in overall mass. However, if the planet reaches a critical mass of a few 10's of earth masses, run away accretion of disk gas onto the planet is triggered. This feeding frenzy is limited by the available material found locally in the disk – the newly forming gas giant depletes all locally available gas and carves a gap in the disk. Note that the radial distribution of mass required to build up all of the planets in the solar system is referred to as the *minimum mass solar nebula* (MMSN), where the surface density profile for gas and solids goes like $\Sigma \propto r^{-3/2}$ and its total mass $M \approx 0.05 M_{\odot}$ (see Hayashi, 1981). The ultimate result of this process is a planet with mass comparable to that of Jupiter, $M_{jup} \approx 1.9 \times 10^{30}$ g.

In contrast to the relatively long process of building a planet from the bottom up through the core accretion model, a planet can also form relatively quickly by gravitational instability. A disk must be very massive to exhibit gravitational instabilities – at least 10 times more massive than the standard MMSN, or a disk mass at least 10% of the stellar mass (Adams et al., 1989; Boss, 1997, 1998). When a disk is sufficiently massive, large clumps of many Jupiter masses can agglomerate from disk material in the outer regions (many 10's of AU) where orbital velocities are small and shear forces are low. Furthermore, the cooling time of disk material in this region must be short so that the outward pressure inside the newly formed clump does not dominate (Gammie & Ostriker, 1996). If these special conditions are met, the clump will be gravitationally bound to itself and feed upon disk material to grow increasingly massive within a few orbits. After a span of time lasting about 1000 years, the clump has eaten enough material that, after cooling and condensing, the resultant object becomes either a gas giant planet or brown dwarf star with nearly identical composition to that of the central star. Recent work shows that giant planets can both form and migrate inward on very short timescales (Zhu et al., 2012). It is difficult to ascertain whether protostellar disks contain the required mass for gravitational instabilities to be effective – observations of disks account for only a fraction of the total mass (see, for instance, Williams & Cieza, 2011, and references therein). Therefore, it is also difficult to determine the probability for a planet to be made by gravitational instability.

1.3.2 Planet-Disk Interactions

Young planets interact with the circumstellar disk, where the result of prolonged interactions is an exchange of energy and angular momentum. The gas, dust, and debris composing the disk interact with an embedded planet gravitationally in a manner that transports angular momentum away from the central star (for instance, see Goldreich & Tremaine, 1980; Ward, 1997a). Numerical simulations are a wonderful tool for understanding the dynamical evolution of the disk and hence the momentum transport due to many factors, including the gravitational perturbations from an embedded planet. However, these simulations are extremely computationally expensive, so dynamical studies spanning the full expected disk lifetime is currently very difficult if not impossible. For such studies, it is more economical to approximate a disk's affect on a planet's orbit, rather than to simultaneously carry out the hydrodynamic evolution of the disk. Below, I outline the treatment of planet-disk interactions found in the literature (see, for instance Goldreich & Tremaine, 1980; Ward, 1997a; Tanaka et al., 2002; Goldreich & Sari, 2003a; Papaloizou et al., 2007; Moorhead, 2008; Lubow & Ida, 2011).

To determine the torque between the disk and an embedded planet, the planet is treated as a perturbing body, whose potential can be written as a Fourier series accordingly,

$$\psi^p(r,\theta;t) = \sum_{l=-\infty}^{\infty}\sum_{m=0}^{\infty} \psi_{l,m}(r)\cos(m(\theta-\Omega_{l,m}t)) \ . \tag{1.27}$$

The gradient of this potential with respect to the planet's location $\mathbf{r}_p$ is equivalent to a disturbing function to the disk, $\mathcal{R} = \nabla_{\mathbf{r}}(\psi^p)$, which provides force corrections to the disk from the usual central force of the non-perturbed case. The pattern speed of the potential $\Omega_{l,m}$ is the angular frequency of a reference frame in which the cosine's argument is stationary. In a flat disk, $\Omega_{l,m}$ can be written in terms of the planet's mean motion n_p and epicyclic frequency κ_p,

$$m\Omega_{l,m} = mn_p + (l-m)\kappa_p \ . \tag{1.28}$$

Since the planet's orbital precession rate is $\dot{\varpi}_p = n_p - \kappa_p$, the pattern speed can be rewritten in terms of the orbital elements discussed in section 1.2,

$$m\Omega_{l,m} = ln_p + (l-m)\dot{\varpi}_p \ . \tag{1.29}$$

Taking $\theta = n_d t$ to be the azimuthal coordinate of a particle in the disk, then the

cosine argument is cast into a similar form as that in equation (1.25)

$$\phi = l\lambda_p - m\lambda - (l-m)\varpi_p \ . \tag{1.30}$$

In such form it becomes apparent that, in exact analogy to equation (1.24), the leading order term in the potential $\psi_{l,m} \propto e_p^{|l-m|}$, so that, for small eccentricities, the largest contributions to the potential in (1.27) will come from terms with $l = m,\ m \pm 1$. For these particular values of l, the argument ϕ is stationary (slowly varying) at locations in the disk where its mean motion $n_d = (l/m)n_p$. Thus, the disk will be strongly perturbed at locations where the rotational speed is in mean motion resonance with the planet. For $l = m$, then $n_d = n_p$, corresponding to corotational resonances (CR). For $l = m \pm 1$, either

$$n_d = \frac{m-1}{m} n_p \ ,$$

corresponding to an inner Lindblad resonance (ILR), or

$$n_d = \frac{m+1}{m} n_p \ ,$$

corresponding to an outer Lindblad resonance (OLR). These gravitational perturbations act as torques on the disk, causing spiral density waves to form at the locations of ILR and OLR. In this formulation, the total torque on the disk due to the planet is

$$\Gamma_{disk} = -\int_{disk} \Sigma r \times \nabla_{\mathbf{r}} \psi^p \ dA \ , \tag{1.31}$$

where Σ is the prescription for the disk's surface density and dA is an area element of the disk. The torque on the planet is equal and opposite the disk torque, $\Gamma_p = -\Gamma_{disk}$, and through these torques, the disk and planet exchange orbital energy and momentum at rates of

$$\frac{dH}{dt} = \Gamma \ , \qquad \text{and} \qquad \frac{dE}{dt} = \Omega_{l,m}\Gamma \ , \tag{1.32}$$

(Goldreich & Sari, 2003b).

For simple disk models, approximate expressions for the net torque on the disk are found by summing a finite number of modes. It is generically the case that the net contribution to the torque from ILR is negative and from OLR is positive. Surprisingly, the planet's main gravitational influence is to repel disk material – inner disk material gets diverted inward and outer disk material gets pushed farther out. The deeper the planet's gravitational potential, the more effectively it diverts disk

material from it's orbital path in this manner. Tanaka et al. (2002) carries out the the calculation in equation (1.31) for isothermal disks with 2D and 3D geometries, and find that the total torque on the disk from ILR, OLR, and CR is

$$\begin{aligned} \Gamma_{3D} &= (1.364 + 0.541\alpha) \left(\frac{m_p}{M_*}\frac{R}{H}\right)^2 \Sigma R^4 \Omega^2 \ , \\ \Gamma_{2D} &= (1.160 + 2.828\alpha) \left(\frac{m_p}{M_*}\frac{R}{H}\right)^2 \Sigma R^4 \Omega^2 \ . \end{aligned} \tag{1.33}$$

Despite the understanding of planet-disk interactions gained from the above analytic treatment, such expressions for disk torques should be used with caution. The above calculations were limited to a linear treatment of the component torques (i.e., first order in eccentricities). However, non-linear terms can dominate torques in some common situations, which render the expressions derived in the linear regime invalid. In the following sections I will discuss some of the ways in which disk torques effect the dynamics of embedded (proto)planets.

1.3.2.1 Planet Migration

Torques arising from a planet embedded in a disk excite spiral density waves at locations of Lindblad resonances. These density waves in turn impart torques back onto the planet and can cause the planet's orbital radius to either grow or shrink – an effect called migration. There are two main types of disk-driven planet migration (Ward, 1997a). Type I migration is valid for planets that do not displace a substantial amount of disk material via torques. The planet's migration rate is written as

$$\tau_a \equiv \frac{r}{\dot{r}} \ ,$$

where $\dot{r} = \dot{h} dr/dh$, the angular momentum for a Keplerian orbit is $h = m_p\sqrt{\mu r}$, and torque is the time rate of change of angular momentum $\Gamma = dh/dt$. Substituting gives

$$\tau_a = -\frac{m_p\sqrt{\mu r}}{2\Gamma} = -\frac{h}{2\Gamma} \ ,$$

and so the migration timescale is a function of the planet's Keplerian angular momentum and inversely proportional to the reaction torque on the planet from the disk (equation [1.31]). Using the total torque on a 3D isothermal disk found by Tanaka

et al. (2002), the Type I migration timescale is

$$\tau_a^I = (2.7 + 1.1\alpha)\frac{M_*}{m_p}\frac{M_*}{\Sigma R^2}\left(\frac{H}{R}\right)^2 \Omega^{-1} \ , \tag{1.34}$$

where α is given in the surface density profile $\Sigma \propto R^{-\alpha}$ and H is the disk scale height. The migration rate then increases with planet mass, or for planets orbiting close to the star. For example, for a $1M_{earth}$ planet at 1AU in a MMSN around a $1\mathrm{M}_\odot$ star, this migration rate is $\tau_a \approx 10^5$yr. Considering this migration rate as constant, the planet migrates into the star in about 0.5 Myr, which is much shorter than the expected lifetime of the disk.

If a planet is massive enough, it can clear away a substantial annulus of disk material and open up a gap, in which case, the planet is subject to Type II migration. In order to clear a gap however, gravitational torques must compete with thermal processes and turbulent viscosity acting within the disk that resist gap opening. For gravitational torques to win out over these processes and open up a gap in the disk, the planet's Hill sphere, $r_h \approx a(m_p/3M_*)^{1/3}$, must be at least comparable to the scale height of the disk H (Lin & Papaloizou, 1986),

$$\frac{m_p}{M_*} \gtrsim 3\left(\frac{H}{a}\right)^3 \ .$$

Furthermore, the gravitational torques clearing the gap must be stronger that the torques at gap's edge from disk viscosity (Lubow & Ida, 2011). This condition results in another bound on the planet mass required to open a gap in the disk,

$$\frac{m_p}{M_*} \gtrsim C\sqrt{\frac{\nu}{a^2\Omega_p}}\left(\frac{H}{a}\right)^{3/2} \ ,$$

where $\nu = \alpha c H$ is the turbulent viscosity in an alpha-disk prescription (Shakura & Sunyaev, 1973), c is the gas sound speed, H is the scale height of the disk, and C is a factor of order unity. For typical parameters in a MMSN disk, $\alpha \sim 10^{-4}$, and at $a \approx 5$AU, by the above conditions, a gap is opened for $m_p \approx 0.2M_{jup}$, or approximately the mass of Saturn. A gap in the disk acts as a momentum transport barrier, and the planet migrates with the disk material, provided that the local disk mass is greater than the planet's mass. For such a sufficiently massive disk, the

migration rate is thus determined by the viscous diffusion rate of disk material

$$\tau_a^{II} \sim \frac{a^2}{\nu} \ . \tag{1.35}$$

Type II migration times are generally larger than Type I rates by one or two orders of magnitude.

Another type of migration can occur, imaginatively called Type III migration (for a review, see Papaloizou et al., 2007). An extremely quick and efficient way to transfer angular momentum from the inner parts to the outer parts of the disk is via corotation resonances. Because this mechanism of angular momentum transport is so efficient, associated timescales are the shortest of all migration types, $\tau_a^{III} \approx 10^3 - 10^4$ years at a distance of $\sim$ 1AU. Since corotational torques arise only when disk material cohabits the planet's orbit, only planets that are not massive enough to clear gaps in the disk can possibly experience Type III migration.

The particular migration rates and even direction of migration cited in this section are all subject to change if the physical state of the disk is different than the "nice" properties and configurations they were assumed to have in the derivations of the torque. Nonetheless, these three types of gas driven migration mechanisms demonstrate that the protoplanetary disk is a highly interactive environment, capable of removing substantial amounts of energy and angular momentum from the orbits of the largest giant planets. In an almost ironic twist, the problem astrophysicists face in not of how planets migrate, but rather how to get planets to not migrate so fast. The gas disk resides in the protostellar environment for $10^6 - 10^7$ years, and so the migration rates quoted above are many magnitudes lower than the lifetime of gas in the disk. Even worse, migration rates tend to increase with mass, setting a seemingly impossible clock of $\sim$ 1Myr for planetary cores to grow into giant planets before plummeting into the star. Fortunately, the situation faced by all planets is not so dire – nearly 1000 planets have been discovered thus far, and the discovery rate is accelerating (see Section 1.1.6.1). Many different mechanisms have been proposed to slow or reverse the migration rates, including refinements to disk physics and their subtle intricacies (e.g., dead zones, magnetic turbulence, x-point, etc.), or disruptive interactions with other embedded planets. It is very likely that there is not one single thing that will fix the gas driven migration rates found throughout the literature. Rather, the answer is probably a combination of all of the above.

The cause of migration is not limited only to interactions with the gas disk – solar system environments are filled with objects for planets to interact with gravitationally,

and hence exchange energy and angular momentum. Planets can migrate from dynamical scattering with planetesimals left over in the disk after the gas has dispersed. Evidence for scattering of planetesimals in the solar system is found in the crater record on the surfaces of the terrestrial planets and the moon (Wetherill, 1975). The time of the late heavy bombardment is an important constraint used in dynamical models of the final phases for the formation of the solar system (Tsiganis et al., 2005; Levison et al., 2011). Furthermore, planets can migrate from planet-planet scattering, however, migration caused by scattering will occur in discrete, abrupt changes to the semi-major axes of participating planets, and will not resemble a gradual migration caused by a gas-disk. Still, other process may have a hand in determining the radial distance of an exoplanet relative to its host star, such as secular interactions between planets or stellar tidal interactions for short period planets. The latter effect can lead to dissipative divergence where the period ratio for a pair of close-in planets in MMR evolves to be many percent wide of nominal resonance due to tidal circularization (Batygin & Morbidelli, 2013; Lithwick & Wu, 2012), thus providing one explanation for the surplus of multiple-planet systems containing planet-pairs wide of nominal resonance (see Figure 1.11). However, these latter migration mechanisms usually require long times to take effect and generally do not move planets far from their initial orbits. The bottom line is that it takes an external mass source to make a planet migrate, and out of all the migration mechanisms mentioned here, the one with the most available mass, and hence the greatest potential to induce migration, is gas-disk migration. For this reason, the migration epoch for newly forming planetary systems is generally considered to coincide with the gas-disk phase of the circumstellar disk, even though other mechanisms, which remain in effect long after the gas-disk has vanished, can play a roll in establishing the variety of observed system architectures (e.g., see Section 1.1.6.3).

1.3.2.2 Eccentricity Damping/Excitation

In a similar manner that disk torques drive migration of an embedded planet, they also affect the orbital eccentricity on timescales comparable to the migration time. The change in orbital eccentricity is characterized by the eccentricity timescale given by

$$\tau_e \equiv \frac{e}{\dot{e}} \ .$$

The details of the eccentricity response for a planet orbiting within a disk of gas and dust depends on the particular properties of the disk, the shape of the gap carved

by the planet, and the physical properties of the planet itself (Moorhead & Adams, 2008). For small eccentricities, disks tend to damp orbital eccentricity of planets (Goldreich & Tremaine, 1980), but numerical simulations that account for more complicated disk geometries show that eccentricity excitations may be common in some situations. However, disks are believed to have a damping effect on eccentricity more often than an excitation effect. The argument in favor of disks generally damping eccentricities is as follows: In multiple planet systems, persistent eccentricity excitations from the disk would ultimately result in intersecting orbits, increasing the strength and frequency of planet-planet interactions and increasing the probability of losing a planet as a result of ejection, accretion, or collision. Indeed, previous research shows that if circumstellar disks were to generally excite the orbital eccentricities of embedded planets, then multiple-planet systems should be rare (Moorhead & Adams, 2005). However, multi-planet exosystems do not appear to be rare; on the contrary, observations show that they may be common (Fabrycky et al., 2012).

1.3.2.3 Magneto-Hydrodynamical Turbulence

Early on, during the cloud collapse phase of star formation, galactic magnetic fields that thread the material get dragged in as part of the collapse. As a consequence of the flux freezing that is thought to occur, weak magnetic fields starting out as a few microGauss grow to many MG at the surface of the star. A substantial portion of the initial magnetic field can remain trapped within the circumstellar disk where planets are born and have an effect on the dynamics that play out therein. For instance, disks may exhibit MRI turbulence, in which case planets could receive substantial perturbations of angular momentum depending on the strength of the turbulence and mass of the disk. Turbulence induced within disk material by magnetic fields can cause the disk to organize on larger scales that in turn creates gravitational perturbations on macroscopic bodies inside the disk by the way of angular momentum perturbations (Laughlin et al., 2004). Over time, these random kicks in momentum from MRI turbulence can disrupt the orbits of forming planets and change the space of dynamical states available to the system overall.

1.4 This Thesis

As outlined above, extrasolar planetary systems display a rich variety of dynamical processes. This thesis addresses a subset of these dynamical problems, including convergent migration, mean motion resonances, and gravitational scattering. Chapter

II addresses the capture rates of planets into MMR (Ketchum et al., 2011b). Pairs of extrasolar planets often lock into mean motion resonance as a result of convergent migration. Here, I study how MMR lock depends on the type of resonance, the migration rate, the eccentricity damping rate, and the amplitude of the turbulent fluctuations. Chapter III addresses the collision probabilities for migrating rocky planets interacting with Jovian planets (Ketchum et al., 2011a). Hot Jupiters exhibit a wide range of radii for a given mass. Here, I consider one particular migration scenario that outlines a regime of parameter space where collisions of rocky planets is a viable mechanism for increasing the core mass and metallicity for Hot Jupiters. Chapter IV contains an exploration of the "nodding" phenomenon where systems move in and out of MMR (Ketchum et al., 2013). This effect can have important implications for interpreting transit timing variations (TTV), a method to detect smaller planets due to their interaction with transiting larger bodies.

CHAPTER II

Effects of Turbulence, Eccentricity Damping, and Migration Rate on the Capture of Planets Into Mean Motion Resonance

** The text appearing in this Chapter is an enhanced version of work originally published in Ketchum, Adams & Bloch, 2011a*

2.1 Abstract

Pairs of migrating extrasolar planets often lock into mean motion resonance as they drift inward. This Chapter studies the convergent migration of giant planets (driven by a circumstellar disk) and determines the probability that they are captured into mean motion resonance. The probability that such planets enter resonance depends on the type of resonance, the migration rate, the eccentricity damping rate, and the amplitude of the turbulent fluctuations. This problem is studied both through direct integrations of the full 3-body problem, and via semi-analytic model equations. In general, the probability of resonance decreases with increasing migration rate, and with increasing levels of turbulence, but increases with eccentricity damping. Previous work has shown that the distributions of orbital elements (eccentricity and semimajor axis) for observed extrasolar planets can be reproduced by migration models with multiple planets. However, these results depend on resonance locking, and this study shows that entry into – and maintenance of – mean motion resonance depends sensitively on migration rate, eccentricity damping, and turbulence.

2.2 Introduction

The past decade has led to tremendous progress in our understanding of extrasolar planets and the processes involved in planet formation. These advances involve both observations, which now include the detection of hundreds of planets outside our Solar System (see, e. g., Udry et al., 2007, for a recent review), along with a great deal of accompanying theoretical work. One surprising result from the observations is the finding that extrasolar planets display a much wider range of orbital configurations than was originally anticipated. Planets thus move (usually inward) from their birth sites, while they are forming or immediately thereafter, in a process known as planet migration (e.g., see Papaloizou & Terquem 2006 and Papaloizou et al. 2007 for recent reviews).

Many of the observed solar systems contain multiple planets, and many others may be found in the near future. For systems that contain more than one planet, theoretical work indicates that the migration process often results in planets entering into mean motion resonance (e.g., Lee & Peale, 2002; Nelson & Papaloizou, 2002), at least for some portion of their migratory phase of evolution. During this epoch, interacting planets (which are often in or near resonance) tend to excite the orbital eccentricity of both bodies. This planet scattering process, acting in conjunction with inward migration due to torques from circumstellar disks, can produce broad distributions of both semi-major axis and eccentricity (Adams & Laughlin, 2003; Moorhead & Adams, 2005; Chatterjee et al., 2008; Ford & Rasio, 2008); these distributions of orbital elements are comparable to those of the current observational sample, although significant uncertainties remain. In any case, the final orbital elements at the end of the migration epoch — and planetary survival — depend sensitively on whether or not the planets enter into mean motion resonance.

These systems are highly chaotic, displaying extreme sensitivity to initial conditions, so that the outcomes must be described statistically. Nonetheless, the distributions of final system properties are well-defined and depend on whether the planets enter into mean motion resonance as they migrate inwards; the outcomes also depend on the type of resonance and how deeply the planets are bound into a resonant state. The circumstellar disks that drive inward migration also produce damping and/or excitation (Goldreich & Sari, 2003b; Ogilvie & Lubow, 2003) of orbital eccentricity, and this complication affects the maintenance of resonance. The disks are also expected to be turbulent, through the magneto-rotational instability (MRI) and/or other processes (Balbus & Hawley, 1991). With sufficient amplitude and duty cy-

cle, this turbulence also affects the maintenance of mean motion resonance (Adams et al., 2008; Lecoanet et al., 2009; Rein & Papaloizou, 2009), and thereby affects the distributions of orbital elements resulting from migration (Moorhead, 2008).

The goal of this Chapter is to understand the probability for migrating planets to enter into mean motion resonance and the probability for survival of the resulting resonant states. Previous work has shown that entry into resonance is affected by the migration rate (Quillen, 2006), where fast migration acts to compromise resonant states. This study expands upon previous efforts by considering the effects of not only the migration rate, but also eccentricity damping and turbulent forcing on the probability of attaining and maintaining a resonant state. This Chapter considers the action of these three variables, jointly and in isolation, and covers a wide range of parameter space. In addition, we address the problem through both numerical and semi-analytic approaches (where 'semi-analytic' refers to models where the equations are reduced to, at most, ordinary differential equations.) The results depend on the type of resonance under consideration; this work considers a range of cases, but focuses on the 2:1, 5:3, and 3:2 mean motion resonances.

This Chapter is organized as follows. We first perform a large ensemble of numerical integrations in Section 2.3. These numerical experiments follow two planets undergoing convergent migration, and include both eccentricity damping and forcing terms due to turbulent fluctuations. The results provide an estimate for the survival of systems in resonance as a function of migration rate, eccentricity damping rate, and turbulent amplitudes. In order to isolate the physical processes taking place, we develop a set of model equations to study the problem in Section 2.4. This model, which follows directly from previous work (Quillen, 2006), illustrates how fast migration rates and high eccentricities act to compromise resonance. The Chapter concludes, in Section 2.5, with a summary of results and a discussion of their implications for observed extrasolar planets.

2.3 Numerical Integrations

2.3.1 Formulation

In this section we consider the direct numerical integration of migrating planetary systems, i.e., we integrate the full set of 18 phase space variables for the 3-body problem consisting of two migrating planets orbiting a central star. For most of our simulations, the planets are started in the same plane so that the dynamics is only two dimensional; however, we have also run cases that explore all three spatial

dimensions. The integrations are carried out using a Burlisch-Stoer (B-S) integration scheme (e.g., Press et al., 1992). In addition to gravity, we include forcing terms that represent inward migration, eccentricity damping, and turbulence. All three of these additional effects arise due to the forces exerted on the planet(s) by a circumstellar disk. In this context, however, we do not model the disk directly, but rather include forcing terms to model its behavior, as described below.

To account for planet migration, we assume that the semimajor axis of the outer planet decreases with time according to the ansatz

$$\frac{1}{a}\frac{da}{dt} = -\frac{1}{\tau_a}\,, \tag{2.1}$$

where τ_a is the migration time scale. Further, we assume that only the outer planet experiences torques from the circumstellar disk.

Small planets, those with masses smaller than that of Saturn, cannot clear gaps in their circumstellar disks and tend to migrate inward quickly in a process known as Type I migration (e.g., Ward, 1997a,b). A number of studies have shown that the Type I migration rate depends on the disk thermal properties and on local gradients of the gas density (e.g., Baruteau & Masset, 2008; Paardekooper & Papaloizou, 2008; Masset & Casoli, 2009; Paardekooper et al., 2010). As a result, for some disks, Type I migration can be much slower (sometimes even directed outward) and a wide range of migration rates is possible. Larger bodies clear gaps and migrate more slowly. Estimates of the migration timescale for planets with $a \sim 1$ AU typically fall in the range $10^4 - 10^6$ yr (e.g., see Goldreich & Tremaine, 1980; Papaloizou & Larwood, 2000).

Planets are thus expected to experience a range of migration rates, depending on both planet masses and disk properties. Since we want to isolate the effects of migration rate on entry into resonance, we adopt a purely parametric approach. We thus consider a wide range of migration rates, where the migration timescale varies over the range $\tau_a = 10^3 - 10^6$ yr. Note that the shorter time scales are included here to study the physics of resonance capture (at these fast rates) and are not generally expected in most circumstellar disks. On the other hand, fast migration could occur for planets with mass $\sim 10 M_\oplus$ migrating within circumstellar disks that have sufficiently small aspect ratios ($H/r < 0.03$) and large masses (Masset & Papaloizou, 2003).

In addition to inward migration, circumstellar disks also tend to damp orbital eccentricity e of the migrating planet. This damping is generally found in numerical

simulations of the process (e.g., Lee & Peale, 2002; Kley et al., 2004), and can be parameterized such that

$$\frac{1}{e}\frac{de}{dt} = -\frac{1}{\tau_e} = K\left(\frac{1}{a}\frac{da}{dt}\right) \qquad \text{so that} \qquad \tau_e = \tau_a/K\,, \tag{2.2}$$

where τ_e is the eccentricity damping timescale. Some analytic calculations suggest that eccentricity can be excited through the action of disk torques (Goldreich & Sari, 2003b; Ogilvie & Lubow, 2003), although multiple planet systems would be compromised if this were always the case (Moorhead & Adams, 2005). Additional calculations show that disks generally lead to both eccentricity damping and excitation, depending on the disk properties, gap shapes, and other variables (e.g., Moorhead & Adams, 2008). The value of the damping parameter K can also be inferred from hydrodynamical simulations, which predict a range of values. Studies of resonant systems (Kley et al., 2004) advocate K values of order unity. In isothermal disk models, however, $K \sim 10$ for typical cases (e.g., Cresswell & Nelson, 2008). More recent work indicates that in radiative disk models, the eccentricity damping parameter K can be as large as 100 (Bitsch & Kley, 2010).

In spite of the aforementioned uncertainties, this study focuses on the case of pure damping, adopts fixed values of K for a given simulation, and considers its effects on the dynamics of mean motion resonances. We expect that the inclusion of damping will act to enhance the survival of mean motion resonances (Lecoanet et al., 2009). Using the ansatz of equation (3.8), this study considers a wide range of the damping parameter K such that $0 \leqslant K \leqslant 100$, where we consider the cases $K = 1$ and $K = 10$ as our "standard" values.

Turbulence is included by applying discrete velocity perturbations at regular time intervals; for the sake of definiteness, the forcing intervals are chosen to be twice the orbital period of the outer planet (four times the period of the inner planet for systems with 2:1 period ratio). Both components of velocity in the plane of the orbit are perturbed randomly, but the vertical component of velocity is not changed. The amplitude of the velocity perturbations thus represents one of the variables that characterize the system. These amplitudes are chosen to be consistent with the expected torques, as described below.

The torques due to turbulent fluctuations have been studied previously using MHD simulations (e.g., Nelson & Papaloizou, 2004; Laughlin et al., 2004; Nelson, 2005; Oishi et al., 2007), and these results can be used to estimate the range of amplitudes. The torque exerted on a planet by a circumstellar disk can be expressed as a fraction of

the benchmark torque $T_D = 2\pi G\Sigma r m_P$, where Σ is the surface density of the disk, r is the radial coordinate, and m_P is the planet mass (Johnson et al., 2006). The scale T_D thus serves as a maximum torque in this problem. The amplitude of the expected angular momentum fluctuations is then given by $\Delta J = f_T \Gamma_R T_D t_T$, where f_T is the fraction of torque scale T_D realized by the disk, Γ_R is a reduction factor due to planets creating gaps in the disk, and t_T is the time required for the disk to produce an independent realization of the turbulence. Previous work suggests that $f_T \sim 0.05$ (Nelson, 2005), $\Gamma_R \sim 0.1$ (Adams et al., 2008), and t_T is comparable to the orbit time of the outer planet (Laughlin et al., 2004; Nelson, 2005). Including all of these factors, we expect that $[(\Delta J)/J] \sim 10^{-4}$ under typical conditions (a disk mass of $\sim 0.05\ M_\odot$ with well-developed MRI turbulence such that $\alpha \sim 10^{-3}$). Under some circumstances, the equatorial plane of the disk is not sufficiently ionized to support MRI turbulence and a dead zone develops; in this case, the fraction f_T would be dramatically decreased. Given the uncertainties in turbulent behavior, and the wide range of possible disk conditions, the fluctuation amplitude could vary by an order of magnitude (perhaps more) in either direction. As a result, we consider turbulent fluctuation amplitudes in the range $0 \leqslant [(\Delta J)/J] \leqslant 10^{-3}$.

For a given realization of the migration scenario, we need to determine whether or not the system resides in mean motion resonance. First, we determine the ratio of the orbital periods of the two planets. It is straightforward to determine when systems have nearly integer period ratios and this condition can be used as a proxy for being in a mean motion resonance. However, this condition is necessary but not sufficient, so we must also monitor the relevant resonance angles (Murray & Dermott, 1999, hereafter MD99). For first order resonances, these angles have the form

$$\theta_1 = (j+1)\lambda_2 - j\lambda_1 - \varpi_1\,, \tag{2.3}$$

$$\theta_2 = (j+1)\lambda_2 - j\lambda_1 - \varpi_2\,, \tag{2.4}$$

$$\theta_3 = \varpi_1 - \varpi_2\,. \tag{2.5}$$

For second order resonances, these angles take the form

$$\theta_1 = (j+2)\lambda_2 - j\lambda_1 - 2\varpi_1\,, \tag{2.6}$$

$$\theta_2 = (j+2)\lambda_2 - j\lambda_1 - \varpi_1 - \varpi_2\,, \tag{2.7}$$

$$\theta_3 = (j+2)\lambda_2 - j\lambda_1 - 2\varpi_2\,, \tag{2.8}$$

$$\theta_4 = \varpi_1 - \varpi_2 \,. \tag{2.9}$$

In order to monitor the angles, and determine if the system is in a resonant state, we must choose the appropriate time windows. Note that the resonance angle $\theta_0 = \varpi_1 - \varpi_2$ oscillates on a much longer timescale than the other angles (where $\theta_0 = \theta_3$ (θ_4) for first (second) order resonances). As a result, the angle θ_0 is measured over a time period corresponding to 1500 orbits of the outer planet, whereas the other angles (which oscillate faster) are monitored over a time window of 300 orbits of the outer planet. These timescales are chosen to be (roughly) several times the expected libration periods of the angles (and the expected libration periods can be calculated from the restricted three-body problem — see MD99). Each angle is considered to be in libration if its value stays bounded within 120 degrees of the effective stability point for the time periods given above. In this context, the effective stability point is determined by the mean value of the angle over the given time window for monitoring; note that these systems are highly interactive (e.g., due to turbulent forcing) so that the stability points are not fixed. Notice also that the value of 120 degrees was chosen arbitrarily. If any of the angles θ_i obtain a value greater than 120 degrees, measured from either side of the effective stability point, then that angle is considered to not be in resonance. The code continues to monitor all of the relevant angles for the duration of the time when the periods have a well-defined ratio (of small integers). As a result, each resonance angle could go in and out of libration many times.

2.3.2 Numerical Results for Resonance Survival

Given the formulation described above, we numerically study the entry of planets into mean motion resonance and the subsequent survival of the resonant configurations. These results depend on a number of parameters, including the migration rate, the eccentricity damping rate, the level of turbulence, and the planetary masses. As indicated by the semi-analytic models (Section 2.4, Quillen 2006), we expect the survival of mean motion resonance to be compromised with sufficiently fast migration rates. The introduction of turbulence can act to further reduce the ability of systems to stay in resonance (Adams et al., 2008), whereas eccentricity damping generally acts in the opposite direction by helping to maintain resonance (Lecoanet et al., 2009). The results also depend on the masses of the planets. As the masses increase, the systems become more highly interactive and mean motion resonance is harder to maintain.

For the first set of simulations, we begin with a standard two planet system

consisting of a Jovian mass planet $m_1 = 1 M_J$ and a "super-Earth" with the mass m_2 = 10 $M_\oplus$. The properties of this system are close to the restricted 3-body problem and hence the resonance is expected to be described reasonably well by the pendulum model of MD99. The star is taken to have a mass $M_* = 1.0\ M_\odot$. The Jovian planet acts as the inner planet and begins with an eccentricity $e_1 = 0.05$ and a period of P_1 = 1000 days (so that $a_1 = 1.96$ AU). The smaller planet starts with an eccentricity $e_1 = 0.10$ and a semi-major axis of $a_2 = 1.8\ a_1$, equivalent to a period ratio of P_2/P_1 = 2.4, which places the system comfortably outside the 2:1 mean motion resonance. Both of the planets are placed in the same orbital plane. As the outer planet migrates inward, it can (in principle) enter into the 2:1 resonance; if the migrating planet passes through the 2:1 resonance, it can then (potentially) enter into resonant states with smaller period ratios.

In this parametric study, we allow migration of the outer planet, given by equation (3.3), to continue throughout the simulations. Since the inner Jovian planet is expected to open a gap in the circumstellar disk however, the migration rate could be altered, where the variations depend on the gap structure. Although not considered herein, some disks with gaps can even halt migration altogether and produce planet traps (Masset et al., 2006). In addition, since the (smaller) outer planet often acquires substantial eccentricity, it will move in and out of the gap over the course of its orbit. This effect leads to time dependent migration torques that vary on the orbital timescale; the time variations tend to average out over the libration timescale of the resonances, but the migration rate could be altered slightly.

Because these systems are highly chaotic, different realizations of the problem lead to different outcomes. For each set of parameters, we perform an ensemble of (at least) 1000 effectively equivalent simulations, where the simulations differ only by the relative position of the two planets in their orbits and by the relative angle between the orientation of the two orbits (i.e., the arguments of periastron $\varpi_2 - \varpi_1$). The length of the numerical integration t_T is set by the migration timescale τ_a, such that $t_T = \tau_a$ for the slowest migration rate ($\tau_a = 10^6$ yr) and $t_T \approx 10\tau_a$ for the fastest migration rate ($\tau_a = 10^3$ yr). The overall integration times are thus shorter for the faster migration rates, but remain long enough to encompass many libration time scales for the relevant resonance angles.

2.3.2.1 Time Evolution and Resonance Criteria

For this set of system parameters, Figure 2.1 illustrates the basic time evolution for an ensemble of planetary systems. Here, the fractions of the systems that reside

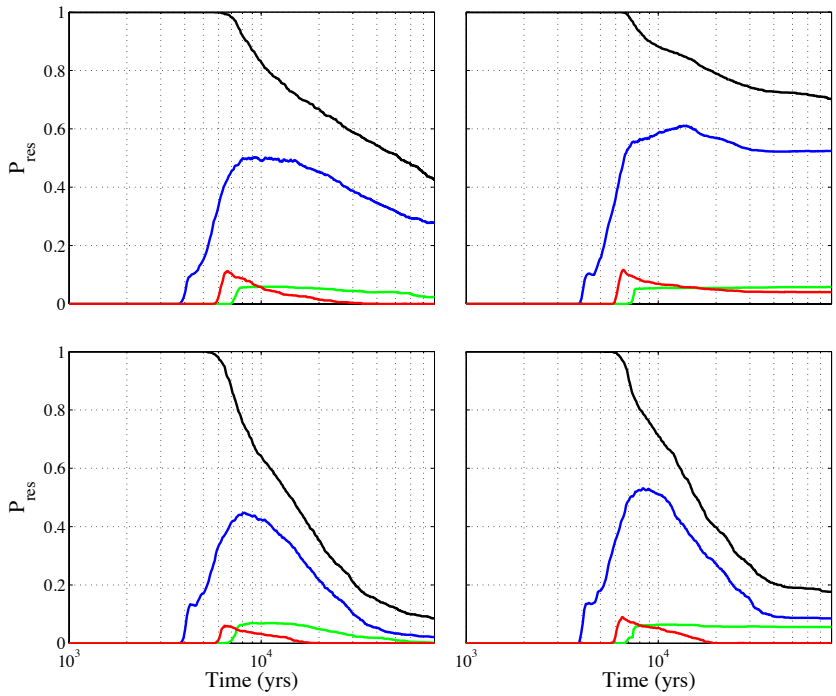

Figure 2.1: Fraction of systems in resonance as a function of time. Each curve shows the fraction of the ensemble that reside in 2:1 resonance (blue curve), 5:3 resonance (red curve), and 3:2 resonance (green curve) versus time. The systems are considered to be in resonance if the period ratios are near the relevant integer values and any of the resonance angles are librating (see text). The black curves shows the fraction of systems that remain intact, without losing a planet, as a function of time. For the four panels shown here, the migration timescale $\tau_a = 2 \times 10^4$ yr. The top row of panels includes eccentricity damping with parameter $K = 1$; the bottom row does not include eccentricity damping ($K = 0$). The left column of panels includes turbulence with $\Delta J/J = 2.5 \times 10^{-4}$; the right column does not include turbulence ($\Delta J/J = 0$.

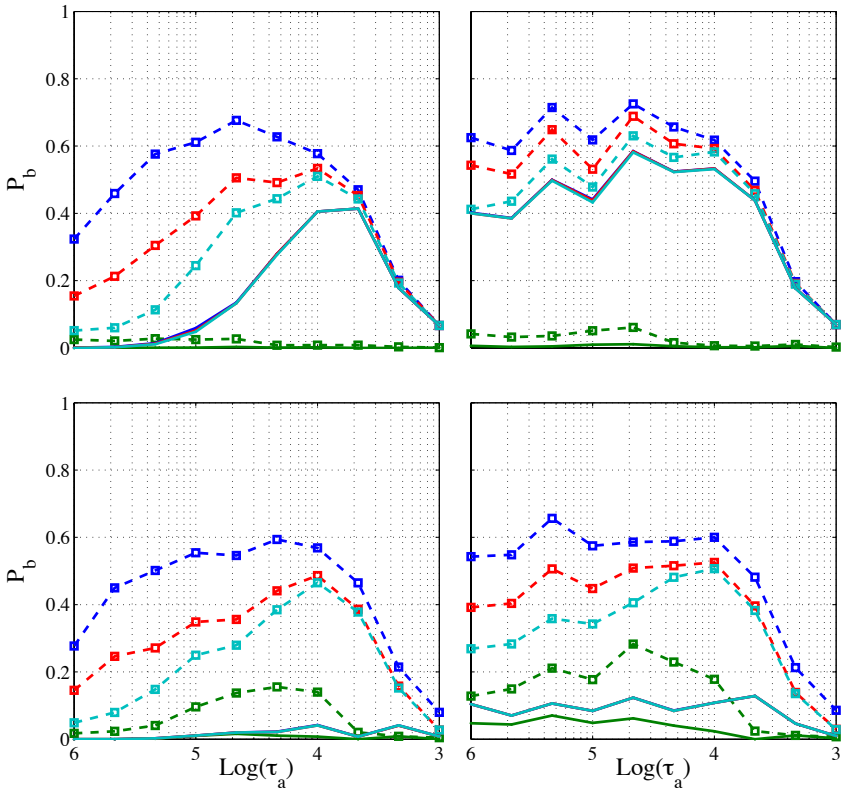

Figure 2.2: Fraction of systems in 2:1 resonance according to four criteria: The curves show the fraction of the ensemble that have nearly 2:1 period ratio (blue dashed curve), are in θ_1 resonance (cyan dashed curve), are in θ_2 resonance (red dashed curve), and are in θ_3 resonance (green dashed curve). The heavy solid curves show the fraction of the ensemble that are in resonance (of each type) at the end of the migration epoch. Note that the fractions of θ_1 and θ_2 resonances at the end of the epoch are nearly identical. The top row of panels includes eccentricity damping with parameter $K = 1$; the bottom row does not include eccentricity damping ($K = 0$). The left column of panels includes turbulence with $\Delta J/J = 2.5 \times 10^{-4}$; the right column does not include turbulence ($\Delta J/J = 0$.

in mean motion resonance are plotted as a function of time for a moderately short migration timescale $\tau_a = 2 \times 10^4$ yr. The simulations shown in the top panels include eccentricity damping with parameter $K = 1$; the two panels on the left include turbulence with the standard level of fluctuations $(\Delta J)/J \sim 2 \times 10^{-4}$. The various curves in each panel correspond to resonances with period ratios of 2:1 (blue), 5:3 (red), and 3:2 (green). The systems are considered to be in resonance if the period ratios are near the relevant integer values and if any of the resonance angles are librating (see Section 2.1 and equations [2.3 – 2.9]). Note that this migration rate was used because slower migration rates lead to few systems in the 5:3 and 3:2 resonances. Since all of the systems start outside of resonance, the fractions start at zero and increase with time as migration pushes the planets together. The 2:1 resonance is encountered first, so that corresponding fraction grows first. As the systems evolve, resonance is often compromised, so that the fractions reach a peak value and then decrease. After some of the systems leave the 2:1 state, they become locked into the 5:3 resonance, and then sometimes the 3:2 resonance. As a result, the peak fraction occurs later for resonances that are further inward, and the peak is lower for the weaker resonances (as expected). When systems begin to leave resonance, some of them decay by losing a planet through ejection, accretion onto the star, or collision with the other planet (the probabilities of these end states are quantified in Section 2.3). This effect is illustrated in Figure 2.1 by the black curves, which show the fraction of systems that retain both planets as a function of time.

We note that planetary systems are often said to "be in resonance" according to different criteria. This trend is illustrated in Figure 2.2 for the case of the 2:1 mean motion resonance. As shown in Figure 2.1, the fraction of systems that reside in resonance is a function of time for a given migration rate. The peak value of this time-dependent curve can be used as one measure of the fraction of systems that are in resonance. However, systems enter and leave resonance at different times, so that the total fraction of systems that enter resonance will be larger than the maximum fraction that reside in resonance at a given time (the peak of this curve). A necessary (but not sufficient) condition for a system to be bound into resonance is for ratio of the periods to be near 2:1. In this context, the period ratio is "near" 2:1 if $|P_2/P_1 - 2| \leqslant 0.01$, where we discuss this issue more quantitatively below. As outlined above, we first invoke the constraint that $P_2/P_1 \approx 2$. This fraction is shown as the dashed blue curves marked by squares in Figure 2.2. The four panels show the effects of including eccentricity damping (with $K = 1$, panels in top row) and turbulent forcing (with $(\Delta J)/J \sim 2 \times 10^{-4}$, panels on left side). Next we note that

each of the resonance angles can be either librating or circulating. For those that are librating, the range of angles (the libration width) is highly variable. For this Chapter we use the requirement that the resonance angles are confined to be within 120 degrees of the effective stability point (as defined above). With this specification, the corresponding fractions of systems in resonance are shown as the cyan curves (θ_1 angle), the red curves (θ_2 angle), and the green curves (θ_3 angle). The solid curves in each panel show the fraction of systems for which any of the resonance angles are librating at the end of the migration epoch. Note that only a relatively small fraction of the systems maintain resonance for the entire migration epoch. In addition, the inclusion of eccentricity damping (top panels) is crucial for the survival of resonant states.

For completeness, we note that the curves shown in Figure 2.2 have slightly different meanings for the different resonance angles. In order for any one of the angles to be considered in resonance, it must librate over (approximately) three libration periods. However, these periods are not the same for the three angles. In particular, the libration period for θ_3 is much longer than the other two. In addition, for this class of systems, the orbit of the outer (lighter) planet varies much more than that of inner Jovian planet. As a result, the argument of periastron of the outer planet can circulate on a long timescale, but the resonance angle θ_2 can still be considered (according to the criteria used here) to be librating.

In order to understand how the period ratios vary, we monitor the period ratio for systems that are found in 2:1 mean motion resonance. Monitoring is triggered by the condition that $P_2/P_1 < 2.05$; however, once triggered, this bound is relaxed and the period ratio for systems in resonance can take any value as long as the angles are librating (see above). We find that systems typically exhibit both a slight offset from exact commensurability and variations about this offset. The offset is typically less than $\sim 1\%$ and the standard deviation is $\sim 2\%$. We note that offsets and variations of this magnitude are expected, given the size of the terms in the disturbing function, and hence the size of the non-Keplerian velocities due to resonance. Both the offset value and amount of variation depend on the levels of damping and turbulence, and on the duration of resonance. In the absence of turbulence, we find an offset such that $P_2/P_1 \sim 2.008$. For systems that do not include eccentricity damping, the variation of the period ratio $\sigma \sim 0.04$, but decreases for systems that stay in resonance over long times (10 times the migration time scale τ_a). For cases with eccentricity damping parameter $K = 10$, the resonances are longer lasting, and we find $\sigma \sim 0.015$. For systems that include turbulent forcing, the period ratio $P_2/P_1 \sim 2.007$ with $\sigma \sim 0.07$

for short lived resonances, but decreases to $P_2/P_1 \sim 2.002$ with $\sigma \sim 0.015$ for longer lived resonances.

2.3.2.2 Resonance Survival

Figure 2.3 shows the effects of both turbulence and eccentricity damping on the survival of resonances as a function of migration rate. In this case, we define resonance using the requirement that the planets have nearly integer period ratios and the libration width is less than 120 degrees for any of the resonant angles. The lower right panel shows the survival of resonances as a function of migration rate with no eccentricity damping and no turbulence. This case is thus analogous to the model equations derived in Section 2.4 below. As expected, systems tend to leave resonance if the migration rate becomes too large. Here, systems leave the 2:1 resonance (blue curve) when the migration rate exceeds roughly 2×10^{-4} yr^{-1} ($\tau_a = 5000$ yr). After leaving the 2:1 resonances, systems can become locked into the 5:3 resonance (red curve), and/or the 3:2 resonance (green curve). Note that the curve for 2:1 resonances shows a broad maximum near the migration rate of 10^{-5} yr^{-1} ($\tau_a = 0.1$ Myr), with decreasing probability towards both slower and faster rates. The decrease with increasing migration rate is expected. The decrease toward slower migration rates occurs because some of the systems are locked into higher order resonances, which include the 7:3 and the 9:4 mean motion resonances (these fractions are not shown in the figure). With the starting period ratio of 2.4, the systems must pass through these states to reach the 2:1 resonance; with extremely slow migration rates, these weak resonances can (sometimes) survive and thus reduce the probability of the systems entering the 2:1 resonance.

The effects of including turbulent fluctuations are shown by the analogous curves in the lower left panel. Turbulence only has a chance to act on long timescales, so that the simulations with long migration times (low migration rates) are affected the most. More specifically, for migration rates slower than about 10^{-5} yr^{-1} ($\tau_a =$ 0.1 Myr), turbulence has time to act, and the probability of maintaining a resonant configuration is lower, as shown on the left hand side of the plot. We note that with the inclusion of turbulence, the weak higher order resonances (7:3 and 9:4) generally do not survive (unlike the case of no turbulence in the lower right panel).

The effects of including eccentricity damping is shown by the top right panel, where we have taken $K = 1$ (so that eccentricity is damped on the same timescale that migration takes place; see equation [3.8]). The inclusion of this damping effect acts to preserve resonance – note that all of the survival fractions are higher when

$\dot{e} \neq 0$ than in the absence of damping. This effect is especially important for the long-term survival of the resonant states (compare the solid curves in the top panels with those in the bottom panels), especially for the case of the 2:1 resonance. The survival probabilities of the (weaker) 5:3 and 3:2 resonances are also enhanced by the inclusion of eccentricity damping, but the absolute values of these probabilities remain low. Keep in mind that these results correspond to $K = 1$; larger eccentricity damping rates lead to more dramatic consequences (see below).

When both turbulent forcing and eccentricity damping are included, we obtain the results shown in the upper left panel of Figure 2.3. In this case, the effects of turbulence dominate at low migration rates, so that fewer resonant systems survive. At high migration rates, however, turbulence does not have sufficient time to act and the effects of eccentricity damping lead to a net gain in the survival fractions. For migration rates faster than about 3×10^{-5} yr^{-1} ($\tau_a \approx 0.033$ Myr), eccentricity damping dominates over the effects of turbulence, so that more resonant systems survive.

For comparison, we consider the survival of resonant systems for the case with eccentricity damping parameter $K = 10$. These results are shown in Figure 2.4, where all of the system parameters are the same as in Figure 2.3 except for the larger rate of eccentricity damping. As expected (e.g., Lecoanet et al., 2009), the simulations with $K = 10$ result in a larger survival rate than the corresponding cases with $K = 1$ (compare the upper right panels of Figures 2.4 and 2.3). For slower migration rates, where the dominant outcome is the 2:1 resonance (blue curves), the survival rate increases only modestly, from $P_b \sim 0.6$ to $P_b \sim 0.8$ with increasing values of K (for the case with no turbulence). For higher migration rates, the 3:2 resonance is most common state, and the survival rate increases substantially for the $K = 10$ case (compared to $K = 1$ systems). For the simulations that include turbulent fluctuations, however, the differences in survival fractions for the 2:1 resonance between the $K = 10$ and $K = 1$ cases are minimal (compare the upper left panels of Figures 2.3 and 2.4). In the absence of turbulence, the increase in resonance survival (for larger K) arises most strongly at slow migration rates; however, the regime of slow migration is where turbulence has enough time to act, and hence to compromise resonant states. For 3:2 resonances, which arise primarily at fast migration rates where turbulence does not have enough time to act, the increased eccentricity damping rate leads to substantially larger survival fractions.

Before leaving this section, we note that the simulations shown thus far all start with the planets confined to the orbital plane. In order to see how nonzero inclination

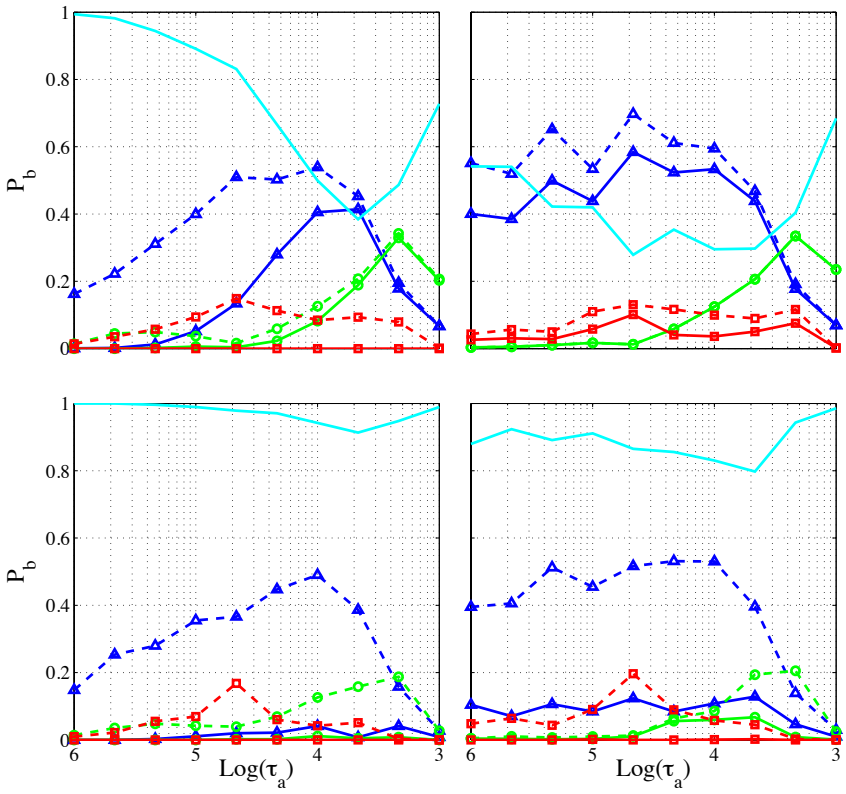

Figure 2.3: Effects of eccentricity damping and turbulent forcing on the survival of mean motion resonances for a two planet system. The inner planet has mass $m_1 = 1M_J$, and the outer planet has mass $m_2 = 10M_\oplus$. The two panels in the left column include turbulent forcing. The panels in the top row include eccentricity damping, which acts on the same timescale as the migration rate (eccentricity damping parameter $K = 1$). The lower right panel shows the results with migration only. The dashed curves show the fraction of systems that enter into mean motion resonance as a function of migration rate (τ_a measured in yr), where this fraction is measured using the peak value (as a function of time – see the curves of Figure 2.1). The solid curves show the fraction that remain in resonance at the end of the migration epoch. The colors denote the various resonances, including the blue curve marked by triangles (2:1), red curve marked by squares (5:3), and green curve marked by circles (3:2). The upper cyan curve shows the fraction of systems that are not in resonance at the end of the simulations.

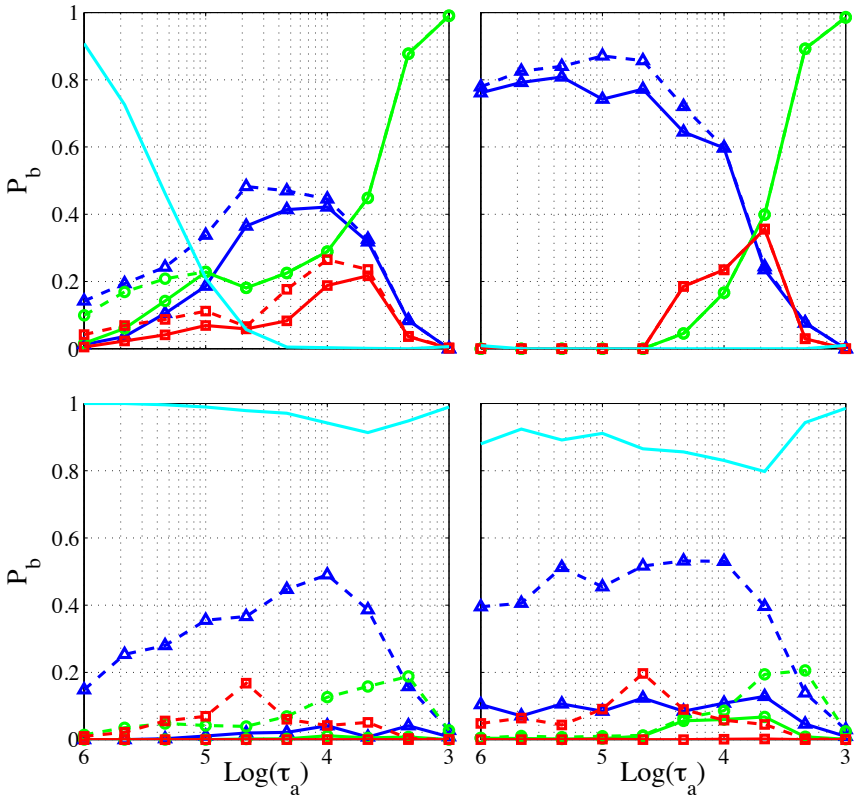

Figure 2.4: Effects of eccentricity damping and turbulent forcing on the survival of mean motion resonances for a two planet system with eccentricity damping parameter $K = 10$. Other properties are the same as in Figure 2.3: The planet masses are $m_1 = 1M_J$ and $m_2 = 10M_\oplus$. The panels in the left column include turbulent forcing. The panels in the top row include eccentricity damping with $K = 10$. The lower right panel shows the results with migration only. The dashed curves show the fraction of systems that enter into mean motion resonance as a function of migration rate. The solid curves show the fraction that remain in resonance at the end of the migration epoch. The colors denote the various resonances, including the blue curve marked by triangles (2:1), red curve marked by squares (5:3), and green curve marked by circles (3:2). The upper cyan curve shows the fraction of systems that are not in resonance at the end of the simulations.

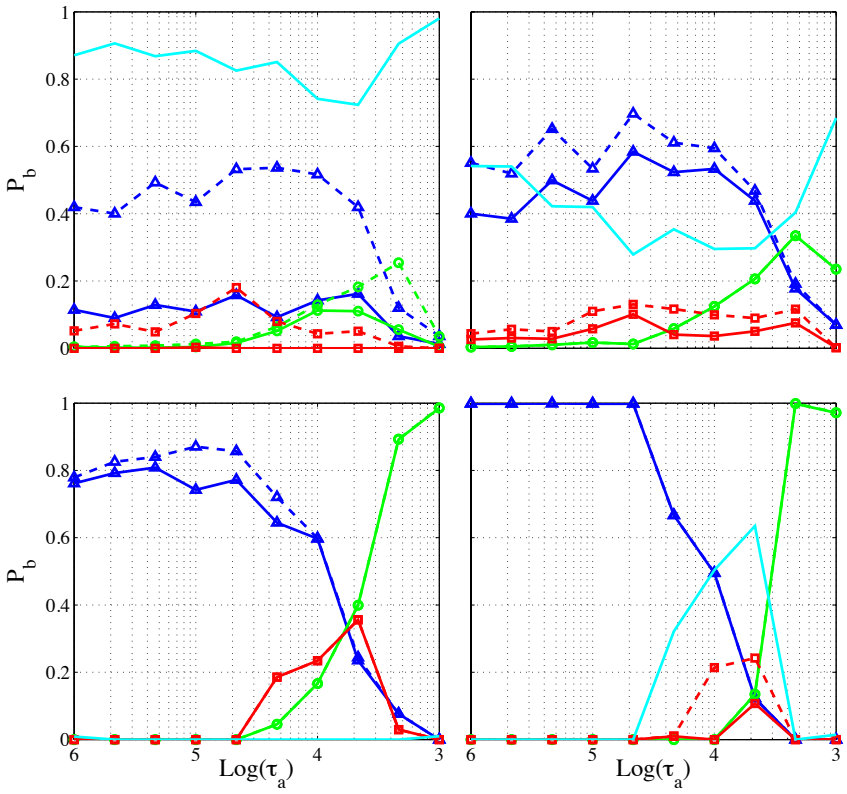

Figure 2.5: Effects of eccentricity damping on the survival of mean motion resonance. This two-planet system has planetary masses of $m_1 = 1M_J$ and $m_2 = 10M_\oplus$. The four panels show the survival fractions as a function of migration rate for increasing values of the eccentricity damping parameter K where $\dot{e}/e = K\dot{a}/a$. Results are shown for $K = 0.1$, 1, 10, and 100, where the K values increase from upper left to lower right. In each panel, the curves correspond to various resonances, including the blue curve marked by triangles (2:1), red curve marked by squares (5:3), and green curve marked by circles (3:2). The unmarked cyan curve shows the fraction of systems that are not found in any of the mean motion resonances. The solid curves show the fraction of systems in resonance at the end of the migration epoch; the dashed curves show the largest value of the fractions during the migration epoch.

angles affect the results, we have carried out a series of test simulations where the planets are given non-zero displacements in the vertical dimension in their starting states (so that these simulations are fully three-dimensional). The results of these test simulations indicate that the third dimension is unimportant as long as the initial departures from the plane are not too large. More specifically, the starting vertical coordinates z_0 are uniformly sampled within the range $[-H, H]$, where H is the scale height of the disk. These test simulations use a variety of scale heights, with $H/r = 0$, 0.05, 0.10, and 0.20; we also use a 10 $M_\oplus$ outer planet, eccentricity damping parameter $K = 10$, and our standard level of turbulence. For this choice of parameters, the results are virtually unchanged.

2.3.2.3 Effects of Eccentricity Damping and Turbulence

Next we consider the case of eccentricity damping acting alone. Figure 2.5 shows the survival probabilities as a function of migration rate for four values of the eccentricity damping timescale, where the parameter $K = 0.1$, 1, 10, and 100. Taken together, the four panels of Figure 2.5 show that eccentricity damping acts to increase the fraction of systems that remain in mean motion resonance. The effect is most pronounced for the 2:1 resonance, and for slow migration rates. In the regime of slow migration, a significant fraction of the systems leave the 2:1 resonance, presumably through the excitation of eccentricity via planet-planet interactions (Adams & Laughlin, 2003; Moorhead & Adams, 2005; Chatterjee et al., 2008; Ford & Rasio, 2008; Matsumura et al., 2010). The inclusion of eccentricity damping counteracts this excitation and allows more systems to remain in resonance.

For sufficiently large eccentricity damping rates (characterized by $K = 100$), essentially all systems remain in 2:1 resonance until the migration rate exceeds a well-defined value, found numerically to be $|\dot{a}|/a \sim 3 \times 10^{-5}$ yr^{-1} or $\tau_a \approx 0.033$ Myr (shown in the lower right panel of Figure 2.5). These results show that the loss of resonant states for the other cases (5:3 and 3:2) also occurs at well-defined values of the migration rate. In addition, as a rough approximation, the migration rates at which these three resonances are compromised are found to be evenly spaced logarithmically (by factors of ~ 3). This behavior can be understood in a qualitative manner through simple physical considerations (see below) and through model equations (Section 2.4). Finally, we note that the 5:3 resonance, which is second order and hence weak, is sparsely populated; as a result, many of the systems with migration time scales ~ 3000 yr are not found in any resonance.

The basic clock that determines the dynamics of these planetary systems is set by

the libration timescale of the resonance. For the simplest model of the resonance, that resulting from the circular restricted three-body problem, the frequency for external resonances is given by

$$\omega_0^2 = -3j_1^2 \mathcal{C}_R n e^{|j_3|} \qquad \text{where} \qquad \mathcal{C}_R = \left(\frac{m_P}{M_*}\right) n \left[f_d(\alpha) + \alpha^{-1} f_i(\alpha)\right] , \tag{2.10}$$

where n is the mean motion of the outer planet, $\alpha = a_1/a_2$, and the functions $f_d(\alpha)$ and $f_i(\alpha)$ are given by the Laplace coefficients (see §8.5 of MD99). For odd order resonances, the function $f_d < 0$, so that the corresponding frequencies are real. For even order resonances, $f_d > 0$, but the equilibrium angle is shifted by π, and the frequencies are again real (see MD99 for further discussion). Notice also that f_i is nonzero only for the 2:1 resonance. The integers j_1 and j_3 depend on the type of resonance. Although both integers are negative for the cases of interest, the libration timescale only depends on the absolute value. More specifically, the integer pair $(|j_1|, |j_3|)$ takes on the values (1,1), (3,2), and (2,1) for the 2:1, 5:3, and 3:2 resonances, respectively. For the values $e = 0.10$ and $\mu = m_P/M_* = 10^{-3}$, as used in the numerical simulations, we find that $\omega_0^2/(3\mu e n^2) \approx 2.0$, 3.0, and 8.1 for the three resonances. For these parameter values, the *square* of the frequencies are spaced by factors of ~ 2. This simple analytic result is thus in qualitative, but not quantitative, agreement with the numerical results. One should keep in mind that the orbital elements that enter into these formulae (e.g., e and n) vary over the course of the simulations, so that comparisons are complicated.

If the migration rate $\dot{a}/a$ were the only relevant variable, then one would expect that capture into resonance would be compromised at a fixed value of the dimensionless parameter $a\omega_0 \ / \ |\dot{a}| = \omega_0 \tau_a$. The case that most closely meets this expectation is that of migration with no eccentricity damping and no turbulent forcing (shown in the lower right panel of Figure 2.3). For this class of simulations, systems tend to enter the 3:2 resonance states for higher migration rates than for the 2:1 resonances, where this trend is predicted (qualitatively) by the simple theory outlined above. However, the fraction of systems in 5:3 resonance is not larger than the fraction in 2:1 resonance at large migration rates, in spite of the 5:3 having a shorter libration period. The 5:3 resonance is generally weaker, in the sense of being easier to disrupt, than the first order resonances, and does not survive for large migration rates. In terms of survival of the resonances, shown by the solid curves, the fraction in 2:1 is generally larger for all migration rates due to its greater stability.

For the case of migration with large eccentricity damping rates (see the lower

right panel of Figure 2.5), the probability of resonance survival shows the expected qualitative behavior: Each of the resonances dominates (has the largest fraction) for a well-defined range of migration rates. The 2:1 resonance is by far the most important for migration timescales longer than about 10^4 yr. For shoter timescales, there is a narrow window of migration rates where the fraction of systems in 5:3 resonance shows a peak, and then the 3:2 resonance dominates for faster migration rates. Although the ordering of these results is consistent with theoretical expectations, the maximum migration rates are spaced at larger intervals than the factors of $\sqrt{2}$ suggested by the above analysis. Here, the large eccentricity damping rates significantly change the dynamics and hence the numerical values. Nonetheless, the qualitative trend holds up.

As the levels of turbulence increase, systems have greater difficulty maintaining mean motion resonance. This trend is quantified by the simulations depicted in Figures 2.6 and 2.7. These numerical experiments are carried out using the standard case of a Jovian planet on the inside and an inward migrating "super-earth" with mass $m_2 = 10\ M_\oplus$. The eccentricity damping rate is set at the standard values of $K = 1$ (Figure 2.6) and $K = 10$ (Figure 2.7). As the amplitude of the turbulent fluctuations increases (from upper left to lower right in both Figures), the general trend is for the fraction of systems in resonance to decline significantly. The 2:1 mean motion resonance, which is the strongest and the first to be encountered, is compromised for sufficiently rapid migration rate. As the level of turbulence increases, the migration rate at which systems leave the 2:1 resonance becomes lower (the curves shift to the right in the figures). We also note that the destructive action of turbulence is more pronounced for the solid curves, i.e., for the fraction of systems that remain in resonance at the end of the migration time. Finally, as expected, we find that more resonant systems survive for larger rates of eccentricity damping (compare Figures 2.6 and 2.7).

With the initial conditions used herein, where the planets are started outside the 2:1 resonance, the faster 5:3 and 3:2 resonances are not affected as severely by the presence of turbulence. These other resonances only arise when the migration rate is rapid, so that the migration timescale is short and turbulence has little time to act. For the 5:3 and 3:2 resonances, the probability curves shown in Figure 2.6 decrease slowly with increasing turbulent amplitude. As expected, the largest effect arises for the largest turbulent amplitude $[(\Delta J)/J]_k = 10^{-3}$, where the probability of remaining in any of the resonant states is extremely low at the end of the migration epoch; the fraction of systems not bound into resonance is marked by the solid cyan curve, which

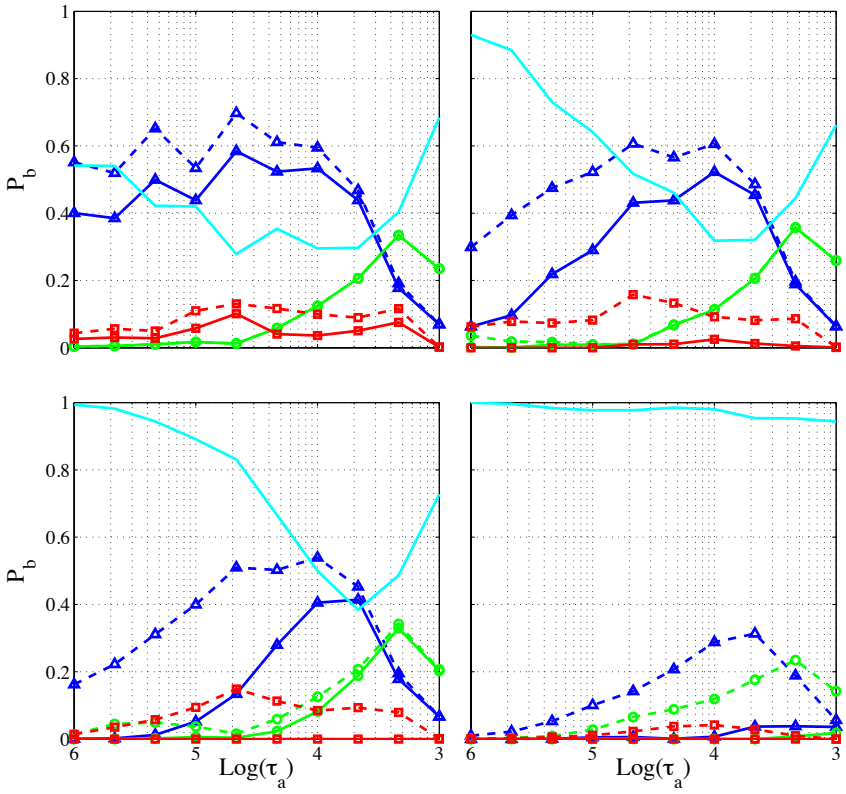

Figure 2.6: Effects of increasing turbulence on the survival of mean motion resonance. This two-planet system has planetary masses of $m_1 = 1M_J$ and $m_2 = 10M_\oplus$. The four panels show the survival fractions as a function of migration rate for increasing levels of turbulence, as specified by the forcing strength $[(\Delta J)/J]_k$ per independent realization of the turbulent fluctuations. Results are shown for $[(\Delta J)/J]_k = 0$ (no turbulence), 10^{-4}, 3×10^{-4}, and 10^{-3}, where turbulence increases from upper left to lower right. In each panel, the curves correspond to various resonances, including the blue curves marked by triangles (2:1), red curves marked by squares (5:3), and green curves marked by circles (3:2). The unmarked cyan curves show the fraction of system that are not found in any of the mean motion resonances. The solid curves show the fraction of systems in resonance at the end of the migration epoch; the dashed curves show the largest value of the fractions during the migration epoch. The eccentricity damping parameter $K = 1$ for these simulations.

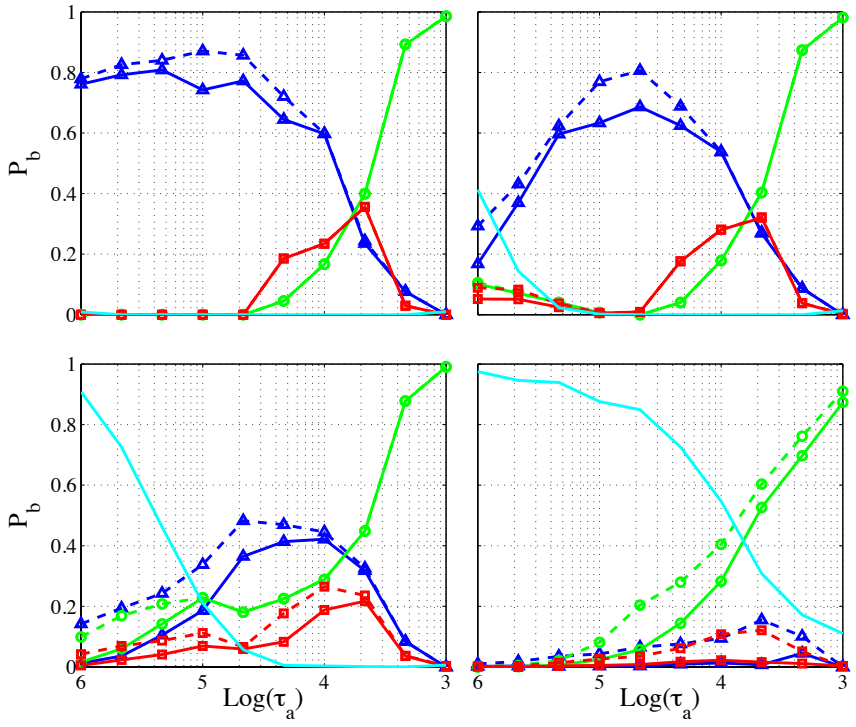

Figure 2.7: Effects of increasing turbulence on the survival of mean motion resonance for systems with eccentricity damping parameter $K = 10$. Other system properties are the same as in Figure 2.6. This system has planet masses $m_1 = 1M_J$ and $m_2 = 10M_\oplus$. The four panels show the survival fractions as a function of migration rate for increasing levels of turbulence. Results are shown for forcing strength $[(\Delta J)/J]_k = 0$, 10^{-4}, 3×10^{-4}, and 10^{-3}, where turbulence increases from upper left to lower right. In each panel, the curves correspond to various resonances, including the blue curves marked by triangles (2:1), red curves marked by squares (5:3), and green curves marked by circles (3:2). The unmarked cyan curves show the fraction of system that are not found in any of the mean motion resonances. The solid curves show the fraction of systems in resonance at the end of the migration epoch; the dashed curves show the largest value of the fractions during the migration epoch.

is close to unity for all migration rates. Note that the 3:2 resonance lasts the longest in the face of increasing turbulence. This apparent resilience arises because the 3:2 cases are only present for fast migration rates, the regime where turbulence has less time to act (it is not due to the increased durability of the resonance).

2.3.2.4 Equal Mass Planets

Next we consider the case of two equal mass planets, with $m_1 = m_2 = M_J$. The results for survival of mean motion resonance are shown in Figure 2.8. The panels on the left include the effects of turbulent forcing; the panels on the top include the effects of eccentricity damping, where the parameter $K = 1$ so that the eccentricity damping timescale is the same as the migration timescale. These results for two Jovian planets are significantly different than those shown in Figure 2.3 for the case of a lower mass outer planet. One important effect of higher planetary masses is to increase the levels of planet-planet interactions in the systems. This effect, in turn, leads to greater libration widths for systems that stay in resonance and a lower probability of remaining in a resonant state. As a result, the probability of the system residing in either the 5:3 or the 3:2 resonance is significantly lower than in the case of a less interactive system (compare Figures 2.3 and 2.8). On the other hand, the fraction of systems that remain in the 2:1 resonance is larger for the more interactive (two jupiter) systems.

2.3.3 End States

During the course of the numerical integrations, the planetary systems can end their evolution in a variety of ways. In many cases, the systems remain bound together, even though mean motion resonance is often compromised as described above. In many other cases, however, planets can be lost through scattering encounters, through collisions with each other, or via accretion onto the central star. This section outlines the probabilities for each of these possible end states of these dynamical systems.

For eccentricity damping parameter $K = 1$, Figure 2.9 shows the likelihood of the planetary systems ending their evolution in various possible end states for the standard case with inner planet mass $m_1 = 1M_J$ and outer planet mass $m_2 = 10M_\oplus$. These probabilities are shown as a function of migration rate for ensembles of simulations with migration only, migration and eccentricity damping, migration and turbulence, and for simulations including all three effects. The evolution of these

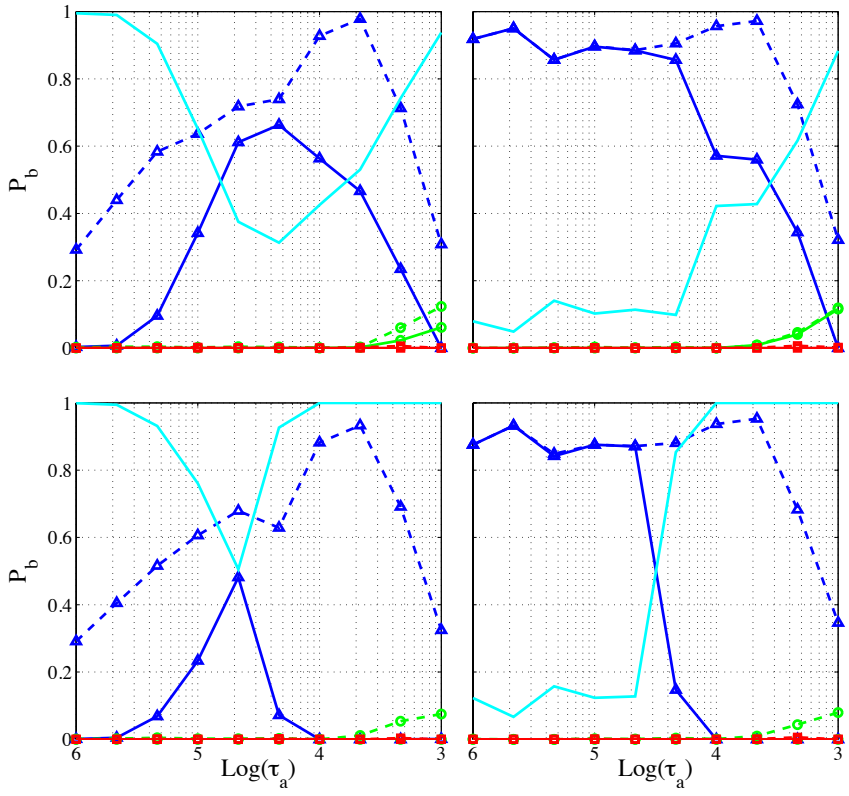

Figure 2.8: Effects of eccentricity damping and turbulent forcing on the survival of mean motion resonances for planetary systems containing two Jovian planets ($m_1 = m_2 = 1M_J$). The panels on the left include turbulent forcing; the top panels include eccentricity damping (where the eccentricity damping parameter $K = 1$). The lower right panel shows the results with migration only. All of the panels show the fraction of systems that remain bound in mean motion resonance as a function of migration time scale (measured in yr). The curves correspond to various resonances, including the blue curves marked by triangles (2:1), red curves marked by squares (5:3), and green curves marked by circles (3:2). The unmarked cyan curve shows the fraction of system that are not found in any of the mean motion resonances. Solid curves show the fractions at the end of the migration epoch; dashed curves show the peak values of the fractions during the migration epoch.

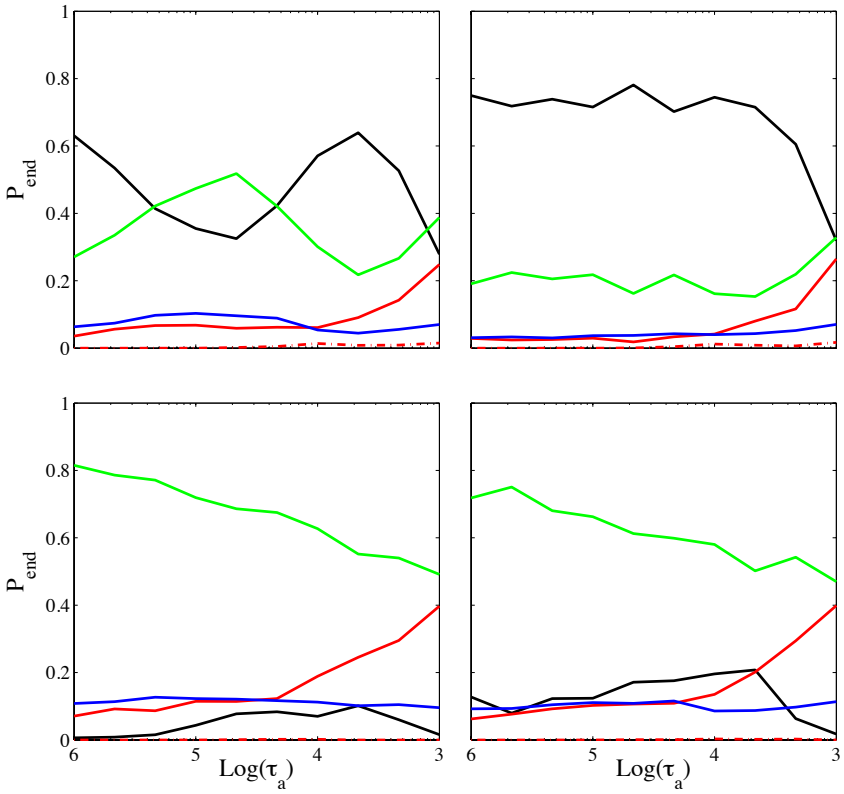

Figure 2.9: Probability of the planetary systems evolving into varying end states for planet masses $m_1 = 1M_J$ and $m_2 = 10M_\oplus$. Each panels shows the fraction of the systems that end their evolution with a given end state, plotted here as a function of migration rate. The end states represented here include survival of both planets (black curves), planetary collisions (blue curves), ejection of a planet (green curves), and accretion of a planet by the central star (red curves). Four ensembles of simulations are depicted for migration only (lower right panel), migration and eccentricity damping (with $K = 1$; upper right), migration and turbulence (lower left), and all three effects (upper left).

systems produces a wide variety of outcomes, including survival of both planets for the entire evolutionary time (shown by the black curves), ejection of a planet (green curves), accretion by the central star (red curves), and collisions between the planets (blue curves). As illustrated by the four panels in the figure, the corresponding probabilities depend sensitively on the migration rates, eccentricity damping rates, and the levels of turbulence.

Figure 2.9 shows several trends. In general, the probability for both planets to survive tends to decrease with increasing values of the migration rate. This trend is expected, because slow migration rates allow the systems to adjust as they evolve; these cases with slow migration systematically exhibit less overall action than cases with higher migration rates. One important exception to this trend arises for the case of slow migration rates, the inclusion of turbulent fluctuations, and no eccentricity damping (see the lower left panel in Figure 2.9). In this regime, migration time scales are long enough that turbulence has time to act, which leads to loss of mean motion resonance (see the previous section), a greater possibility of orbit crossing, and subsequent planetary ejection. For this class of systems, the outer planet has substantially less mass than the inner planet and is far more susceptible to being lost. The outer planet is removed through ejection, accretion onto the central star, and through collisions with the inner Jovian planet. Note that the first two of these channels dominate the third.

Figure 2.9 shows another trend: As the migration rate increases, the probability of losing a planet through ejection decreases, whereas the probability of losing a planet through accretion onto the star increases. One important physical property that determines the relative number of accretion events versus ejections is the location of the planet(s) in the gravitational potential well of the star at the end of the migration epoch (when the planets are likely to suffer close encounters). The depth of the stellar potential well at $a = 1$ AU is approximately $(30 \text{ km/s})^2$, whereas the depth of the potential well at the surface of Jupiter is $(43 \text{ km/s})^2$. These scales are thus comparable. For fast migration rates, the outer planet is able to push the inner planet somewhat farther inward, deeper into the stellar potential well, and hence the probability of ejection decreases.

Figure 2.10 shows the analogous plots for the channels of planetary loss for systems initially containing two Jovian planets ($m_1 = m_2 = 1 M_J$). The trends are roughly similar to the case with lower mass outer planets: Planetary survival decreases with increasing migration rate. Turbulence leads to planetary loss in the regime of slow migration and no eccentricity damping, where the regime of slow migration corresponds

to migration time scales longer than about $\tau_a = 3 \times 10^4$ yr. And, as the migration rate increases, there is a shift from loss of planets through ejection to a loss of planets through accretion onto the central star. However, for these systems with two Jovian planets, ejections, collisions, and accretion events are on a more equal footing. One clear difference from the case of low-mass outer planets is that planet-planet collisions are more common (compare the blue curves in Figures 2.9 and 2.10). The other significant difference is that the inner planet is more often lost during accretion events, rather than the outer planet (shown by the dotted curves in Figure 2.10).

For solar systems with sufficiently large values of the eccentricity damping parameter K, most of the planets survive over the relatively short timescales considered in this Chapter. For example, for cases with $K = 10$, most systems remain intact and neither eject nor accrete a planet. However, as shown by the comparison of Figures 2.3 and 2.4, the fraction of systems that remain in mean motion resonance for $K = 10$ is only moderately increased over the values obtained for $K = 1$. The solar systems that are not in resonance will often eject or accrete planets on longer timescales, even in the absence of additional migration (e.g., Holman & Wiegert, 1999; David et al., 2003). This issue should be addressed with additional, longer term numerical integrations, but is beyond the scope of this present work.

2.4 Model Equations

In this section we derive a Hamiltonian model to describe the migration of a pair of planets into mean motion resonance. In this context, we want to find the simplest possible set of model equations that captures the essential physics. Toward this end, we make a number of simplifying assumptions. In particular, most of this discussion is restricted to the case of a single resonance, which we take to be the 2:1 mean motion resonance; note that other resonances can be considered in similar fashion. In qualitative terms, this analysis should apply to the variety of resonances that we consider in the numerical simulations of Section 2.3. The development is parallel to previous treatments (Quillen, 2006; Friedland, 2001).

2.4.1 Derivation

As a starting point, we consider a test particle of mass m_0 orbiting in the same plane as a larger planet with mass m_P, which is orbiting a star of mass M_*. The

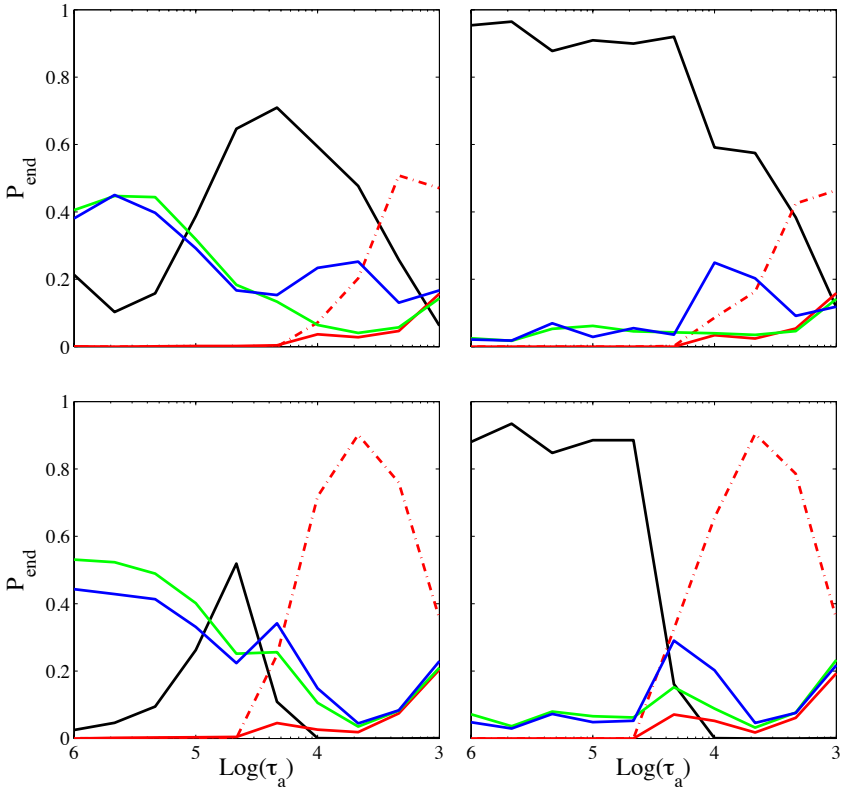

Figure 2.10: Probability of the planetary systems evolving into varying end states for planet masses $m_1 = m_2 = 1M_J$. Four ensembles of simulations are depicted for cases with migration only (lower right panel), migration and eccentricity damping (upper right), migration and turbulence (lower left), and all three effects (upper left). The end states represented here include survival of both planets (black curves), planetary collisions (blue curves), ejection of a planet (green curves), and accretion of a planet by the central star (red curves).

masses thus obey the ordering

$$m_0 \ll m_P \ll M_* \,. \tag{2.11}$$

The orbital elements of the test particle are as follows: λ is the mean longitude, M is the mean anomaly, a is the semi-major axis, ϖ is the longitude of pericenter, and e is the orbital eccentricity. The analogous variables for the planet have the same symbols but are denoted with the subscript 'P' (see below). The Poincaré coordinates (MD99) can be written

$$\lambda = M + \varpi \qquad \text{and} \qquad \widetilde{\gamma} = -\varpi \,, \tag{2.12}$$

with momentum variables of the form

$$\ell = (GM_* a)^{1/2} \qquad \text{and} \qquad \Gamma = (GM_* a)^{1/2} \left[1 - (1 - e^2)^{1/2} \right] . \tag{2.13}$$

The Hamiltonian can be written in the form

$$H = -\frac{(GM_*)^2}{2\ell^2} - \mathcal{R} \,, \tag{2.14}$$

where $\mathcal{R}$ is the disturbing function due to the gravitational interaction between the test particle and the planet.

Specializing to the case of a 2:1 mean motion resonance where the planet is the inner body, we perform a canonical transformation using the generating function

$$F_2 = I(2\lambda - \lambda_P) \,, \tag{2.15}$$

which leads to the new variables

$$I = -\ell/2 \qquad \text{and} \qquad \psi = \lambda_P - 2\lambda \,. \tag{2.16}$$

The new Hamiltonian for the unperturbed problem, without the disturbing function, has the form

$$H_{0;new} = -\frac{(GM_*)^2}{8I^2} - I n_P \,, \tag{2.17}$$

where n_P is the mean motion of the planet.

Next we express all quantities in dimensionless form and expand around the resonance. Here, distances are measured in units of the semimajor axis a, time is measured

in units of $(a^2/GM_*)^{1/2}$, and mass is measured in units of M_*. If we define

$$\delta \equiv I - I_0 \qquad \text{and} \qquad \frac{1}{4I_0^3} = n_P(t_0)\,, \tag{2.18}$$

the new Hamiltonian now reads

$$K_{0;new} = constant - (n_P - 1)\delta - \frac{3\delta^2}{8I_0^4}\,. \tag{2.19}$$

We must now include the relevant terms from the disturbing function, which provides an expansion in orders of eccentricity (of both the test mass and the planet). Here we keep only the leading order term (see MD99 and Quillen 2006) and write the Hamiltonian (from equation [2.19]) in the form

$$K(\delta, \psi, \Gamma, \widetilde{\gamma}) = -6\alpha^2\delta^2 - (n_P - 1)\delta - 2\mu f_2 \alpha^{1/2}\Gamma + A\Gamma^{1/2}\cos(\psi - \varpi)\,, \tag{2.20}$$

where A is the expansion coefficient in the disturbing function and where we have used the fact that $I_0 = \alpha^{-1/2}/2$ for these units and choice of resonance.

Following Quillen (2006), we perform another canonical transformation using the generating function

$$F_2 = J_1(\psi - \varpi) + J_2\psi\,, \tag{2.21}$$

which leads to the new variables

$$J_1 + J_2 = \delta\,, \qquad \phi = \psi - \varpi\,, \qquad J_1 = \Gamma\,, \qquad \text{and} \qquad \theta = \psi\,, \tag{2.22}$$

and hence the new Hamiltonian

$$H = -6\alpha^2\left(\Gamma^2 + J_2^2\right) - \left[12\alpha^2 J_2 + (n_P - 1) + 2\mu f_2\alpha^{1/2}\right]\Gamma - (n_P - 1)J_2 + A\Gamma^{1/2}\cos\phi\,. \tag{2.23}$$

Since J_2 is conserved and constant terms can be dropped, the Hamiltonian can be simplified to the form

$$H = 6\alpha^2\Gamma^2 + \left[12\alpha^2 J_2 + (n_P - 1) + 2\mu f_2\alpha^{1/2}\right]\Gamma - A\Gamma^{1/2}\cos\phi\,. \tag{2.24}$$

Next we rescale the momentum variable Γ according to the transformation

$$\Gamma \to \left[\frac{6\alpha^2}{A}\right]^{2/3}\Gamma\,, \tag{2.25}$$

and rescale the time variable so that the Hamiltonian H is given by

$$H = \Gamma^2 + b\Gamma - \Gamma^{1/2}\cos\phi\,. \tag{2.26}$$

The parameter b is thus given by

$$b = \left[12\alpha^2 J_2 + (n_P - 1) + 2\mu f_2 \alpha^{1/2}\right] 6^{-1/3}(\alpha A)^{-2/3}\,. \tag{2.27}$$

The first and third terms in square brackets are generally small compared to unity. The central term vanishes on resonance, by definition, but can be of order unity when the system is far from resonance. As a result, the parameter b provides a measure of how far the system resides from a resonant condition. For this Chapter, we let the parameter b evolve linearly with time so that the systems approach resonance ($b = 0$) at a well-defined rate.

Using the Hamiltonian with the form given by equation (2.26), the equations of motion become

$$\frac{d\Gamma}{dt} = -\Gamma^{1/2}\sin\phi\,, \tag{2.28}$$

and

$$\frac{d\phi}{dt} = 2\Gamma + b - \frac{1}{2\Gamma^{1/2}}\cos\phi\,. \tag{2.29}$$

It is useful to define the reduced momentum variable $p \equiv \Gamma^{1/2}$ so that the equations of motion simplify to the forms

$$2\frac{dp}{dt} = -\sin\phi\,, \tag{2.30}$$

and

$$\frac{d\phi}{dt} = 2p^2 + b - \frac{1}{2p}\cos\phi\,. \tag{2.31}$$

Although this ansatz simplifies the equations of motion, note that the variables (ϕ, p) are no longer canonical. We also note that this change of variables in convenient for calculating curves in phase space to analyze the dynamics (this exercise is carried out in the Appendix).

2.4.2 Entry into Resonance

Using the model equations derived above, we can study the entry into mean motion resonance as a function of the normalized migration rate db/dt. Here, the initial conditions are given by the starting momentum Γ_0 and the starting value of the

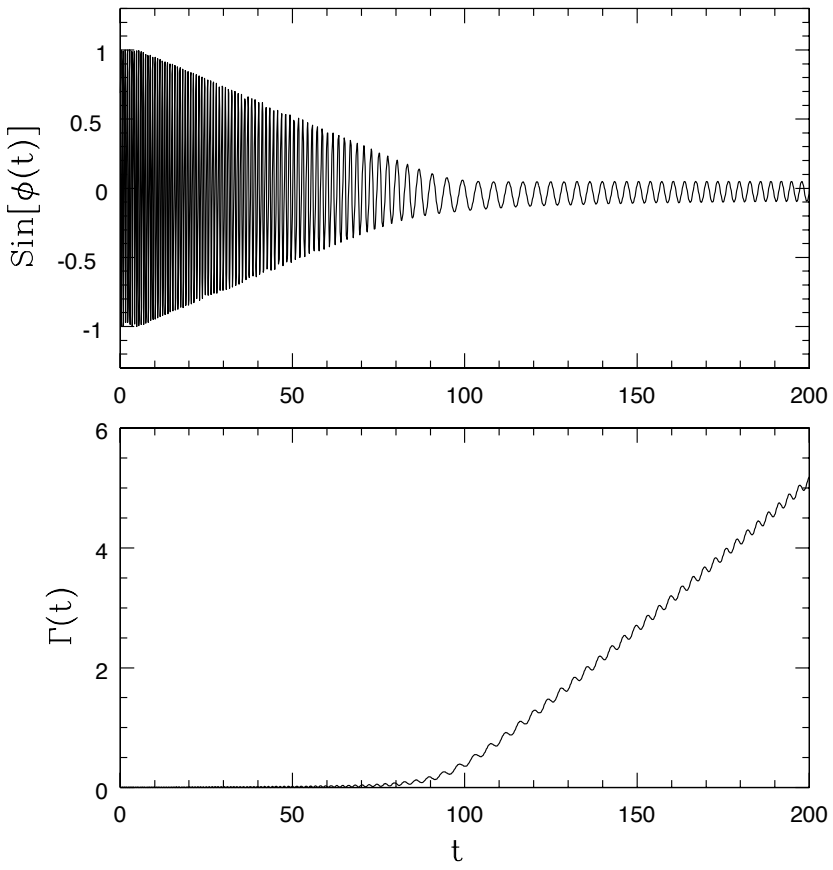

Figure 2.11: Time evolution of the resonance angle for a model system that becomes trapped in resonance. The top panel shows the variable $\sin[\phi(t)]$ versus time, for a starting value of $\Gamma_0 = 0.01$ and a migration rate $db/dt = -0.1$. The bottom panel shows the time evolution of the momentum variable Γ.

angle ϕ. We choose fixed values of the momentum variable Γ_0 and then study the probability of entering into resonance as a function of migration rate db/dt. Since these systems often display extreme sensitivity to their starting conditions, we must perform many realizations of the numerical integrations for each pair $(\Gamma_0, db/dt)$, where each realization uses a different value of the starting angle ϕ. For the sake of definiteness, we start the systems with $b = b_0 = 10$ (well outside of resonance) and let the resonance parameter evolve according to the relation $b(t) = b_0 - (db/dt)t$. The systems thus pass through resonance at time $t = b_0/|db/dt|$.

One example integration is shown in Figure 2.11, which plots the quantity $\sin\phi$ (top panel) and the momentum variable Γ (bottom panel) as a function of time for a system that becomes locked into mean motion resonance. In this case, the libration width of the system steadily decreases with time until it reaches a steady state near time $t = 100$ (in dimensionless units). In this case, $db/dt = 0.1$, so that $t \sim 100$ corresponds to the time when the system passes through resonance (as expected). The momentum variable Γ stays small until the system enters resonance, and then grows steadily (see also the discussion of Quillen 2006).

As found previously (Quillen, 2006), the probability of entering and surviving in resonance decreases with increasing migration rate. This trend is illustrated in Figure 2.12, which shows the probability of achieving a resonant state versus the migration rate db/dt. The three curves shown in the figure use different starting values of the momentum variable $\Gamma_0 = 0.1$, 1, and 3. Recall that Γ is related to the orbital eccentricity of the migrating planet (equation [2.13]). Previous work shows that small starting momentum generally leads to resonance capture, whereas larger values generally do not (Quillen, 2006); the value $\Gamma_0 = 1$ corresponds to the transition region. For each value of the rate db/dt, we have performed an ensemble of 1000 integrations, each with a different starting value of the angular variable ϕ. The probability of capture decreases with increasing db/dt, but the curves show a great deal of additional structure. The probability of achieving resonance decreases near $db/dt = 1$ and approaches zero for somewhat larger values $db/dt \sim 3 - 5$.

Another clear trend is that increasing the initial value of the momentum variable Γ_0 acts to decrease the probability of entering into resonance. In other words, larger eccentricities tend to compromise the chances of attaining resonance. This finding is consistent with the full numerical integrations of the previous section, where eccentricity damping was found to allow for more resonant states (see Figure 2.5).

The leading order trend illustrated by Figure 2.12 is that resonant capture is more difficult with fast migration. This result, obtained from the model equations of this

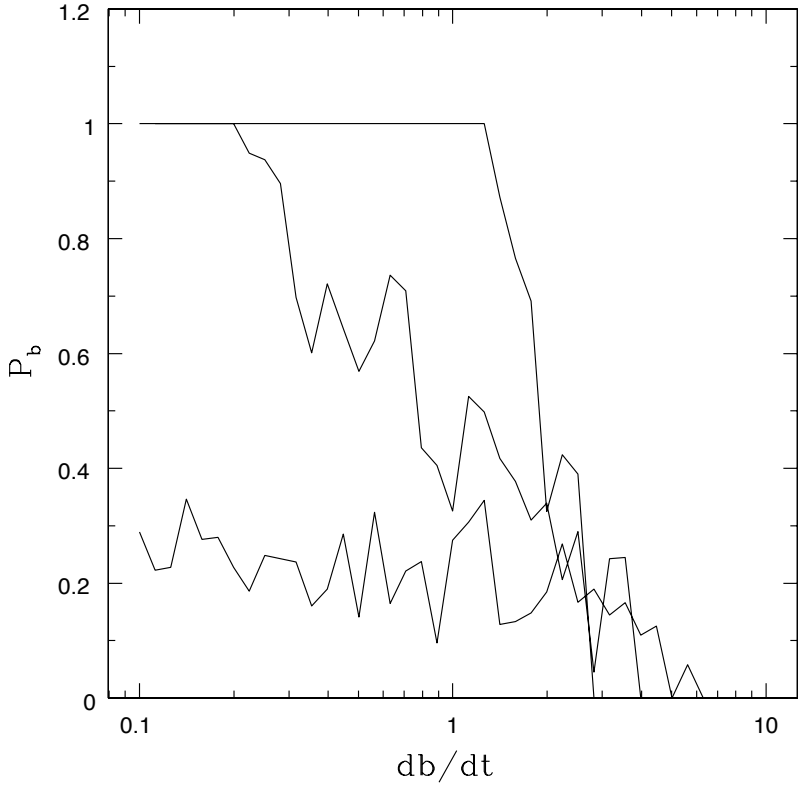

Figure 2.12: Fraction of systems that survive in mean motion resonance as a function of migration rate db/dt. The three curves correspond to different initial conditions, where the the angular momentum variable $\Gamma_0 = 0.1$ (top curve), 1 (center curve), and 3 (bottom curve). Each point on each curve shows the result of 1000 realizations of the evolution, each with a randomly chosen starting angle. Note that this model system corresponds to the case of the 2:1 mean motion resonance.

section, is thus consistent with the results of the numerical simulations of Section 2.3 (see Figures 2.2 – 2.8). We can understand this effect through a simple analysis: In the limit of large $db/dt = \gamma$, which we consider to be a constant, the equation of motion for ϕ simplifies to the form

$$\frac{d\phi}{dt} = -\gamma t \qquad \Rightarrow \qquad \phi = -\frac{1}{2}\gamma t^2 \,, \tag{2.32}$$

where we have used the same sign convention as before. The momentum variable is then given by the remaining equation of motion, which can be written in integral form

$$p - p_0 = \frac{1}{2}\int \sin\left(\frac{1}{2}\gamma t^2\right) dt = \frac{1}{(2\gamma)^{1/2}}\int \sin u^2 du = \frac{1}{2}\left(\frac{\pi}{\gamma}\right)^{1/2} S\left[\left(\frac{\gamma}{\pi}\right)^{1/2} t\right] \,, \tag{2.33}$$

where $S(z)$ is the Fresnel integral (e.g., Abramowitz & Stegun, 1965). In the limit $z \to \infty$, $S(z) \to 1/2$, so the expression on the right hand side of equation (2.33) approaches a constant value $(\pi/16\gamma)^{1/2}$. As result, the momentum variable p approaches a constant, and hence does not grow, so the system does not enter resonance. For a given starting value of the momentum variable Γ_0, the critical value of the migration rate γ can be estimated by

$$\gamma_c = \frac{\pi}{16\Gamma_0} \qquad \text{or} \qquad \gamma_c\,\Gamma_0 \approx 1/5 \,. \tag{2.34}$$

For comparison, in the set of simulations shown in Figure 2.12 with $\Gamma_0 = 1$, the probability of survival in resonance P_b falls below unity when the migration rate becomes greater than $\gamma = db/dt \approx 0.2$; P_b falls below 1/2 for $\gamma > 1$ and goes to zero for larger values.

Another trend present in Figure 2.12 is that small variations in the migration rate can significantly change the probability of resonant capture, especially for larger starting values of the momentum variable. The curves shown in the Figure display a great deal of variation with db/dt; if the curves were plotted with finer resolution in db/dt, the plot would show even greater variation (and would not show resolved oscillations). This sensitivity to the migration rate can be illustrated further by plotting the time evolution of two nearly identical systems, as shown in Figure 2.13. In this case, two systems are started with Γ_0, the same angle ϕ_0, and two different migration rates $db/dt = 0.300$ (solid curve) and $db/dt = 0.301$ (dashed curve). The evolution of the two systems is nearly identical until about halfway through the total

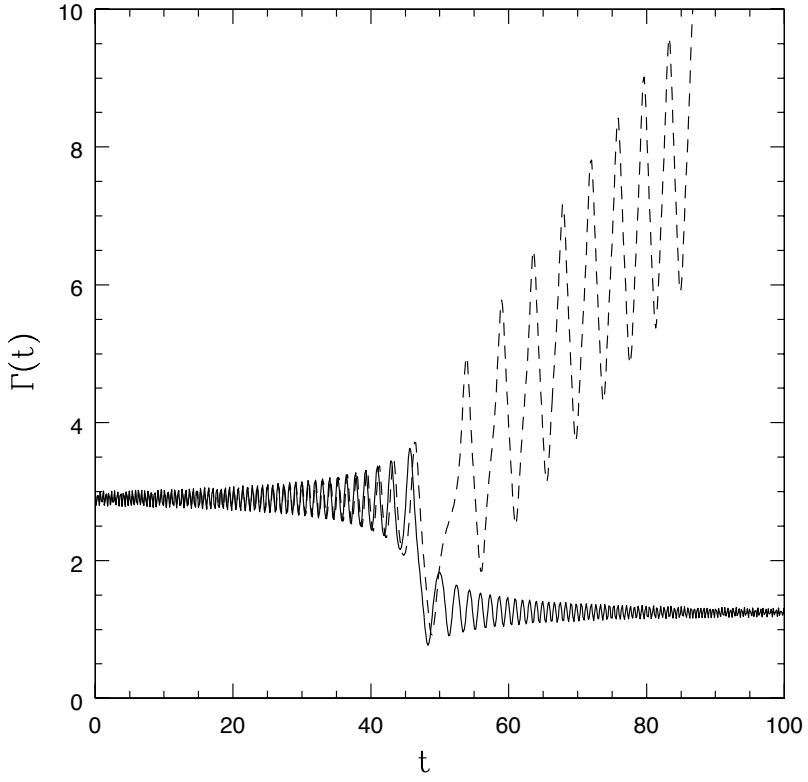

Figure 2.13: Comparison of the momentum evolution of two nearly identical systems. Both systems are started with the same values of the phase space variables (Γ_0, ϕ_0). The migration rates are taken to be $db/dt = 0.300$ (solid curve) and $db/dt = 0.301$ (dashed curve). This small difference in migration rate allows one system to enter into mean motion resonance (dashed curve), while the other continues to circulate (solid curve).

time interval, when the second system becomes locked into mean motion resonance (indicated by the growing values of Γ), whereas the first system continues to circulate with its momentum variable exhibiting a decreasing amplitude.

This effect can be (roughly) understood as follows: Suppose we consider circulating solutions such that $\phi \approx \omega t$. The equation of motion for the angle ϕ then implies that

$$\omega \sim 2p^2 + b - \frac{1}{2p}\cos\phi\,. \tag{2.35}$$

The corresponding solution for the reduced momentum variable p then becomes

$$p(t) \sim A + \frac{1}{2\omega}\cos\omega t\,, \tag{2.36}$$

where A is a constant. In this context, the parameter b starts at a positive value (outside resonance) and then decreases. The relation (2.35) indicates that ω must decrease with time, so that the amplitude of the oscillations of momentum increase with time as the frequency decreases. Near the point where $\omega \to 0$, however, the oscillation amplitudes are large and the frequency is small. The system must then match onto one of the possible solutions for late times when b is large and negative. One solution corresponds to $\omega \to b$ (see relation [2.35]); in this case, equation (2.36) indicates that the momentum variable will oscillate with increasing frequency and decreasing amplitude (shown by the solid curve in Figure 2.13). Although the momentum variable oscillates, the resonance angle circulates for this case. A second solution exists for sufficiently large p; in this case, the equation of motion (2.31) for the variable ϕ takes the approximate form

$$\frac{d\phi}{dt} \approx 2p^2 + b\,. \tag{2.37}$$

This equation can be combined with the momentum equation (2.30) to obtain the result

$$\frac{d^2\phi}{dt^2} + 2p\sin\phi + \frac{db}{dt} = 0\,, \tag{2.38}$$

which is a type of pendulum equation, and hence allows for librating solutions for the angle $\phi(t)$. This class of solution is depicted by the dashed curve in Figure 2.13.

2.5 Conclusions

This Chapter studies the entry of planetary systems into mean motion resonance, and the subsequent survival of resonant configurations, with a focus on how the migration rate, eccentricity damping rate, and turbulence levels affect the results. Our basic findings can be summarized as follows:

In agreement with previous studies, we find that an inward migrating planet naturally becomes locked into mean motion resonance when it becomes sufficiently close to an inner planet. If the migration rate is too fast, then mean motion resonance cannot be maintained. This trend arises in both full numerical integrations of the 3-body system with 18 phase space variables (Section 2.3), and in model equations (Section 2.4), in agreement with previous results (e.g., Quillen, 2006). In rough terms, the probability of staying in resonance is a decreasing function of the migration rate; this probability (effectively) vanishes when the migration rate exceeds the frequency of the resonant state. As the migration rate increases, the frequency of the resonances that the systems can maintain also increases. For example, the three strongest resonances considered here are the 2:1, 5:3, and 3:2, in increasing order of frequency. As the migration rate increases, the systems become more likely to pass through the 2:1 resonance and then become locked into the 5:3. For even larger migration rates, the systems cannot maintain 5:3 resonance but enter into the 3:2 resonance. Figures 2.3 – 2.8 all show this basic trend. This general trend continues to hold up in the presence of additional processes, such as eccentricity damping and turbulent forcing; however, the critical values of the migration rate change, as described below.

Eccentricity damping acts to maintain mean motion resonance (again, in agreement with expectations; see Lecoanet et al. (2009)). As a general rule, larger eccentricity damping rates result in more systems maintaining resonant configurations (see Figure 2.5). For a relatively non-interactive system (here we use $m_1 = 1 M_J$ and $m_2 = 10 M_\oplus$), a substantial increase in resonance survival is realized with eccentricity damping parameter $K \geqslant 1$, where roughly half the systems survive (Figure 2.3). This survival fraction increases to $P_b \sim 0.75$ for a larger eccentricity damping parameter $K = 10$ (Figure 2.4). In order to increase the probability of survival close to unity (for relatively "slow" migration rates with $\tau_a > 3 \times 10^4$ yr), the eccentricity damping parameter must be increased to about $K \geqslant 100$. This level of eccentricity damping can be realized in radiative disk models (e.g., Bitsch & Kley, 2010).

This work also shows that turbulence acts to compromise mean motion resonance, in agreement with previous studies (Adams et al., 2008; Lecoanet et al., 2009; Rein

& Papaloizou, 2009). Because turbulence, with the expected amplitudes, requires a long time to act, it primarily affects those systems with slow migration rates. We can define an effective timescale for turbulent fluctuations to affect resonances through the following heuristic argument. For a stochastic process, the system accumulates changes in angular momentum as a random walk; after N_S steps the angular momentum changes by $N_S^{1/2}(\Delta J)_k$, where $(\Delta J)_k$ is the typical angular momentum fluctuation per step. As an order of magnitude estimate, the angular momentum of the resonant configuration is given by $J_{orb}\omega_0/\Omega$, where ω_0 is the frequency of the resonance and J_{orb} is the orbital angular momentum. The number of steps required to compromise the resonance is then given by $N_S > [(\Delta J)_k/J_{orb}]^{-2}(\omega_0/\Omega)^2$. The time required for an independent realization of the turbulent fluctuations is approximately the orbit time, so that the corresponding time scale becomes

$$\tau_T \approx \frac{2\pi}{\Omega}\left[\frac{(\Delta J)_k}{J_{orb}}\right]^{-2}\left(\frac{\omega_0}{\Omega}\right)^2 \approx 3\times 10^4\,\mathrm{yr}\left[\frac{(\Delta J)_k/J_{orb}}{10^{-4}}\right]^{-2}, \tag{2.39}$$

where the second equality scales the result to the parameters used in this study. In order for turbulence to have a significant effect, the migration timescale must be longer than this value. As shown in Figures 2.6 and 2.7, turbulence compromises mean motion resonance for slower migration rates, more specifically for migration time scales $\tau_a = -a/\dot{a} > 10^5$ yr.

The above results can be summarized in terms of the four timescales in this problem: the migration timescale τ_a, the eccentricity damping timescale τ_e, the timescale τ_T for turbulence to act, and the libration timescale τ_R of the mean motion resonance. The relative ordering of these timescales determines much of the dynamics. The numerical integrations (Section 2.3), the model equations (Section 2.4), and previous work (Quillen, 2006) all show that planetary systems have difficulty entering and maintaining mean motion resonance when $\tau_a < \tau_R$. Eccentricity damping allows more resonances to survive provided that $\tau_e < \tau_a$ (see Figure 2.5 and Lecoanet et al. (2009)). On the other hand, turbulence acts to destroy resonances when $\tau_T < \tau_a$ (see Figures 2.6 and 2.7, Adams et al., 2008; Rein & Papaloizou, 2009).

Although the trends outlined above are robust, the boundaries between the various regimes are not sharp, and are subject to a number of complications: First we note that the condition for passing through resonance, $\tau_a < \tau_R$, should be written in the more general form $\tau_a < A\tau_R$, where the factor A depends on the details of the system. For example, planetary systems with larger eccentricity are generically less stable, so the factor A will vary with orbital eccentricity (e.g., see Figure 2.12). Similarly,

systems with larger planetary masses are more interactive, so that the parameter A should increase with mass. Each type of resonance has a different libration timescale τ_R. In addition, the different resonances have different strengths, as determined by the depth of the effective potential well that the resonance angle resides within (and this effect can be incorporated into the factor A for a given resonance). The libration timescale is also affected by the other variables such as the migration timescale τ_a and/or the eccentricity damping timescale τ_e.

One of the challenges facing applications of these ideas to extrasolar planets is that many systems are expected to have comparable timescales so that $\tau_a \sim \tau_e \sim \tau_T$. All three of these timescales are often longer than the typical libration time τ_R, so that mean motion resonance is not usually compromised by fast migration alone. Instead, resonance configurations are compromised by a combination of too rapid migration, too much eccentricity excitation (not enough damping), and turbulent forcing acting over long spans of time. We also stress that these systems display sensitive dependence on their initial conditions (e.g., Figure 2.13), so that systems in essentially the same regime of parameter space can result in widely different outcomes. These differences are important, because migrating planets that maintain resonance stand a much greater chance of survival (see Figures 2.9 and 2.10).

Finally we note that planetary systems will continue to evolve after the removal of disk material from the system. When the gaseous disk is gone, the forcing terms that lead to migration, eccentricity damping, and turbulent forcing will vanish. However, the system will continue to evolve through gravitational forces. Planetary systems that are deep in mean motion resonance are expected to survive over long spans of time; on the other hand, systems that are near — but not in — resonance will often be disrupted over these longer time scales (e.g., Holman & Wiegert, 1999; David et al., 2003).

CHAPTER III

Accretion of Rocky Planets by Hot Jupiters

** The text appearing in this Chapter is an enhanced version of work originally published in Ketchum, Adams & Bloch, 2011b*

3.1 Abstract

The observed population of Hot Jupiters displays a stunning variety of physical properties, including a wide range of densities and core sizes for a given planetary mass. Motivated by the observational sample, this Letter studies the accretion of rocky planets byHot Jupiters, after the Jovian planets have finished their principal migration epoch and become parked in ~ 4 day orbits. In this scenario, rocky planets form later and then migrate inward due to torques from the remaining circumstellar disk, which also damps the orbital eccentricity. This mechanism thus represents one possible channel for increasing the core masses and metallicities of Hot Jupiters. This Letter determines probabilities for the possible end states for the rocky planet: collisions with the Jovian planets, accretion onto the star, ejection from the system, and long-term survival of both planets. These probabilities depend on the mass of the Jovian planet and its starting orbital eccentricity, as well as the eccentricity damping rate for the rocky planet. Since these systems are highly chaotic, a large ensemble ($N \sim 10^3$) of simulations with effectively equivalent starting conditions is required. Planetary collisions are common when the eccentricity damping rate is sufficiently low, but are rare otherwise. For systems that experience planetary collisions, this work determines the distributions of impact velocities – both speeds and impact parameters – for the collisions. These velocity distributions help determine the consequences of the impacts, e.g., where energy and heavy elements are deposited within the giant planets.

3.2 Introduction

With hundreds of alien worlds now detected, extrasolar planets have dramatically completed their migration into the main-stream of astronomy. The initial discoveries (Mayor & Queloz, 1995; Marcy & Butler, 1996) showed that the orbital elements of extrasolar planets are significantly different from those of Solar System planets. Some giant planets are found in short period orbits ($P_{orb} \approx 4$ days; semi-major axes $a \approx 0.05$ AU), while others have longer period orbits with a range of eccentricity, $0 \leqslant e \leqslant 0.9$. Subsequent discoveries indicate that such planetary systems are common and display a rich variety of architectures (Marcy & Butler, 2000; Hatzes et al., 2000; Perryman, 2000; Udry et al., 2007). The galactic planetary census is growing rapidly, and we can probe their physical properties, dynamics, composition, and even their weather.

An important subset of migrating Jovian planets reach the inner edge of their parental disks, where they enter orbits with periods $P_{orb} \sim 2 - 5$ days. Much of our knowledge regarding the physical properties of extrasolar planets comes from this population, primarily those planets observed in transit. For example, observations of transiting planets have driven an exploration of the planetary mass-radius relation, which shows several unexpected features. The mass distribution of these planets is wide, spanning more than three decades. The distribution of inferred densities is striking, with $\rho \approx 0.16 - 26$ g/cm^3, ranging over two orders of magnitude. Extrasolar planets thus span a wide range of radii for a given mass. The mass-radius relation for Hot Jupiters depends on many factors, including metallicity, core mass, stellar irradiation, and additional heat sources (Bodenheimer et al. 2003, hereafter BLL; Laughlin et al. 2011).

This Chapter explores one channel for Jovian planets to change their structure after reaching the vicinity of the star: Hot Jupiters can accrete additional rocky bodies while they are parked in close orbits. This accretion process increases the planetary mass, core mass, metallicity, and density of Jovian target. This scenario works as follows (see Figure 3.1): Jovian planets stop their inward migration at semi-major axes corresponding to ~ 4 day orbital periods. Although the reason for planets halting their migration is not completely understood, this orbital radius coincides (Lin et al., 1996) with the inner truncation point of the disk due to interactions with the stellar magnetosphere (Koenigl, 1991; Shu et al., 1994). As a result, Hot Jupiters can enter ~ 4 day orbits with circumstellar disk material remaining outside. Additional bodies (rocky Earth-like planets and/or larger Neptune-like planets) can subsequently migrate into the vicinity, where they tend to lock into mean motion resonance with

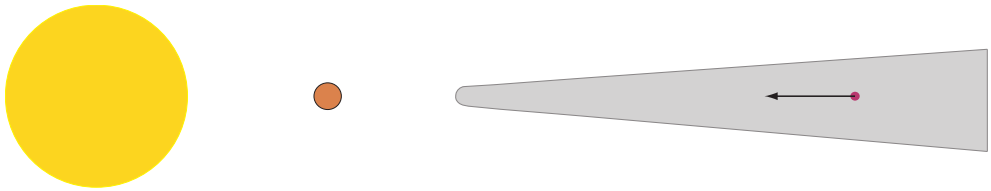

Figure 3.1: Diagram of the Hot Jupiter collision scenario outlined in the text.

the Hot Jupiter; as long as the disk acts on the rocky body, the two planets continue to migrate and interact.

The inward migration of these additional bodies, while the Hot Jupiter is stranded inside the inner disk edge, presents an interesting dynamical problem. Many outcomes are possible, including collisions between the planets, producing Earth-Jupiter systems in mean motion resonance, and accretion of planets onto the star. The relative frequency of these outcomes is studied here. If the resonant system survives, it would become a candidate for observing transit timing variations (Agol et al. 2005, hereafter ASSC). If rocky planets are accreted by the Hot Jupiter, its mass would increase. Since these rocky bodies have higher metallicities, and densities, than the original object, the planetary density generally increases. As a result, this mechanism alters the mass-radius relationship for Hot Jupiters and can help explain the diversity of planetary properties in the current sample. In particular, if the rocky bodies are large enough, they can survive the impact (Anic et al., 2007) and increase the core mass of the Jovian planet. The observed planet HD149026b is inferred to have an exceptionally large core mass $M_C \sim 80 M_\oplus$ (Ikoma et al., 2006; Fortney et al., 2006) and may provide one example of this mechanism in action.

Working within this scenario, this Chapter shows that a large fraction of inward migrating rocky planets collide with the Jovian planet, thereby allowing increases in core masses and metallicities. However, the collision rate decreases sharply for sufficiently high levels of eccentricity damping. If the Jovian planet has nonzero eccentricity, and/or smaller mass, the collision rate is lower for small damping rates, but persists for larger damping rates. For systems that experience planetary collisions, we determine the distributions of impact velocities.

This Chapter focuses on collisions between rocky bodies and Hot Jupiters. A complete understanding of the planetary mass-radius relation requires many additional mechanisms, e.g., Ohmic dissipation in planetary atmospheres (Batygin & Stevenson 2010, hereafter BS; Perna et al. 2010), which are beyond the scope of this work. Notice also that Hot Jupiters have a range of spin-orbit alignments, measured through

the Rossiter-McLaughlin effect (Fabrycky & Winn, 2009); some of these systems may have binary companions with inclined orbits so that planets are influenced by the Kozai effect (Wu et al., 2007). However, this Chapter is limited to systems where stellar binary companions do not play a defining role.

3.3 Formulation

This Chapter studies migration scenarios where the Hot Jupiter is already in place and a second body migrates inward. The most important parameters are the migration rate and eccentricity damping rate for the rocky planet, and the initial eccentricity and mass of the Jovian planet. Given that both the star and the the Hot Jupiter are much more massive than the rocky planet, the latter acts as a test particle (to leading order). If the rocky planet migrates sufficiently slowly, it is expected to become locked into mean motion resonance with the Hot Jupiter. Continued migration of the second body can then push both planets inward, although this motion ceases if the second body reaches the inner edge of the disk. In this case, the resulting pair of planets could survive in or near resonance. If the Hot Jupiter can be observed in transit, the second body can produce transit timing variations (ASSC). If the migration rate is too fast, the second planet passes through mean motion resonance (Quillen, 2006; Ketchum et al., 2011b) and will often experience a close encounter with the Hot Jupiter. The interaction event can result in either a collision between the two planets (and assimilation of the rocky body) or the accretion of one planet (generally the smaller one) by the central star. Planets are rarely scattered out of the solar system because the gravitational potential of the star (for a $\sim$ 4-day orbit) is deeper than that at the surface of a Jovian planet (escape thus requires 3-body effects). One goal of this work is to determine the branching ratios for the various outcomes — survival, accretion, scattering into the star — as a function of (Jovian) planetary mass and orbital eccentricity.

We approach this problem by performing direct numerical integrations of migrating planetary systems, i.e., we integrate the full set of 18 phase space variables for the 3-body problem consisting of the star, Hot Jupiter, and a second migrating planet. These integrations are carried out using a B-S integration scheme. In addition to gravity, we include forcing terms that represent inward migration and eccentricity damping; these additional effects arise due to the forces exerted on the planet(s) by the circumstellar disk. However, we do not model the disk directly, but rather include forcing terms to model its behavior.

We consider simple disk models where the surface density and temperature distribution of the disks are power-laws in radius,

$$\Sigma(r) = \Sigma_1 \left(\frac{r_1}{r}\right)^p \qquad \text{and} \qquad T(r) = T_1 \left(\frac{r_1}{r}\right)^q, \tag{3.1}$$

where Σ_1 and T_1 are normalization constants. For the sake of definiteness, we take $r_1 = 1$ AU, so the coefficients Σ_1 and T_1 correspond to values at 1 AU. The index p generally lies in the range $p = 1-2$; the intermediate value $p = 3/2$ arises for the Minimum Mass Solar Nebula model (Weidenschilling, 1977). The normalization for the surface density has a range of values, with $\Sigma_1 \approx 1500 - 4500$ g/cm^2 (Weidenschilling, 1977; Kuchner, 2004). The power-law index of the temperature profile $q \approx 3/4$ for a viscous accretion disk (Pringle, 1981) and a flat reprocessing disk (Adams & Shu, 1986), whereas $q \approx 1/2$ for a flared reprocessing disk (Kenyon & Hartmann, 1987; Chiang & Goldreich, 1997). The latter value is often used to describe the early solar nebula (Weidenschilling, 1977).

The disk scale height $H = a_S/\Omega$, where a_S is the sound speed, which is determined by the disk temperature profile. For a power-law temperature distribution, we obtain the form

$$\frac{H}{r} = \left(\frac{H_1}{r_1}\right) \left(\frac{r}{r_1}\right)^{(1-q)/2}. \tag{3.2}$$

At $r_1 = 1$ AU, we typically expect the scale height $H \approx 0.1r$.

To account for planet migration, we assume that the semi-major axis of the outer planet decreases with time according to the ansatz

$$\dot{a}/a = -1/\tau_a, \tag{3.3}$$

where τ_a is the migration timescale, which varies with a. We assume that only the outer planet experiences torques from the circumstellar disk. Small planets, with masses less than about that of Saturn, cannot clear disk gaps and migrate inward quickly through the process of Type I migration (Ward, 1997a). Larger bodies clear gaps and migrate more slowly. Planets are expected to experience a range of migration rates, depending on planet masses and disk properties. Estimates of the migration timescale for $a \sim 1$ AU typically fall in the range $10^4 - 10^5$ yr (Goldreich & Tremaine, 1980; Papaloizou & Larwood, 2000). The migration timescale decreases with semi-major axis a and can be further modified by subkeplerian rotation (Adams et al., 2009). Since we must perform a large ensemble of simulations using effectively equivalent starting conditions, we adopt a relatively simple model of Type I migration

(see below).

The strength of Type I torques can be written in the form

$$T_I = f_1 \left(\frac{m_P}{M_*} \right)^2 \pi \Sigma r^2 (r\Omega)^2 \left(\frac{r}{H} \right)^2, \tag{3.4}$$

where m_P is the mass of the rocky planet and f_1 is a dimensionless parameter (Ward, 1997a; Tanaka et al., 2002). For nearly Keplerian disks, the orbital angular momentum for a circular orbit is given by $J = m_P (G M_* r)^{1/2}$, and the migration timescale τ_a becomes

$$\tau_a = \frac{J}{T_I} = \frac{1}{f_1} \left(\frac{M_*}{m_P} \right) \left(\frac{M_*}{\pi \Sigma r^2} \right) \left(\frac{H}{r} \right)^2 \frac{1}{\Omega}. \tag{3.5}$$

Using typical parameter values, we obtain the scaled result

$$\tau_a = 5.6 \times 10^4 \text{ yr } \left(\frac{r}{r_1} \right)^{p-q+1/2} \left(\frac{m_P}{10 M_\oplus} \right)^{-1}. \tag{3.6}$$

We adopt the indices used to model the early solar nebula, $p = 3/2$ and $q = 1/2$, so the migration timescale is proportional to the orbital period,

$$\tau_a \approx 56,000 \, P_{orb} \, (m_P / 10 M_\oplus)^{-1}, \tag{3.7}$$

where the period is in years. The timescale τ_a thus decreases as the rocky planet moves inward, i.e., migration accelerates.

In addition to inward migration, circumstellar disks act to damp orbital eccentricity e of the migrating planet. This damping effect is found in almost all numerical simulations of the process (e.g., Kley et al., 2004), and can be parameterized through the ansatz

$$\dot{e}/e = -1/\tau_e = K(\dot{a}/a) \qquad \text{so that} \qquad \tau_e = \tau_a / K, \tag{3.8}$$

where τ_e is the eccentricity damping timescale. For planets that are large enough to clear gaps, analytic calculations suggest that eccentricity can be excited through the action of disk torques (Goldreich & Sari, 2003b; Ogilvie & Lubow, 2003), although multiple planet systems would be compromised if this were always the case (Moorhead & Adams, 2005). For smaller planets that remain embedded only eccentricity damping is expected. Given the uncertainties, we parameterize the eccentricity damping using equation (3.8) and explore a wide range of the damping parameter K such that $10^{-2} \leqslant K \leqslant 10^2$, where fully embedded planets are expected to have K values at the high end of this range (Artymowicz, 1993).

Note that this treatment implicitly assumes that the migrating planets are small enough so that they produce no back reaction on the disk. Since we are primarily interested in planetary cores in the mass range $m_P = 1 - 30 M_\oplus$, this assumption is expected to be valid.

3.4 Results

Using the formulation outlined above, we study the inward migration of rocky planets in planetary systems that contain a Hot Jupiter. The primary objective is to catalog the probabilities of the various outcomes, including survival, collisions, and accretion onto the star. A secondary goal is to determine the distribution of impact velocities for those cases that end in planetary collisions.

The parameter space for this study is large. For the sake of definiteness, the star has mass $M_* = 1.0 M_\odot$ and the Jovian planet has starting semi-major axis $a = 0.05$ AU ($P_{orb} \approx 4$ day). The eccentricity of the giant planet varies over the range $0 \leqslant e \leqslant 0.3$ (these planets are expected to become tidally circularized, but only on much longer timescales). The rocky planet starts just outside the 5:1 mean motion resonance ($a \approx 0.15$ AU), with small eccentricity $e = 0.001$, and fixed mass $m_P = 10 M_\oplus$; in this problem, the rocky planet acts like a test particle, so its mass cannot greatly affect the dynamics. The migration rate of the rocky planet varies with location, according to equation (3.7); inside the disk edge ($a \lesssim 0.05$AU), migration ceases. With these specifications, we consider the effects of varying the mass and eccentricity of the Jovian planet, and the eccentricity damping rate (through K) of the rocky planet. Since these systems are highly chaotic, a large ensemble of numerical experiments must be performed for each point in parameter space ($\sim$1000 independent realizations).

The main result from these simulations is the fraction of the trials that end with the two planets colliding. For a given migration rate, collisions represent the most common outcome provided that eccentricity damping is not too effective. These results are depicted in Figures 3.2 and 3.3, which show the fraction of collisions plotted versus the parameter K that sets the strength of eccentricity damping for the rocky planet (equation [3.8]). Figure 3.2 shows collision fractions for four choices of starting eccentricity for the Hot Jupiter, from $e = 0$ to $e = 0.3$. Figure 3.3 shows collision fractions for fixed starting eccentricity $e = 0.2$ and three choices for the Hot Jupiter mass, $M_P/M_J = 0.5$, 1, and 2. In both Figures, each point shown corresponds to the fractions calculated from $N \sim 300 - 1000$ independent realizations of the starting

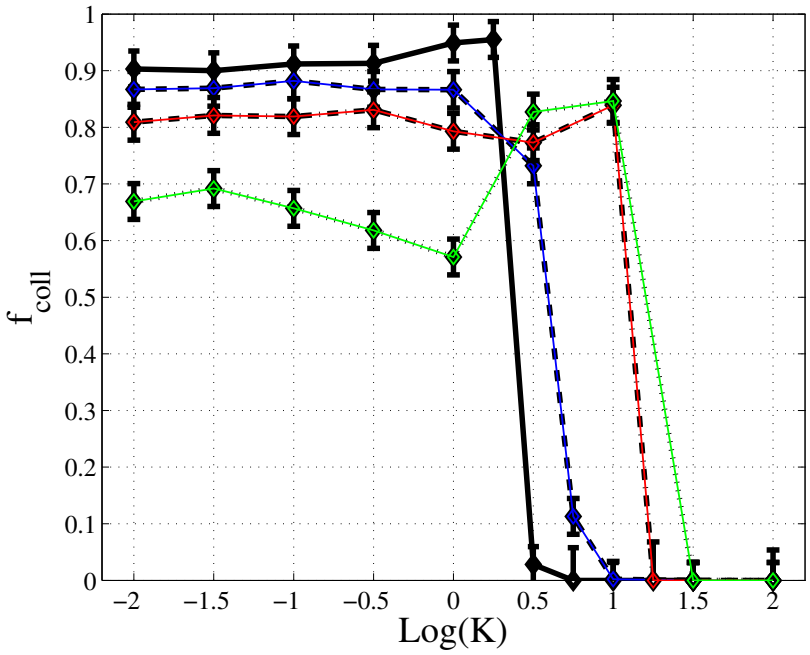

Figure 3.2: Collision fraction for rocky planets impacting Hot Jupiters versus eccentricity damping parameter K. The curves correspond to varying initial eccentricity of the Jovian orbit: $e = 0$ (black-solid), $e = 0.1$ (blue-dashes), $e = 0.2$ (red-dot-dashes), and $e = 0.3$ (green-dots).

conditions. The error bars ($\sim 1/\sqrt{N}$) provide a crude measure of the uncertainties.

The collection of results shown in Figures 3.2 and 3.3 shows a robust trend: For sufficiently weak eccentricity damping, namely $K < K_C \approx 10$, most simulations end with collisions between the planets. For stronger eccentricity damping, $K > K_C$, the fraction of collisions becomes negligible and nearly all of the systems survive (keeping both planets) over the entire range of integration times. Further, the critical level of eccentricity damping (K_C) depends on the starting eccentricity of the Hot Jupiter and its mass.

Larger eccentricities (for the Jovian orbit) allow collisions to occur in the face of greater eccentricity damping, following a trend of the approximate form $\log_{10} K_C \approx (3+10e)/4$ (from fitting). However, larger eccentricities combined with smaller values of K lead to lower collision rates. In this regime, collision events are replaced (primarily) by accretion events (onto the star). The larger eccentricity of the Jovian planet provides the rocky planet with greater opportunity to pass by and enter the gravitational realm of the star. Similarly, larger masses for the Jovian planet allow collisions to occur for larger values of the eccentricity damping parameter. In addition, larger

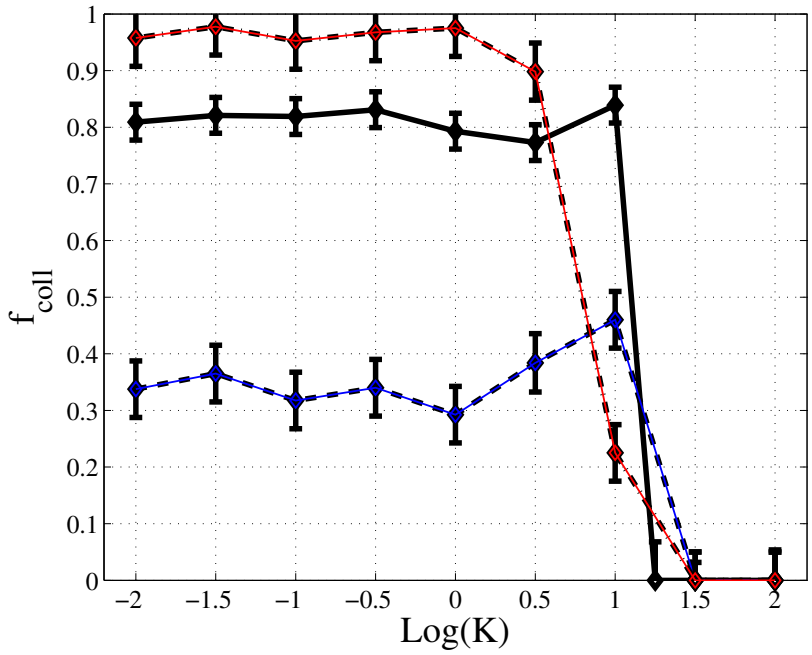

Figure 3.3: Collision fraction for rocky planets impacting Hot Jupiters versus eccentricity damping parameter K. The curves correspond to varying masses of the Jovian planet: $0.5M_J$ (red-dot-dashes-top), $1M_J$ (black-solid-middle), and $2M_J$ (blue-dashes-bottom).

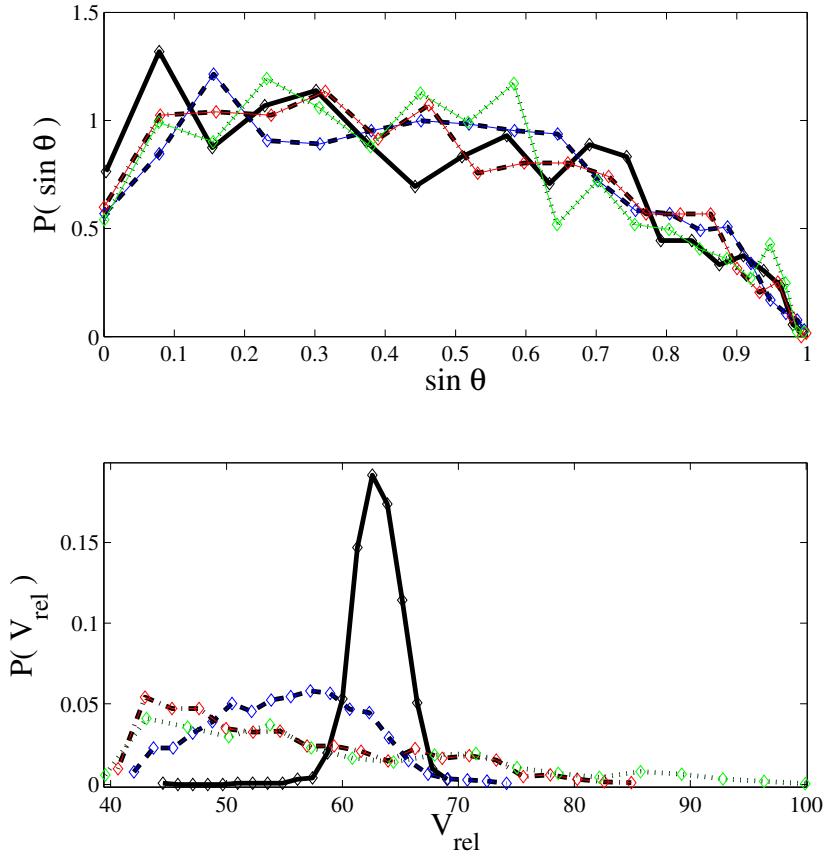

Figure 3.4: Distribution of impact velocities (for $K = 1$). Top panel shows distributions of impact directions, specified by $\sin\theta$, where the angle θ is given by $\cos\theta = \hat{v} \cdot \hat{r}$. Bottom panel shows distributions of impact speeds. In both panels, distributions are shown for systems where the Jovian planet has initial eccentricity $e = 0$ (black-solid), $e = 0.1$ (blue-dashes), $e = 0.2$ (red-dot-dashes), and $e = 0.3$ (green-dots).

masses combined with smaller values of K lead to lower collision rates. In this case, the collision events are (again) replaced with accretion events. The larger mass of the Jovian planet can scatter the rocky planet before impact, and the scattering alters the orbit of the rocky planet enough to send it into the star (or, more rarely, eject the planet).

For simulations that end in planetary collisions, the effect on the Jovian planet depends on the impact velocity of the rocky planet. Distributions of these impact velocities are depicted in Figure 3.4 (for eccentricity damping parameter $K = 1$). The top panel shows distributions of the angle at which the incoming planet strikes the giant planet surface. This distribution is equivalent to the distribution of impact parameter $\varpi = R_P \sin\theta$. Collision dynamics depend on the impact speed v_{rel}, shown in the bottom panel of Figure 3.4, and the escape speed $v_{esc} = (GM_P/R_P)^{1/2} \approx 37$ km/s (for $M_P = 1M_J$ and $R_P = 1.4R_J$). In the limit $v_{rel} \gg v_{esc}$, the giant planet presents a circular target and the probability $P(\varpi) \propto P(\sin\theta)$ increases with impact parameter ϖ. In the limit $v_{rel} \ll v_{esc}$, gravity of the planet focuses incoming trajectories into nearly radial paths and the distribution peaks near $\varpi = 0$. The calculated distribution is relatively flat, but falls with ϖ, which suggests significant gravitational focusing. This expectation is validated in the bottom panel of Figure 3.4, which shows that the impact speeds fall in the range $\sim 40 - 100$ km/s, so that $v/v_{esc} \sim 1 - 3$. When the Jovian planet has nonzero eccentricity, the distribution of speeds shows a broad peak near $v = 50$ km/s. For systems with $e = 0$, however, the distribution has a narrower peak near $v = 65$ km/s. One reason for this difference is that the rocky planets migrate further inward (before colliding) in the $e = 0$ simulations, so they are deeper in the gravitational potential well of the star. Obtaining a deeper dynamical understanding of this trend provides an interesting problem for future investigation. However, the following heuristic explanation serves to outline why there are different velocity distributions for the different cases.

In this scenario, the Super Earth (SE) is not massive enough to appreciably affect the angular momentum of the Hot Jupiter's (HJ) orbit, so the HJ's eccentricity stays close to its initial value. As the outer SE migrates into resonance zones with the HJ, the gravitational perturbations it receives from the HJ are big, which causes the SE's periapse (closest approach to the star) to circulate relative to the periapse for the HJ, i.e. it changes the phase of the SE's radial coordinate. This phase can make a big difference in the relative velocities of the planets at orbital intersections ONLY IF the HJ's orbit is not circular. It's this phase that's responsible for the broad distributions for non-circular HJ orbits (see Figure 3.5).

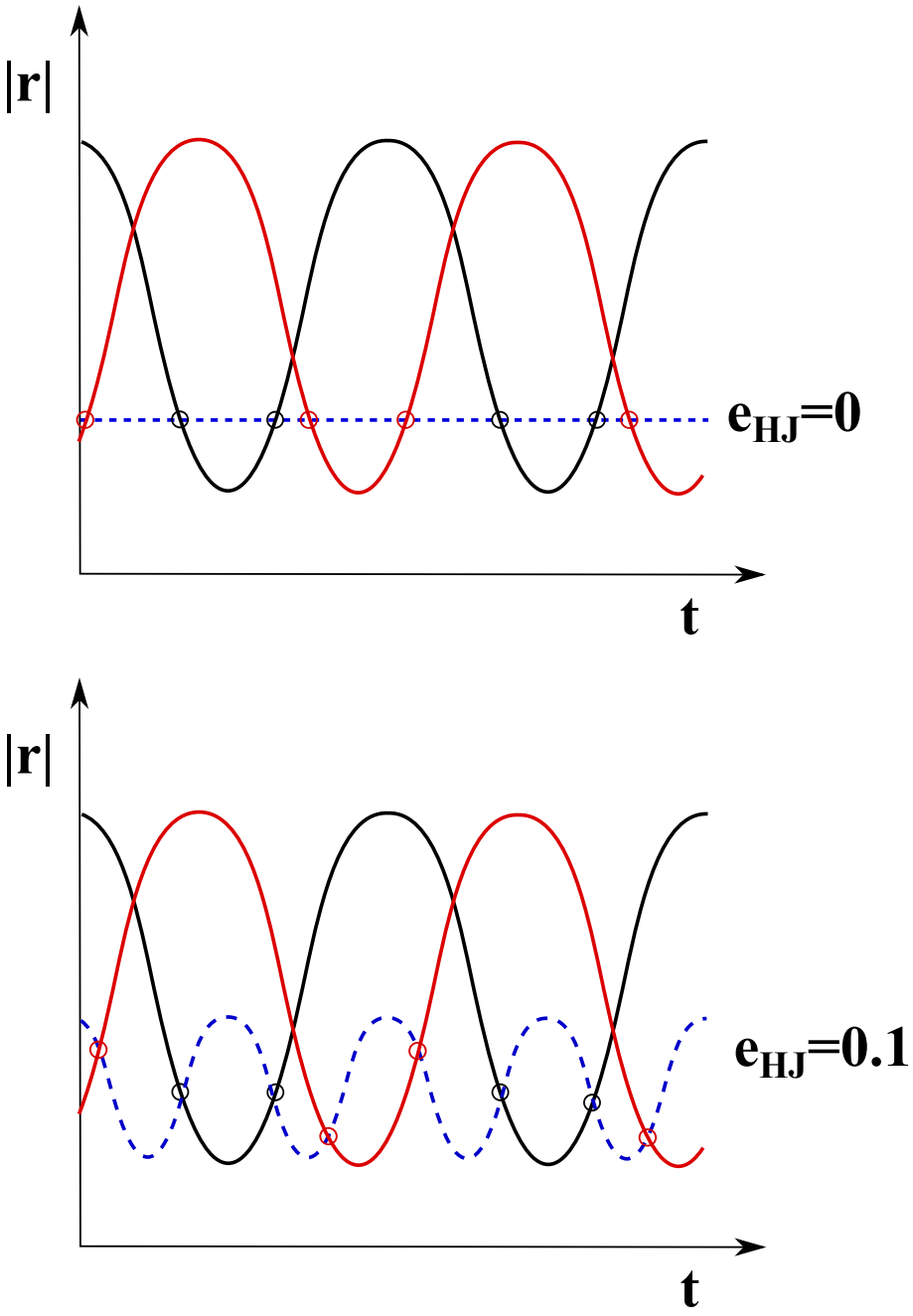

Figure 3.5: $\Delta\varpi$ dependence on collisional speed distributions. Radial distances (from the central star) as a function of time for the Hot Jupiter (dashed blue curve) and the Super Earth (black and red curves). *Top Panel*: Depicts the situation where the Hot Jupiter orbit is nearly circular. Notice that the periapse location of the SE doesn't affect the radial location of collisions. *Bottom Panel*: Depicts the situation where the HJ's orbit is non-circular. Notice that $\Delta\varpi$ between the two orbits can affect the radial location of collisions in this instance. These curves show in this figure are sine waves only as an approximation of how the curve should really look, and are used only for demonstrative purposes.

In the top panel of Figure 3.5, the HJ's orbit is circular, so the circulation of the SE's periapse (which changes the phase of the sine curve) has no effect on the radial location of collision (indicated by open circles), nor will it have any effect on the relative velocities of the planets at the moment of impact (the slopes of the curves at the points of all intersections on the figure are uniform). In this case, a sharp peak in Figure 3.4 (black curve) is expected. The value of the peak is likely a function of the SE's eccentricity and semi-major axis at the moment of collision (consider a small distribution of amplitudes and periods for the black and red sine curves), and the overall depth within the stellar potential at the moment of impact.

On the other hand, the bottom panel of Figure 3.5 shows the same scenario, except with the HJ's orbital eccentricity e=0.1 (or any other non-zero value). The HJ's radial coordinate in time now looks like a sinusoid too, except this one has a shorter period than the SE because it is closer to the star. Now, the radial locations of orbital intersections does depend on the relative alignment (or non-alignment) of the two orbits' periapse locations. The black open circles and the red open circles occur at different locations along the curves, so the relative velocities of the planets will be different in the two cases. This leads to the broader distributions of the curves in Figure 3.4 for non-circular Hot Jupiter orbits.

3.5 Conclusion

This Chapter explores the accretion of rocky planetary bodies by Hot Jupiters after they reach close-in orbits. The results show that collisions between planets are common when the eccentricity damping rate is sufficiently small, and rare otherwise. In approximate terms, collisions require the eccentricity damping parameter $K \leqslant K_C \approx 10$, where the threshold K_C depends on the eccentricity and mass of the Jovian planet (Figures 3.2, 3.3). The corresponding distributions of impact velocities for the collisions are shown in Figure 3.4.

These results have important implications for the diversity seen in the observational sample of Hot Jupiters: For large K values, both planets usually survive, in resonance, and such systems can exhibit observable transit timing variations (ASSC). For small K values, collisions are common whenever disks produce rocky bodies after a Hot Jupiter has migrated to its inner orbit. These collisions, in turn, can increase the core mass and the metallicity of the Jovian planet. Accretion onto the star and ejection are always rare.

The frequency of collisions is governed by the K value, which depends on disk

structure, viscosity, and the mass of the migrating rocky planet. Previous studies of planet-disk interactions generally find K values of order unity for migrating planets that clear gaps (Kley et al., 2004), but $K \approx 10 - 30$ for smaller embedded planets (Artymowicz, 1993). The outcomes thus depend on gap-clearing. For low-viscosity disks, planets clear gaps when their Hill sphere exceeds the disk scale height, $r_H > H$ (Crida et al., 2008; Papaloizou & Terquem, 2006), which requires $m_P \gtrsim 27 M_\oplus$ for the disk parameters used here. The gap doesn't need to be completely open to reduce the K value below the threhold K_C. Nonetheless, relatively large rocky planets ($m_P \gtrsim 10 - 20 M_\oplus$) are required for partial gap-clearing, reduced K values, and hence collisions. Small planets with $m_P \lesssim 10 M_\oplus$ are expected to have $K > K_C$ and hence to avoid collision with high probability. In addition, incoming rocky bodies must survive the collision and reach the core to increase its mass; survival is expected when $m_P \gtrsim 1 - 10 M_\oplus$ (Anic et al., 2007). Both the occurrence of collisions and subsequent survival to reach the core thus require $m_P \gtrsim 10 M_\oplus$. Although this threshold mass should be determined more rigorously, these results show that larger rocky planets have more influence (per unit mass) than smaller ones.

In addition to increasing the core mass, accretion of rocky planets can affect the energy budget of giant planets. Figure 3.4 shows the distribution of impact speeds for rocky planets that collide with Hot Jupiters. This distribution indicates speeds $v \sim 40 - 100$ km/s, so we consider a benchmark $v \sim 60$ km/s. With this speed, an accreting "superearth" planet with mass $m_P = 10 M_\oplus$ deposits energy

$$\Delta E = \frac{1}{2} m_P v^2 \approx 1.1 \times 10^{42} \text{ergs}. \tag{3.9}$$

To put this energy increment into perspective, note that the binding energy of the Hot Jupiter $U = f G M_P^2 / R_P \approx 1.6 \times 10^{43}$ erg (using typical values $M_P = 1 M_J$, $R_P = 1.4 M_J$, and $f = 3/5$). A single collision thus accounts for $\sim 7\%$ of the binding energy of a Hot Jupiter. If we assume the energy ΔE is deposited deep within the planet, and slowly leaks out over time $\Delta t \sim 1$ Gyr, the associated power increment $\Delta P \approx 3.5 \times 10^{18}$ W, large enough to help inflate the planetary radius (BLL, BS). On the other hand, if the energy is deposited in the upper atmosphere of the planet, it quickly radiates away and cannot inflate the radius.

The results of this Chapter pose a number of interesting problems for future work. To determine the number of accretion events (per Hot Jupiter) we need a better understanding of eccentricity damping rates for both migrating rocky planets and Hot Jupiters; we also need estimates for the number (and masses) of rocky

planets produced after Hot Jupiter migration has occurred. When accretion events take place, we need to understand the energy deposition within the giant planet and the subsequent long-term transfer of heat/energy out of the planetary body. These issues, and others, will help explain the observed diversity in the properties of Hot Jupiters.

CHAPTER IV

Mean Motion Resonance in Exoplanet Systems: Introduction to Nodding Behavior

** The text appearing in this Chapter is an enhanced version of work originally published in Ketchum, Adams & Bloch, 2013*

4.1 Abstract

Motivated by the large number of extrasolar planetary systems that are near mean motion resonances, this Chapter explores a related type of dynamical behavior known as "nodding". Here, the resonance angle of a planetary system executes libration (oscillatory motion) for several cycles, circulates for one or more cycles, and then enters once again into libration. This type of complicated dynamics can affect our interpretation of observed planetary systems that are in or near mean motion resonance. This work shows that planetary systems in (near) mean motion resonance can exhibit nodding behavior, and outlines the portion of parameter space where it occurs. This problem is addressed using both full numerical integrations of the planetary systems and via model equations obtained through expansions of the disturbing function. In the latter approach, we identify the relevant terms that allow for nodding. The two approaches are in agreement, and show that nodding often occurs when a small body is in an external mean motion resonance with a larger planet. As a result, the nodding phenomenon can be important for interpreting observations of transit timing variations, where the existence of smaller bodies is inferred through their effects on larger, observed transiting planets. For example, in actively nodding planetary systems, both the amplitude and frequency of the transit timing variations depend on the observational time window.

4.2 Introduction

The current observational sample of extrasolar planets includes many systems with multiple planets, and many systems have orbital period ratios that are close to integer values (e.g., Fabrycky et al. 2012). These systems are thus candidates for being in mean motion resonance (MMR), which represents a special dynamical state for a planetary system. In addition to the necessary period ratio, the other dynamical variables of a resonant system must allow one or more resonance angles (see below for their definitions) to execute oscillatory behavior (e.g., Murray & Dermott 1999; hereafter MD99). One way to describe this requirement is that the resonant angle(s) must reside in a "bound state" within an "effective potential well". Because of the special conditions required for a planetary system to reside in mean motion resonance, systems found in such states must have a constrained dynamical history. The relative fraction of planetary systems in mean motion resonance thus provides important information regarding planetary formation and early dynamical evolution.

The dynamics of mean motion resonances is often more complex than indicated by standard textbook treatments. This Chapter explores one such complication called "nodding", where the resonance angle librates for several cycles and then circulates for one or more cycles before returning to an oscillatory state. In addition to appearing in planetary systems, this nodding behavior arises in other dynamical systems, including the driven, inverted pendulum (Acheson, 1995). Additionally, nodding systems sometimes exhibit similar phase characteristics to other known dynamical systems, such as the the Duffing oscillator (Guckenheimer & Holmes, 1983). The immediate goal of this Chapter is to obtain a better understanding of nodding in the context of three-body planetary systems. The over-arching goal is to provide a more detailed basis for interpreting observed systems that are found in or near resonance, including systems that exhibit transit timing variations (TTV), which provide a means of detecting small bodies interacting with larger planets in transit (Agol et al., 2005).

Resonant and near-resonant systems provide important information about planetary systems. As one example, note that it is relatively easy to disrupt the resonance through external perturbations (Adams et al., 2008; Rein & Papaloizou, 2009; Ketchum et al., 2011b). As a result, planetary systems that are observed in resonance today must not have been greatly perturbed in the past, or they must have been subsequently influenced by significant dissipative interactions.

As another example, we note that entry into mean motion resonance is non-trivial: If the orbital elements of a planetary system are selected at random, the

chance that the system resides in a mean motion resonance is slim (even when the period ratio is chosen to be near the ratio of small integers). However, systems can evolve into resonance states through the process of convergent migration (e.g., Lee & Peale, 2002), where, for instance, the outer planet migrates inward faster than the inner planet, and the two bodies subsequently move inward together. Even in this scenario, survival of the resonance can be compromised by overly rapid migration (Quillen, 2006), and/or by turbulent forcing from the disk driving the migration (Lecoanet et al., 2009; Ketchum et al., 2011b).

As one potential application of this work, nodding can affect our interpretation of TTVs (Agol et al., 2005). In this setting, unseen small bodies orbit outside observed transiting planets (usually Hot Jupiters). The smaller bodies affect the orbit of the inner, larger planets and lead to small variations in the timing of the transit events. This phenomenon is potentially a powerful method to detect (infer the presence of) smaller, otherwise unobserved, planets in such systems. Indeed, discoveries of this type have already been reported (e.g., Holman et al., 2010; Cochran et al., 2011), and many more are expected in the near future. However, the timing variations are largest when the smaller planets are in or near mean motion resonance with the larger planet (e.g., Nesvorný & Morbidelli, 2008), and such systems are susceptible to nodding as studied herein. Even without the complication posed by nodding, inferring the system properties from observations is a sensitive process (e.g., Veras et al., 2011). In any case, the results of this work will be useful for future interpretation of systems that exhibit transit timing variations.

This Chapter is organized as follows. In Section 4.3, we study the nodding phenomena through numerical integrations of multiple planet systems that are near mean motion resonance. This investigation shows that complex dynamical behavior, including nodding, is often present, and outlines the portion of parameter space where it occurs. For systems that exhibit nodding behavior, we then outline the corresponding effects on transit timing variations. In Section 4.4, we derive a class of model equations to describe nodding behavior. Here we expand the disturbing function for planetary interactions (e.g., MD99), keep the highest order terms, and identify the relevant terms that lead to nodding. The resulting model equations elucidate the dynamical ingredients required for nodding behavior to take place. We conclude, in Section 4, with a summary of our results, a discussion of their implications, and a brief description of future work.

4.3 Numerical Study of Nodding

4.3.1 Full 3-body Numerical Simulations

This Chapter studies nodding of mean motion resonance angles for planet pairs that are near MMR. For simplicity, most of this work focuses on the 2:1 resonance. The term "nodding" here refers to a tendency to repeat a pattern of bounded libration for several cycles followed by one or more cycles of circulation. For intermediate times, the system exhibits behavior of MMR, but intermittent bouts of circulation may produce a cumulative net circulation of the resonance angle over many libration times. In the context of resonant angle phase trajectories, nodding can be described as motion near a separatrix in the phase space. The phase space for internal resonances contain one separatrix, whereas the phase space for external resonances can contain two distinct separatrices. The qualitative differences are mainly due to the existence of asymmetric external resonances, which arise when the orbital eccentricity for the test body becomes sufficiently large (Ferraz-Mello et al., 2003).

To carry out the study in this section, we numerically integrate the three body gravitational forces using a Bulirsch-Stoer integration scheme. In addition to gravity, both general relativistic corrections and stellar tidal damping are included in force calculations, but the inclusion of these additional forces were not necessary to produce the interesting features explored in this work. Our system consists of a star with mass $M_* = 1M_\odot$, a massive planet ($m_p = 1M_{Jup}$), and a test body ($m = 10^{-6}M_{Jup}$). We chose this particular test mass in order to minimize its influence on the planet's motion and to obtain the clearest dynamical signature of resonance angle nodding, but nodding is also present for larger test body masses. The planet is placed in orbit with period $T_p = 1$ year, and the test body is placed in orbit with initial period $T = 1/2$ or $T = 2$ years for studies involving internal and external resonances, respectively. We choose a benchmark test body eccentricity of $e = 0.15$, which is motivated by previous work (Ketchum et al., 2011b), and we choose from two values for the planet's initial orbital eccentricity, $e_p = 0.001$ or $e_p = 0.1$.

To fully describe the initial configuration of the system, the initial orbital angles must be specified. We parameterize this study using the set of angles given by $\Delta\varpi_0$ – the relative alignment between the two orbits – and f_0 – the test body's true anomaly. Unless noted otherwise, all simulations begin with the planet and test body in conjunction. In an attempt to sample the available resonance angle phase space resulting from a choice of initial orbital elements $\{e_p, e, \alpha, \Delta\varpi\}$, values of f_0 spanning the full range $-\pi$ to π in increments of $\pi/100$ are sampled. Following this systematic

approach, those states that have phase trajectories occurring near a separatrix, which ultimately lead to nodding, are easily found.

The simulations are integrated for 10^4 years, a sufficient amount of time to capture several secular cycles for most initial configurations (for completeness, note that the parameter space for external resonances contain small regions where the secular cycle's period is infinite – see Michtchenko et al. 2008b). The energy for a typical system that experiences no significant close encounters is conserved to better than one part in 10^{10}. The planets' period ratio is monitored to confirm that the system remains nearly integer commensurate during the integration and hence that near resonance has not been compromised by a chance close encounter. The osculating elements for both bodies are recorded once per orbit of the inner planet, frequently enough to account for short period effects. For 2:1 resonances, the resonance angles of interest are

$$\phi = 2\lambda_p - \lambda - \varpi \ , \tag{4.1}$$

for a test body internal to the planet's orbit, and

$$\phi = 2\lambda - \lambda_p - \varpi \ , \tag{4.2}$$

for a test body external to the planet's orbit, where λ is the mean longitude and subscript p denotes the orbital elements belonging to the Jovian planet. And finally, the time rate of change for the resonance angle, $\dot{\phi}$, is determined by quadratic interpolation, and used to construct resonance angle phase trajectories.

4.3.2 Nodding Features for Near-Resonance

The range of dynamical behaviors encountered in (or near) mean motion resonance is surprisingly rich (e.g., Michtchenko et al., 2008a,b). Presented here is a small representative sample set of the simulations outlined above which display the main features found in these resonance states.

We first consider systems where nodding does *not* occur (see Figure 4.1). The figure features a system with a configuration and behavior deviating only slightly from the pendulum model of MD99. For this system, the perturbing planet is placed in orbit with semi-major axis $a_p = 1$AU and eccentricity $e_p = 10^{-3}$ around a $1M_\odot$ star. A test particle of mass $m = 10^{-6}M_{Jup}$ is set in a coplanar orbit with semi-major axis $a = 0.63$ AU and orbital eccentricity $e = 0.15$, which places the two orbiting bodies near a 2:1 period ratio. The orbits are initially anti-aligned ($\Delta\varpi_0 = \pi$) and the orbiting bodies placed in conjunction with the test particle near periapse – the

system is prepared such that the planet's influence on the test body's motion is initially minimized, i.e., the two orbiting bodies cannot be separated further from one another during conjunction given this set of orbital elements. The top panel of Figure 4.1 shows the resonance angle, ϕ, from equation (4.1) in blue and the angle of apsides, $\Delta\varpi$, in red. The resonance angle librates with a small amplitude of $\Delta\phi \simeq 0.1$ radians around the equilibrium $\phi = 0$, while the apsidal angle circulates due to a prograde motion of the test particle's longitude of periastron – the planet's longitude of periastron, ϖ_p, does not move significantly. In the limit of small orbital eccentricities e and e_p, the test body's true anomaly approximately coincides with the resonance angle at instances of conjunction. Thus, for this system, these dynamics depend mainly upon our choice for $|f_0|$ and are independent of our choice for $\Delta\varpi$. The bottom panel of Figure 4.1 shows the phase trajectory for the resonance angle. This panel depicts a phase trajectory analogous to small oscillations of a simple pendulum, as expected. In this respect, the pendulum model of the circular restricted three body problem provides a sufficient model for resonances arising from orbital configurations of this type – although the planet's orbital eccentricity is non-zero, dynamical deviations from the pendulum model of the circular restricted three body problem incurred through small departures from circular symmetry are negligible.

As $|f_0|$ increases from 0 to π, the amplitude of oscillations also increase until the conjunction line approaches apoapse, where the system reaches a separatrix and the resonance angle will circulate rather than oscillate. Figure 4.2 shows a system identical to that of Figure 4.1 in all aspects except that $f_0 \approx 2\pi/3$ radians, so that the resonance angle exhibits larger oscillations. The libration frequencies of the two systems however, are practically identical with frequency $\omega \sim 0.03$ yr^{-1}.

For external resonance scenarios, the behavior is significantly different. Figure 4.3 shows the first example of nodding. In the figure, $|f_0| \sim \pi$ so initial conjunction is close to apastron of the test body's orbit, and the orbits are initially anti-aligned, $\Delta\varpi_0 = \pi$. This set of initial orbital elements gives the maximum possible spatial separation between the planet and test body. The resonance angle ϕ, given by equation (4.2) and shown in blue in the top panel of the figure, seems to be attracted to one of two stable fixed points, with an unstable fixed point effectively located at $\phi = \pi$. This is an example of an asymmetric resonance (Callegari et al., 2004; Lee, 2004), and the existence of the two equilibrium points on either side of $\phi = \pi$ are due to a bifurcation occurring in the dynamics for sufficiently large test body orbital eccentricity (e.g., Michtchenko et al., 2008b). As it turns out, this system was configured near a different kind of separatrix than those encountered for internal resonances, and

motion near this separatrix leads to nodding behavior that is unique to the external case. There are several secular cycles shown in the figure, and during each secular cycle the resonance angle seems to choose one of three different libration modes – *(a)* resonance oscillations enclosing some point to the left of $\phi = \pi$, *(b)* oscillations enclosing some point to the right of $\phi = \pi$, or *(c)* oscillations enclosing all three points. As $|f_0| \to 0$ for similarly prepared systems, resonant oscillation amplitudes reach the maximum possible value $\Delta\phi \approx \pi$ radians before circulating. Encountered here is another separatrix, which is analogous to the separatrix for the internal resonance. In contrast to the internal resonance separatrix, the phase space trajectory for large amplitude oscillations here takes a different shape – the resonant angle's speed decreases (increases) as it approaches (departs from) the test body's apoapse location. Systems on such phase trajectories appear to nod once per one resonant libration, as depicted in Figure 4.4 where $f_0 \approx \pi/4$. In this regard, the resonance angle moves as if it lives in a quartic potential, with a local maximum at $\phi = \pi$, two minima near $\phi = \pi/2$ and $\phi = 3\pi/2$, and a maximum at $\phi = 0$. This feature of the motion near the outer separatrix of an asymmetric outer resonance can lead to a period increase or decrease by a factor of two for transit timing variations, a result presented later on in this Chapter.

The nodding features become more prevalent as the perturber's eccentricity increases, where the resonance angle can begin accumulating a net circulation over longer times. Figures 4.5 and 4.6 provide examples of the type of circulation behavior we observe in simulations. These two figures also showcase the stark contrasts between nodding for internal and external resonances, respectively. In this comparison, the planet's orbital eccentricity is $e_p = 0.1$ – substantial enough to be well outside the *circular* restricted three body regime (where the pendulum model is strictly valid). Both examples show the tendency for $\Delta\varpi$ to circulate, on average, with a periodic component resulting from secular interactions, and, on average, the resonance angle circulates at the same rate. For times shorter than secular timescales, however, the resonance angle librates with some amplitude, not exceeding $\Delta\phi = \pi$, around some equilibrium point. The point about which the resonance angle oscillates differs between the external and internal perturber cases. For the pendulum model of the circular restricted 3-body problem, the equilibrium point is located at $\phi = 0$ for internal resonances, while for external resonances it is $\phi = \pi$. We stress, however, that the pendulum model is an over-simplification for the regime under consideration.

Figure 4.5 shows the eccentricities (top panel), resonance angle (middle panel), and phase trajectory (bottom panel) for a system the same set of initial orbital elements

as was used in Figure 4.1, with the exception that here the planet's orbital eccentricity $e_p = 0.1$. The system is prepared with anti-aligned orbits and the orbiting bodies in conjunction near the test body's apoapse. Recall from the above discussion that this particular configuration places the resonance angle near a separatrix in its phase space. The figure shows slightly more than 3 complete secular cycles, each lasting ≈ 3300 yrs, which corresponds to hundreds of libration times. During each secular cycle, the test body's orbital eccentricity (shown in black in the top panel) increases from its initial value of $e = 0.15$ up to $e \sim 0.6$ (where the two orbits intersect for a time), and then decreases close to its initial value. For times that are shorter than secular timescales and longer than libration timescales, the resonance angle undergoes large amplitude oscillation about the test body's periapse. In the previous case, when the planet's orbit was nearly circular, the motion of the test body's apsidal angle was steady circulation. In the present case where the Jovian planet's eccentricity is substantially larger, the azimuthal symmetry of the star-planet Keplarian system has been sufficiently broken and the evolution of the test body's osculating elements depends sensitively upon the orbital alignment (given by the apsidal angle, $\Delta\varpi$). The red curve in the middle panel of Figure 4.5 shows the apsidal angle, which, over the course of one secular cycle, oscillates once very slowly about $\Delta\varpi = \pi$, then very abruptly passes $\Delta\varpi = 0$ in the retrograde direction. Generally, as the apsidal angle approaches $\Delta\varpi = \pi$ (i.e., as the orbits approach anti-alignment), the test body's eccentricity decreases, and as the orbits rotate out of anti-alignment, the eccentricity increases. As the apsidal angle approaches $\Delta\varpi = 0$, the orbits come into alignment, and with comparatively large orbital eccentricities, the planet exerts greater influence on the motion of the test body than in cases where it's orbit is nearly circular (see Batygin & Morbidelli 2011 for a detailed analysis of secular dynamics). As a consequence, the resonance angle circulates once or twice until the orbits rotate out of alignment, and the system enters into yet another secular cycle that deviates only slightly from the one just described. The test body can exhibit a wide range of eccentricity growth/decay during a secular cycle, and the duration of the secular cycle depends on the details of the initial 3-body configuration. However, the generic behavior of the osculating orbital elements described above during a secular cycle for any choice of $\Delta\varpi_0$ is robust. As long as the orbiting bodies are in conjunction with f_0 for the test body near apoapse, the resonance will reside near the separatrix in phase space and the system can experience nodding for states near mean motion resonance.

For the external resonance shown in Figure 4.6, the system is initially configured with anti-aligned orbits $\Delta\varpi = \pi$ and conjunction occurring near the test body's

apastron $f_0 \simeq \pi$. The test body's orbital eccentricity is sufficiently large to place the system near an asymmetric resonance, meaning there are generally two libration points. The exact locations of the libration points depend on the instantaneous orbital eccentricity (shown by the black curve in the top panel of the figure), but for ease of discussion, we take them to be $\approx \pi \pm \pi/2$. During a secular cycle, the resonance angle ϕ oscillates with an amplitude $\pi/4 \lesssim \Delta\phi < \pi/2$. There are 6 full secular cycles shown here, each lasting ~ 1600 years. The test body's periapse circulates in the retrograde direction on average, so the apsidal angle $\Delta\varpi$ circulates. The nodding cycle, eccentricity growth/decay, and the apsidal angle circulation are all governed by the secular cycle and coordinate together to produce the specific nodding behavior of the resonance angle. As the two orbits' major axes rotate to become more perpendicular, the test body's eccentricity grows, and resonant oscillation amplitudes decrease, resulting in a tightening of libration. As the two orbits rotate so that their major axes become parallel (orbits either aligned or anti-aligned), the test body's orbital eccentricity decreases. The eccentricity attains a minimum value when the major axes are in alignment, reaching its smallest values when the orbits' periapses become aligned (as opposed to anti-aligned). As the test body's orbital eccentricity decreases, the libration points of the asymmetric resonance move closer to π and the resonant angle's oscillation amplitudes generally increase, which in turn moves the phase trajectory toward one of the two separatrices. With the orbits near alignment ($\Delta\varpi \approx 0$), the phase trajectory approaches the outer separatrix, and circulation becomes possible. When the orbits are nearly anti-aligned, the phase trajectory approaches the inner separatrix, which separates bounded libration around a single stable point from libration around both. Here, it is possible for the phase trajectory to jump across π to the adjacent stable point. The number of times the resonant angle circulates or jumps back and forth between stable points during major axes alignment varies from secular cycle to cycle. However, the nodding cycles tend to mimic preceding cycles, and every so often abrupt changes will occur which again persist over multiple nodding cycles, until another abrupt change occurs. This behavior then repeats.

To summarize, we have studied both internal and external resonance scenarios using both nearly circular planet orbits ($e_p = 10^{-3}$) and an orbit that departs from circular ($e_p = 0.1$). We took a benchmark value for the test body's initial orbital eccentricity of $e = 0.15$, but this value varied with the secular cycle, reaching values as high as $e \simeq 0.6$ and as low as $e \simeq 0.01$. Variations to the test body's orbital eccentricity increased in simulations which included larger planet eccentricity. On secular timescales, the 2:1 resonance angle may exhibit bouts of circulation with

regular libration in between circulation events (the phenomenon we call nodding). Nodding is common when the planet's orbital eccentricity is sufficiently large, where we find an approximate threshold of $\sim e_p \gtrsim$ a few $\times 10^{-2}$. Nodding systems with larger orbital eccentricities are able to obtain greater net circulation than systems where both orbital eccentricities are small. However, the relative orbital alignment and the test body's true anomaly at the moment of conjunction affect both the period of the nodding cycle and the libration width during intermediate times. Both internal and external resonances exhibit nodding, but prominent qualitative differences in the nodding signatures between the two configurations exist. Because of our choice of initial test body orbital eccentricity, asymmetric resonances are found for external cases, where libration occurs around points $\phi = (1 \pm \delta/2)\pi$ with $\delta \approx 1$ for $e_0 \approx 0.15$ (e.g., Callegari et al., 2004; Lee, 2004). Consequently, for external resonances, libration amplitudes are typically smaller ($\Delta\phi \lesssim \pi/4$) for large e_p. For nearly circular planet orbits, large amplitudes ($\Delta\phi \lesssim \pi$) may persist for external resonances, and appear to librate about $\phi = \pi$. However, the resonance angle's motion slows as it passes $\phi = \pi$, which is distinctively different from large amplitude oscillations for the internal resonance case.

4.3.3 Dynamical Map of Nodding in the Hot Jupiter Problem

In this section we explore the nodding phenomenon for Hot Jupiters. Because of the existence of the asymmetric resonance and the additional separatrix that comes along with it, the external resonance is particularly interesting in the context of the Hot Jupiter problem (where smaller bodies could be found in outer orbits – see Ketchum et al. 2011a). For completeness, we explore how the resonance angles of the external 2:1 near resonance are affected by the external test body's orbital eccentricity and by the orbital alignment between the planet and the test body. To perform this study, we use typical parameters of Hot Jupiter systems, where a Jovian planet (with mass $m_p = 1 M_{Jup}$, orbital eccentricity $e_p = 0.04$, and orbital period $T_p = 4$ days) orbits a $1 M_\odot$ star with a small planet (with mass $m = 1 M_\oplus$ and orbital period $T = 8$ days) orbiting external to the Star-Jovian system. We take orbital eccentricity values for the test body between $-3 \leqslant \log_{10} e \leqslant -1/3$ in equally spaced logarithmic increments. For each value of the test body's eccentricity, we perform an ensemble of 200 similarly prepared systems, each with a slightly different initial apsidal angle between $-\pi < \Delta\varpi \leqslant \pi$ in equally spaced increments. Both the Hot Jupiter and the smaller rocky planet begin each simulation located at the periastron of their respective orbits (not necessarily in conjunction with one another). The

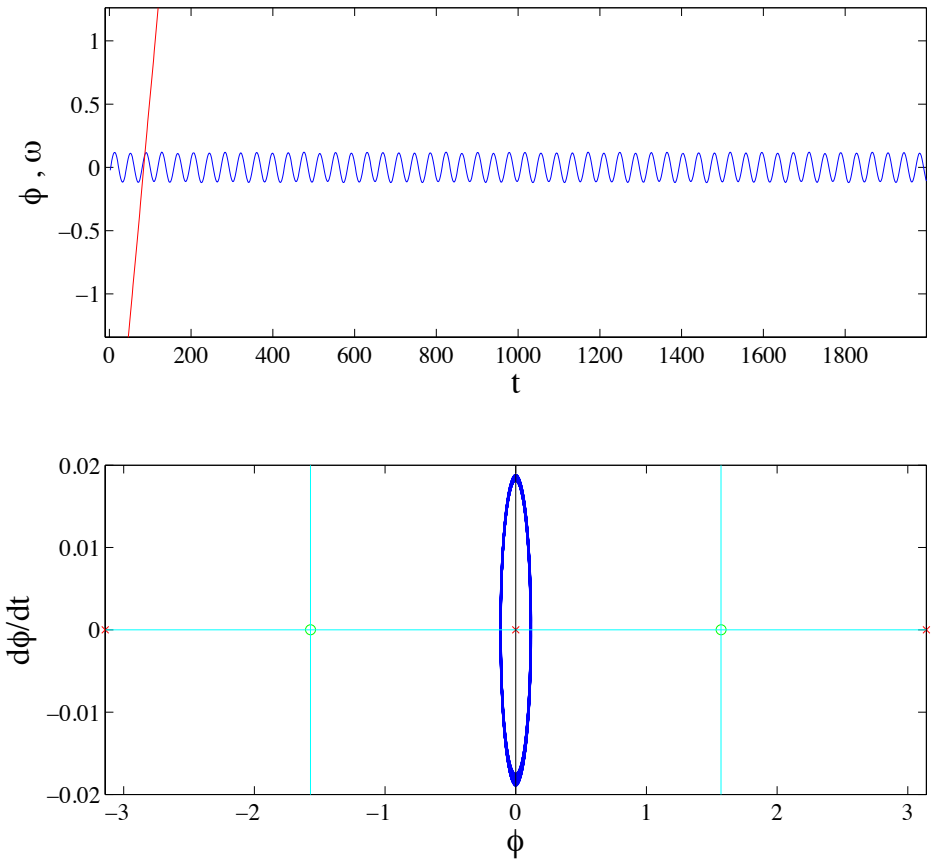

Figure 4.1: Internal 2:1 near-MMR with small amplitude of librations. Internal 2:1 near-resonance with periaspses initially anti-aligned ($\Delta\varpi = 0$), test body near periastron at conjunction ($f_0 \approx 0$), and $e_p = 10^{-3}$. The *top panel* shows the resonance angle, ϕ (blue curve), and the angle of apsides, $\Delta\varpi$ (red curve). In this example, resonance angle nodding does *not* occur. The *bottom panel* shows the phase trajectory of the resonance angle during the full 10^4 years of simulation. This system is close to the text book example of mean motion resonance described by the pendulum model (see Murray & Dermott 1999). The libration amplitude is small ($\Delta\phi \sim 0.1$ rad) and the equilibrium point for oscillations is at $\phi = 0$.

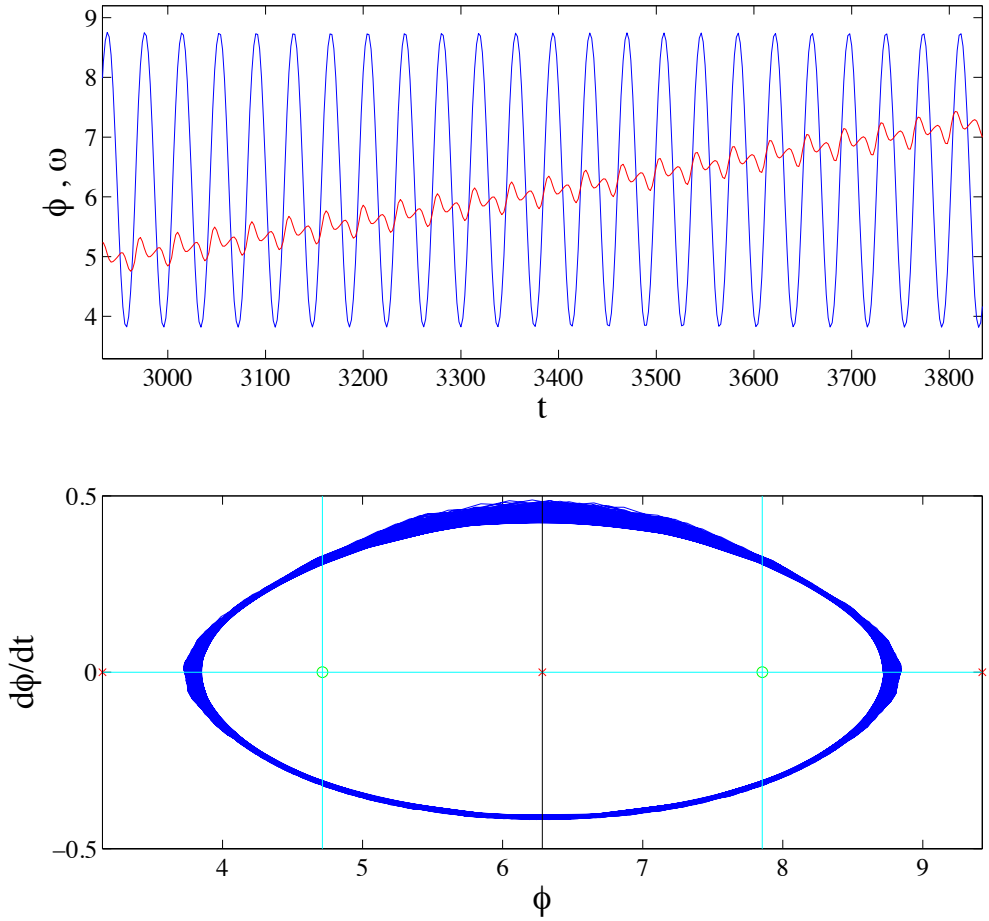

Figure 4.2: Internal 2:1 near-MMR with large amplitude of librations. Internal 2:1 near-resonance with periapses initially anti-aligned ($\Delta\varpi = 0$), test body closer to apastron than to periastron during initial conjunction with a true anomaly $f_0 \approx 2\pi/3$, and the perturbing planet's orbit nearly circular with an eccentricity of $e_p = 10^{-3}$. The *top panel* depicts the resonance angle (blue curve) and the angle of apsides (red curve). The resonance angle undergoes large amplitude oscillations of $\Delta\phi \geqslant 3\pi/4$ due to the test body's large angular displacement from periastron of its orbit during the initial conjunction with the perturbing planet. In this example, resonance angle nodding does *not* occur. The *bottom panel* shows the phase trajectory for the resonance angle over the full 10^4 years of the simulation, which oscillates about 0 (modulo 2π) and doesn't circulate at anytime.

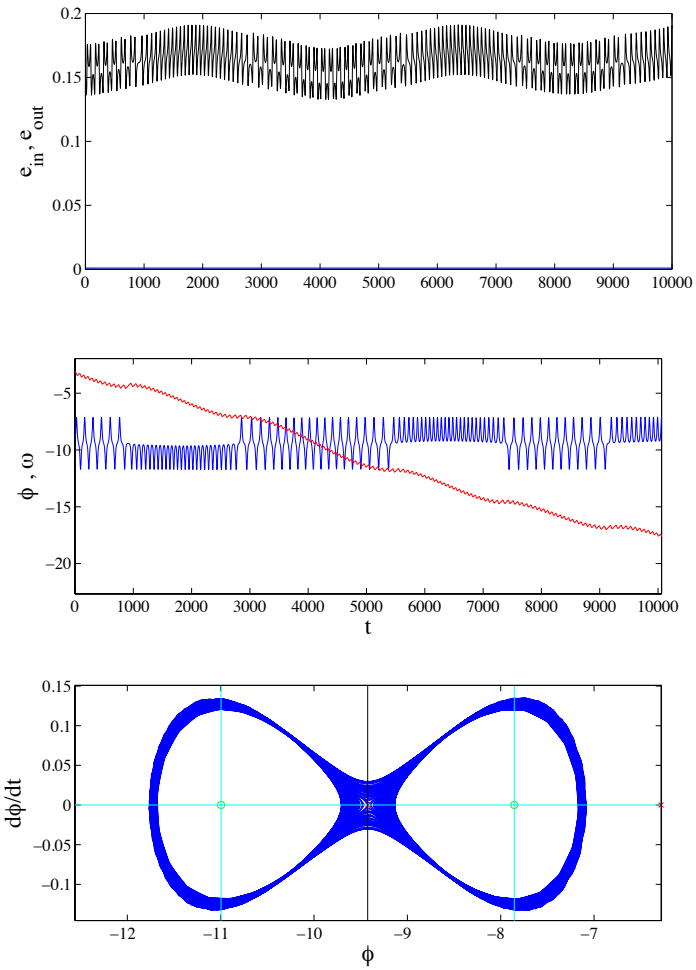

Figure 4.3: External 2:1 near-MMR with ϕ_0 near unstable fixed point at $\phi = \pi$. External 2:1 near-resonance with periapses initially anti-aligned ($\Delta\varpi \approx \pi$), test body near apastron at conjunction ($f_0 \approx \pi$), and a nearly circular planetary orbit with eccentricity $e_p = 10^{-3}$. The *top panel* shows the time series of the test body's eccentricity (black curve – taking values between $0.14 \lesssim e \lesssim 0.18$) and the planet's eccentricity (blue curve – nearly constant at $e_p \simeq 10^{-3}$). The *middle panel* shows the resonance angle, ϕ (blue curve), and the angle of apsides, $\Delta\varpi$ (red curve). The resonance angle jumps between two points of attraction located near $\pi/2$ and $3\pi/2$ (mod 2π) – sometimes librating around one of these two points many times (e.g., for times between $1000 \lesssim t \lesssim 3000$) before jumping to the opposite point of attraction – this is one form of nodding. The *bottom panel* shows the resonance angle's phase trajectory for the entire 10^4 years of simulation. This trajectory traces out a complex dance around the inner separatrix of the phase space of the external 2:1 asymmetric resonance. The behaviors of the test body's eccentricity, the nodding of the resonance angle, and the circulation of the angle of apsides are all intrinsically linked together through the secular interactions between the planet and test body.

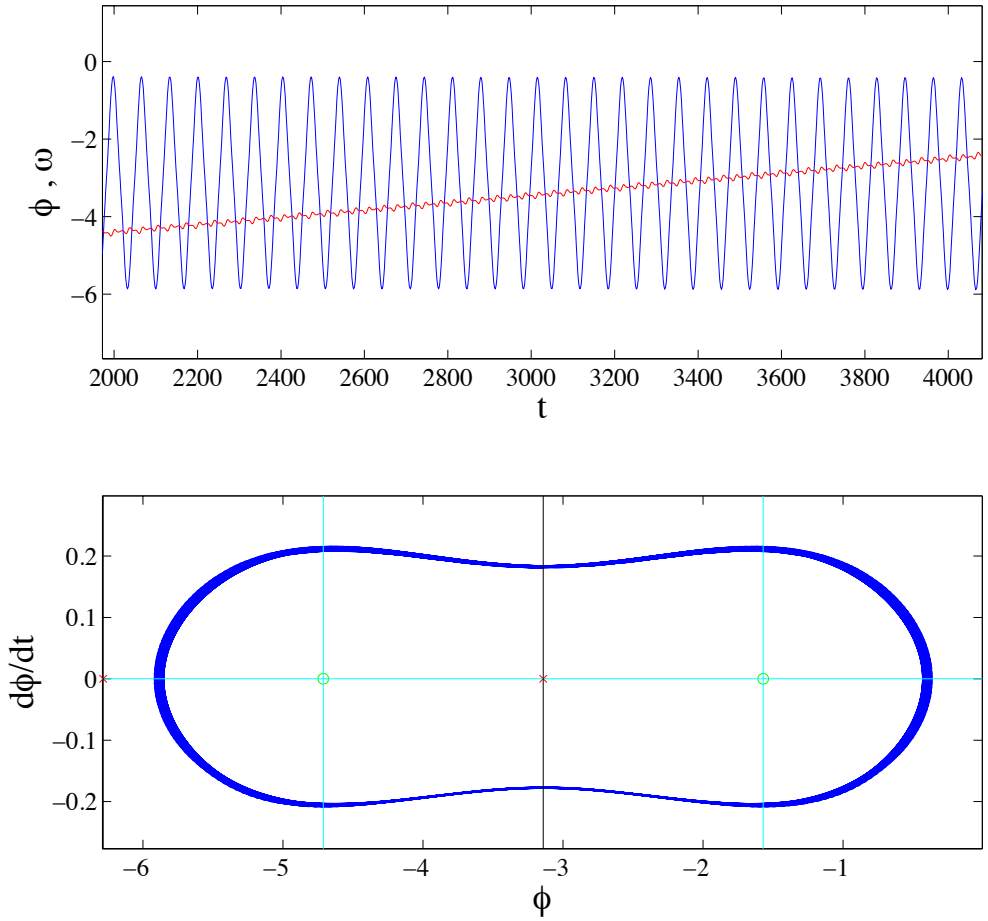

Figure 4.4: External 2:1 near-MMR with $\phi_0 \approx \pi/4$. External 2:1 near-resonance with periapses initially anti-aligned ($\Delta\varpi \approx \pi$), test body displaced $\approx 40°$ from periastron at conjunction ($f_0 \approx \pi/4$), and a nearly circular planetary orbit with eccentricity $e_p = 10^{-3}$. The *top panel* shows the resonance angle, ϕ (blue curve), and the angle of apsides, $\Delta\varpi$ (red curve). The resonance angle repeatedly jumps between two points of attraction located near $\pi/2$ and $3\pi/2$ (mod 2π) – this behavior is one form of nodding. The *bottom panel* shows the resonance angle's phase trajectory for the entire 10^4 years of simulation. The resonance angle's motion temporarily slows as it passes apoastron of the test body's orbit $\phi \approx -\pi$, and accelerates producing sharper peaks in the resonance angle signal of the top panel, in contrast to the internal resonance case (compare with Figure 4.2).

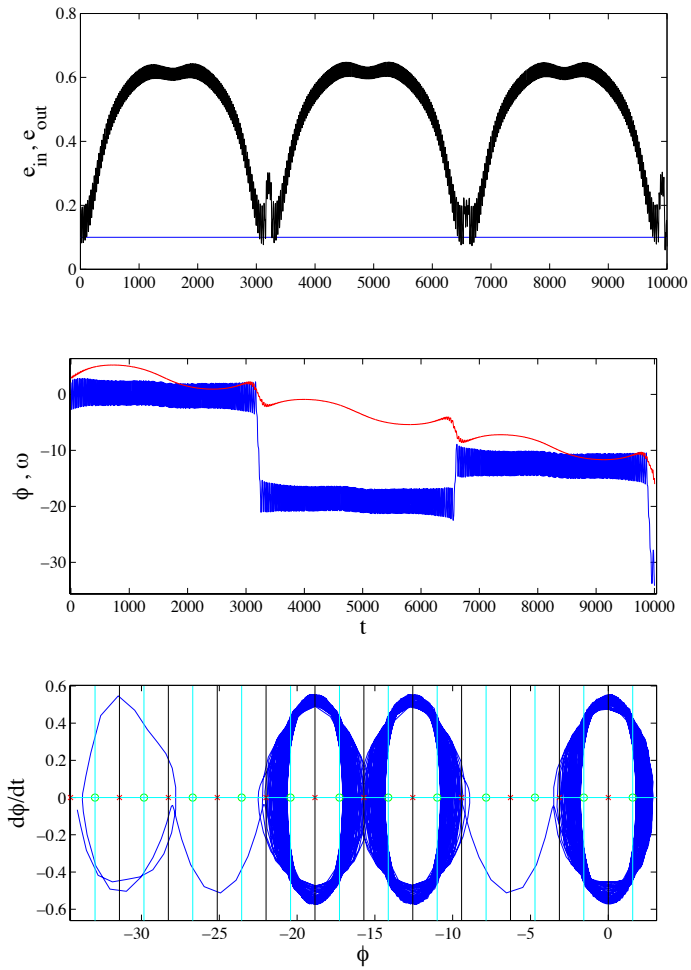

Figure 4.5: Internal 2:1 near-MMR with large ϕ amplitude and moderate $e_p = 0.1$. Internal 2:1 near-resonance, periapses initially aligned ($\Delta\varpi \approx 0$), test body near apastron during initial conjunction ($f_0 \approx \pi$), and the external planet's orbit with eccentricity is $e_p = 0.1$. The *top panel* shows the eccentricity time series for both the test particle (black curve) and the planet (blue curve). The test body's eccentricity reaches values in excess of $e \gtrsim 0.6$ and as low as $e \lesssim 0.1$, the planet's orbital eccentricity does not vary significantly. The *middle panel* shows the time series for the resonance angle (in blue) and $\Delta\varpi$ (in red). The resonance angle librates about $\phi \approx 0$ with a varying amplitude $\pi/2 \lesssim \Delta\phi \lesssim \pi$ for large stretches of time, and suddenly circulates once (at time close to $t \approx 6500$ years) or twice (at time $t \approx 3000$ years). This is a form of nodding. The moments in time where the nodding events occur are correlated with the times that the test body's orbital eccentricity is comparable to the planet's orbital eccentricity, $e \simeq e_p$, and to times when the orbits are aligned (the angle of apsides $\Delta\varpi \approx 0$ modulo 2π). The *bottom panel* shows the corresponding phase trajectory of the resonance angle, $\dot{\phi}$ vs ϕ.

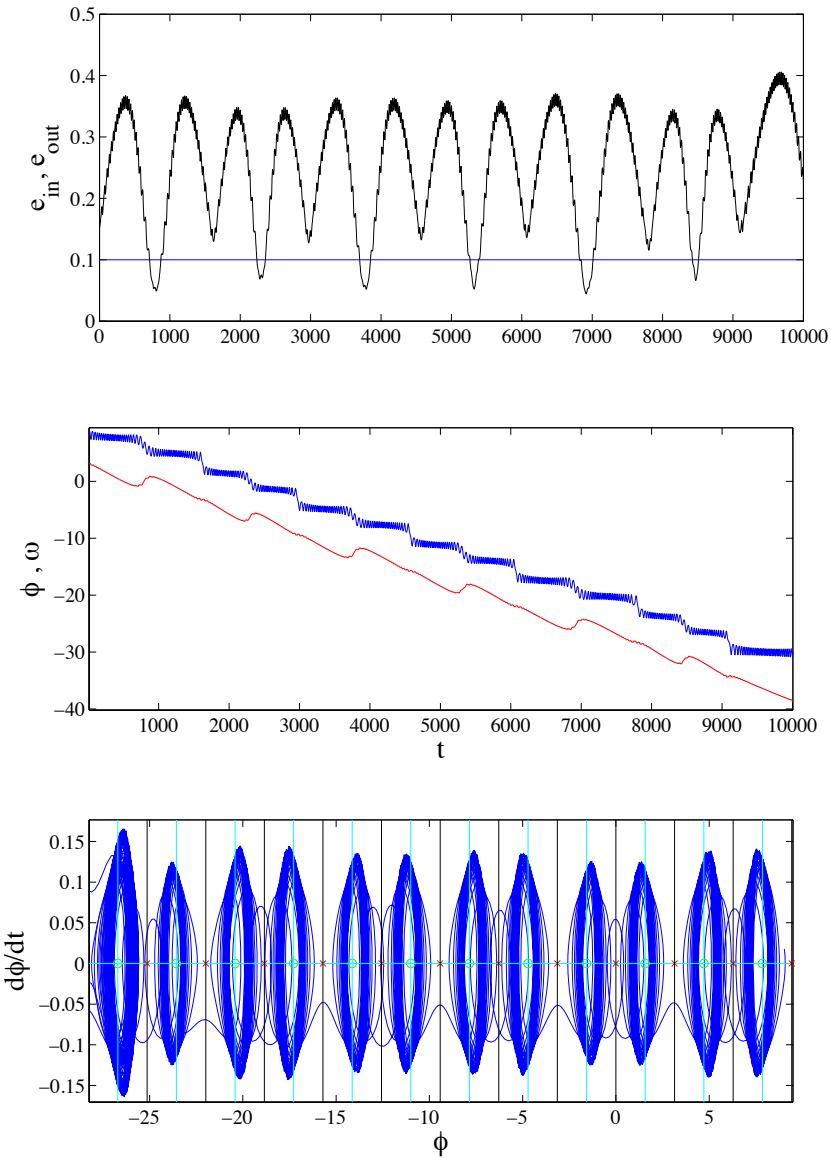

Figure 4.6: External 2:1 near-MMR with $\phi_0 \approx \pi$ and moderate $e_p = 0.1$. External 2:1 near-resonance, periapses anti-aligned ($\Delta\varpi \approx \pi$), test body near apoastron during initial conjunction ($f_0 \approx \pi$), and planet on an eccentric orbit with $e_p = 0.1$. The *top panel* shows the eccentricity time series for both the test particle (black curve) and the perturber (blue curve). The planet's eccentricity remains nearly constant during the simulation, while the test body's eccentricity reaches values up to $e \approx 0.4$ and down to $e \approx 0.05$. The *middle panel* shows the time series for the resonance angle (in blue) and $\Delta\varpi$ (in red). The *bottom panel* shows the phase trajectories of the resonance angle, $\dot{\phi}$ vs ϕ. The behaviors of the test body's eccentricity, the nodding of the resonance angle, and the circulation of the angle of apsides are all intrinsically linked together through the secular interactions between the planet and test body.

parameter space outlined by the above conditions contains 28,560 points, each of which are integrated for up to 200,000 orbits of the Jovian planet ($\approx$ 2000 years). During each individual simulation, we keep track of the angular displacement of both the resonance angle ϕ and the angle of apsides $\Delta\varpi$, as well as the total number of times the resonance angle passes the test body's periastron (a rough measure of the number of circulation events undergone during the simulation).

The results of the survey are shown as a dynamical map in Figure 4.7. Each pixel in the figure is composed of an admixture of the three colors red, green, and blue. The amount of each color within a given pixel represents different behavioral characteristics of the angles of interest: *(i)* Red measures the resonances angle's final angular displacement, *(ii)* Green measures the angle of apsides final angular displacement, and *(iii)* Blue measures the resonance angle's final angular displacement in comparison to the total number of circulation occurrences during the given simulation. We use the ensemble averages for each category to gauge the overall shade of each color of the survey.

Admittedly, our metric for defining each color's particular shade in each pixel is somewhat arbitrary, so we refrain from providing specific details about it here. However, in general our metric produces a bright color for smaller deviations from the initial state in comparison to the ensemble's average deviation, and a darker shade corresponds to a larger deviation than average. We provide a brief interpretation of the prevalent color combinations presented in the figure as follows: *RED:* ϕ strictly librates (no circulation events) and $\Delta\varpi$ circulates; *YELLOW:* Both ϕ and $\Delta\varpi$ librate (minimal circulation); *GREEN:* $\Delta\varpi$ librates, but ϕ circulates quickly; *PURPLE:* ϕ circulation events encountered, but direction of circulation is erratic, and $\Delta\varpi$ ciruclates; *CYAN:* relatively few circulation events for both ϕ and $\Delta\varpi$ and direction of circulation is consistent; *BLACK:* both ϕ and $\Delta\varpi$ circulate rapidly; *BLANK:* either *(i)* premature termination of the simulation due to a scattering or collision event for the test body, or *(ii)* a period ratio between the planet and test body that deviates by more than 10% once the simulation reaches its time limit.

The details appearing in the Figure 4.7 are intricate and rich, and should be explored further in future work. There is one main feature that we want to emphasize here, which is an apparent pitchfork bifurcation occupying this mapping. For low test body eccentricities, rapid circulation occurs for initial apsidal angles, indicated by the thin horizontal tracks of dark (almost black) pixels located around $\Delta\varpi = \pm\pi/2$. As the eccentricity is increased, these tracks converge to a single horizontal line at the center of the map, where at $e \approx 0.1$ rapid circulation of both ϕ and $\Delta\varpi$ occurs for

initial apsidal angle $\Delta\varpi \approx 0$. This trend in the dynamics of the resonance angles as the exterior test body's eccentricity is increased is consistent with past studies (e.g., Lee, 2004) and, perhaps, reveals further details about the onset of the asymmetric exterior 2:1 resonance.

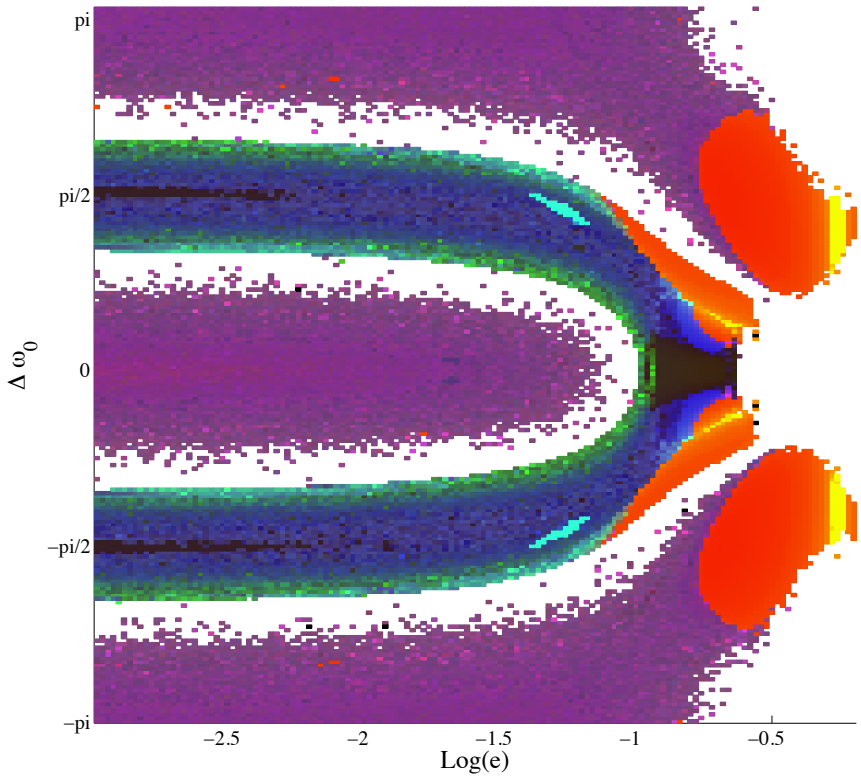

Figure 4.7: Dynamical map of the resonance angle nodding for the external 2:1 near-MMR. Dynamical map of the resonance and apsidal angles' relative amounts of accumulated circulation during simulations lasting 200,000 orbits ($\approx$ 2000 years) for the external 2:1 near-resonance. Each pixel in this figure represents one simulation with a given initial apsidal angle, $\Delta\varpi$ (vertical axis), and test body orbital eccentricity, $\log_{10} e$ (horizontal axis). This figure is a mosaic of 28,560 different simulations performed as described in the text. Each pixel is colored with an admixture of red, green, and blue. The particular shade of each color signifies the relative amount of circulation, hence nodding, using three different metrics – see text for full description. This set of simulations was performed under the context of a Hot Jupiter scenario, i.e., the planet has eccentricity $e_p = 0.04$, mass $m_p = 1$ M$_{Jup}$, and period $T_p = 4$ days, and the test body has mass $m \approx 1 M_\oplus$ and period $T = 8$ days, both orbiting a $1 M_\odot$ star. Each simulation begins with the planet and test body located at periastron of their respective orbits. This figure shows what looks like a pitchfork bifurcation in this parameter space (perhaps due to the transition from symmetric to asymmetric resonances following from left to right across map). For low test body eccentricities, rapid circulation occurs for initial apsidal angles $\Delta\varpi = \pm\pi/2$, and as the initial eccentricity increases, these tracks converge in the center, where, at $e \approx 0.1$, rapid circulation occurs for states with an initial apsidal angle $\Delta\varpi \approx 0$.

4.3.4 Transit Timing Variations in the Presence of Nodding

One potential channel for discovering terrestrial sized exoplanets involves observing variations in the transit times for a Hot Jupiter. These transit timing variations (TTV) will be largest if the body responsible for the variations is in (or near) a mean motion resonance with the Hot Jupiter. Of the multiple-planet systems known to date, many of the adjacent planet pairs have period ratios that are close to small integer ratios, with 2:1, 3:2, and 3:1 being the most populated, in order of decreasing frequency (e.g., Fabrycky et al., 2012). These observations suggest that a planet, whose presence produces transit timing variations of a transiting Hot Jupiter, is more likely to be near MMR, not deep in MMR with the Hot Jupiter. On the other hand, planet-pairs may still be deep in resonance while the ratio of their orbital periods deviates from exact resonance by as much as 20% (e.g., Batygin & Morbidelli, 2013). As shown in the previous section, planetary systems near MMR can exhibit distinctive and interesting resonance angle nodding behaviors, which can lead to interesting signatures in TTVs.

To demonstrate the possible effect of nodding on transit timing variations of a Hot Jupiter, we perform additional simulations. We place two planets in orbit around a $1M_{\odot}$ star – a $1M_{Jup}$ planet in a 4 day orbit and a $10M_{\oplus}$ planet in an 8 day orbit. The periastra are approximately anti-aligned $\Delta\varpi \approx \pi$, and the planets are initially placed near conjunction with the Hot Jupiter at periastron. The orbits were set to be coplanar with initial eccentricities $e_p = 0.1$ and $e = 0.15$ for the Hot Jupiter and Super Earth, respectively. We then performed numerical integrations using the integration scheme described above and recorded the times that the center-to-center displacement between the star and Hot Jupiter were parallel to some arbitrary line of sight. Neither light travel time nor transit duration variations are corrected for during the simulations – a more rigorous study should take into account the light travel time from the star to the Hot Jupiter, and should consider the surface-to-surface grazing chord between the star and Hot Jupiter as the line-of-sight rather than the center-to-center line (Veras et al., 2011). However, these are higher order corrections and are not considered here.

Figure 4.8 shows the results of one such simulation. The resonance angle, shown in blue on the top panel, begins in one mode of oscillation, caught in libration while being passed back and forth between fixed points near $-\pi/2$ and $-3\pi/2$, before settling on the $-3\pi/2$ fixed point for nearly 20 librations. At $t = 10$ years (≈ 1000 orbits), the periastra have rotated into near alignment $\Delta\varpi \approx 0$, and the resonance angle undergoes a different type of nodding than exhibited at the beginning, one which is

characterized by free circulation across the unstable point located at $\phi = -2\pi$. Near the 12 year mark, the resonance angle enters into a mode of libration around a single fixed libration point at $\phi \simeq -5\pi/2$. This libration undergoes around 20 oscillations, at which time the cycle starts over from the beginning and is repeated several times. The particular secular cycle illustrated here, which produces the nodding pattern, is similar to that exhibited by the system represented in Figure 4.6; the initial orbital configurations are nearly identical. However, the test body's mass in this case, a Super Earth with $m = 10M_{\oplus}$, is much larger and the two planets are located much deeper inside the stellar potential than in the previous case, deep enough that stellar damping plays a role in the dynamics. These two differences contribute to produce the different signatures of the nodding patterns for the two cases.

The transit timing variations described above and shown in Figure 4.8 exhibit many different modes of oscillation. In addition, this figure shows that it is plausible that the transit timing variations closely follow the time derivative of the resonance angle. When the resonance angle is nodding between the fixed points on either side of π, the derivative $\dot{\phi}$ decreases as ϕ passes π, and then increases before ϕ reaches the stable point opposite π and reverses direction. This type of motion qualitatively matches the transit timing variations calculated during the same period of time. When the resonance angle increases, the transit timing variations are positive; when the angle ϕ decreases, the TTVs are negative; and when the angle passes through π, the angle slows down and the TTVs decrease. This complicated behavior is depicted by the 'double-peaked' patterns in Figure 4.8 between $t = 0 - 2$ years and $t = 20 - 25$ years.

The bottom panel in Figure 4.8 shows the Fourier Transforms of the TTV signal in 3 year windows which encapsulate times corresponding to the three different modes of libration exhibited by the resonance angle's nodding cycle. The three different power spectra in the bottom panel are color coded and correspond to the regions in the TTV signal highlighted with the same color. Accordingly, the dashed blue curve is the FT for the portion of the TTV signal in the middle panel that is highlighted in blue, near $t \sim 5 - 8$ years. During this window, the resonance angle librates around a single fixed point, and the peak frequency given by the FT is $f \sim 3$ yr^{-1}. The red FT curve is from the TTV signal in the time window of $t \sim 10 - 13$ years, which corresponds to a dynamical state of the system which exhibits a net resonance angle circulation with aligned orbits. The peak frequency of the red FT curve is $f \sim 1$ yr^{-1}. And the green FT curve from the TTV signal between $t \sim 21 - 24$ years has a wide peak frequency $f \sim 0.5 - 0.8$ yr^{-1}. So, for this system, depending on when

the transit times are observed, a three year observational period of TTVs can yield a range of fundamental frequencies that span a factor of ~ 4.

Figure 4.9 shows an identical scenario to Figure 4.8, except that the outer planet mass is taken to be $1M_{\oplus}$ rather than $10M_{\oplus}$. The behavior of the resonance angle is nearly the same, except with larger resonance frequencies. The transit timing variations calculated for the Hot Jupiter in this case contain all of the same qualitative features discussed in the Super Earth example, but the signal's amplitude is smaller by about a factor of 10 – the same factor by which the outer planet's mass has been reduced.

We conclude this section by deriving a relation between TTV amplitudes (for the Hot Jupiter scenarios outlined above) and the time rate of change for the resonance angle, $\dot{\phi}$. The applicable resonance angle for this situation is given in equation (4.2). The second time derivative for the resonance angle is given by

$$\begin{aligned} \ddot{\phi} &= (p+q)(\dot{n}+\ddot{\underline{\epsilon}})_{se} - p(\dot{n}+\ddot{\underline{\epsilon}})_{hj} - q\ddot{\varpi}_{se} \\ &\approx (p+q)\dot{n}_{se} - p\dot{n}_{hj} \ . \end{aligned} \tag{4.3}$$

Lagrange's planetary equations of motion provide us with the time rate of change for the mean motion for both the Hot Jupiter and the Super Earth in this problem,

$$\dot{n}_{se} = -\frac{3}{a_{se}^2}(p+q)\partial_{\phi}\mathcal{R}_I \ , \tag{4.4}$$

$$\dot{n}_{hj} = \frac{3}{a_{hj}^2}p\partial_{\phi}\mathcal{R}_E \ , \tag{4.5}$$

where $\mathcal{R}_I$ and $\mathcal{R}_E$ are the disturbing functions for an internal and external perturber, respectively. Using a simple, time averaged form for the internal disturbing function,

$$\mathcal{R}_I = \frac{\mathcal{G}m_{hj}}{a_{hj}}\left[\alpha\mathcal{S} + \mathcal{F}_{\rm I}e_{se}\cos\phi\right] \ , \tag{4.6}$$

and the external disturbing function,

$$\mathcal{R}_E = \frac{\mathcal{G}m_{se}}{a_{se}}\left[\mathcal{S} + \mathcal{F}_{\rm E}e_{se}\cos\phi\right] \ , \tag{4.7}$$

where $\mathcal{S}$ is the secular contribution to the disturbing function, we substitute these forms into equations (4.4) and (4.5) and get a relation between $\dot{n}_{se}$ and $\dot{n}_{hj}$,

$$\dot{n}_{hj} = -\mu\frac{p}{p+q}\alpha^3\frac{\mathcal{F}_{\rm E}}{\mathcal{F}_{\rm I}}\dot{n}_{se} \ , \tag{4.8}$$

where $\mu \equiv m_{se}/m_{hj}$ is the ratio of planet masses. In the case of a 2 : 1 resonance, $\alpha \approx 2^{-2/3}$, and the portion of equation (4.8) that depends on α simplifies to

$$\alpha^3 \frac{\mathcal{F}_{\rm E}}{\mathcal{F}_{\rm I}} \simeq \alpha^3 \frac{f_{31} - 2\alpha}{\alpha f_{31} - (2\alpha)^{-1}} = \alpha^2 \ . \tag{4.9}$$

Substituting this simplification into equation (4.8) and combining the result with the approximate form for the second time derivative in equation (4.3), we find an expression relating the time rate of change for the Hot Jupiter's orbital period to the second time derivative of the resonance angle,

$$\frac{\dot{T}}{T^2} \approx \frac{\mu}{2^3 \pi \alpha^2} \ddot{\phi} \ , \tag{4.10}$$

where we have made use of the relation $\dot{n} = -2\pi T^2 \dot{T}$ in this last line. Neglecting time variations in α, equation (4.10) can be directly integrated (over one orbit of the Hot Jupiter) to give us the desired relation between transit timing variations, ΔT, and the time derivative of the resonance angle, $\dot{\phi}$,

$$\Delta T \approx \frac{\mu T_j^2}{2^{5/3}\pi} \dot{\phi} \ . \tag{4.11}$$

To demonstrate the accuracy of this equation, we take Figure 4.8 as an example. At peak TTV in Figure 4.8 (near the 7 year mark in the TTV panel of the figure), the resonance angle is changing at a rate of ≈ 12 rad yr^{-1} $\sim 3.8 \times 10^{-7}$ rad sec^{-1}. The Hot Jupiter's period is roughly 4 days ($\sim 3.5 \times 10^5$ sec), and the outer planet has mass $m \approx 10 M_\oplus$ ($\mu \approx 0.03$). Substituting these quantities into the right hand side of equation (4.11) gives $\Delta T \approx 150$ sec, a result which is in good agreement with the figure. This result shows that the any TTV signal found should reveal the intricate details about near resonance nodding if such a system happens to exist in nature. This result also confirms that the strength of the TTV signal increases with the mass of the exterior planet (Agol et al., 2005), which is shown graphically in Figures 4.8 and 4.9. As the test particle's mass decreases by a factor of 10 from Figure 4.8 to Figure 4.9, so does the amplitude for the simulated TTV signal. By equation (4.11), the TTV signal appears to increase with the square of the Hot Jupiter's orbital period, however $\dot{\phi}$ itself is inversely proportional to the period. So, the TTV amplitudes are directly proportional to the orbital period.

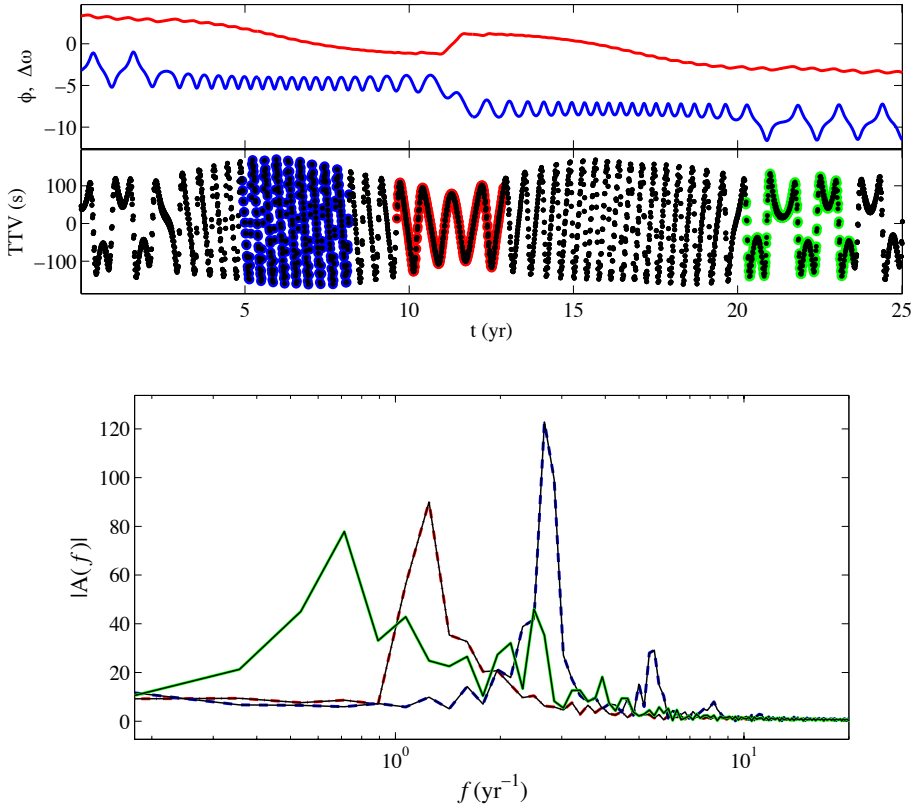

Figure 4.8: Transit timing variations for external 2:1 MMR nodding, $m_1 = 1M_{Jup}$, $m_2 = 10M_{\oplus}$. Results for a Hot Jupiter in a 4 day orbit and in an external 2:1 near-MMR with a Super Earth (with mass $m \approx 10M_{\oplus}$), both orbiting a $1M_{\odot}$ star. The *top panel* shows the time series for the resonance angle ϕ (blue curve) and the angle of apsides $\Delta\varpi$ (red curve) for the first 25 years ($\approx$ 2000 Hot Jupiter orbits). The configuration of this system was prepared to obtain a resonance angle nodding state. The *middle panel* shows transit timing variations in seconds for the Hot Jupiter during the simulation. The TTV amplitude varies in accordance with $\dot{\phi}$ – see equation (4.11) – and attains values as high as $\Delta T \approx 150 - 160$ seconds. Three separate 3-year windows highlight the TTV data (corresponding to different nodding modes of the resonance angle) in the colors (from left to right) blue, red, and green. Fourier Transforms for each highlighted portion are shown in the *bottom panel*, and are color coded to match their corresponding progenitive TTV signal. This bottom panel demonstrates that the fundamental frequency of the TTV signal for a system undergoing nodding motion can vary by a factor $\sim$ 2 (either way) depending on resonance angle nodding effects.

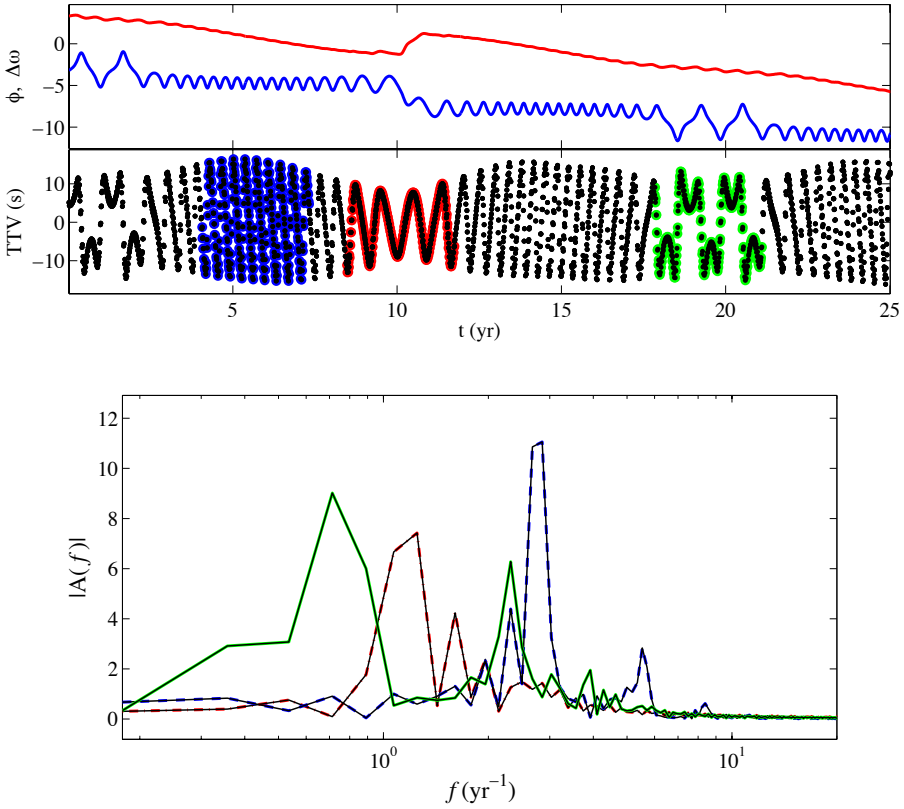

Figure 4.9: Transit timing variations for external 2:1 MMR nodding, $m_1 = 1M_{Jup}$, $m_2 = 1M_{\oplus}$. Results for a Hot Jupiter in a 4 day orbit and in an external 2:1 near-MMR with a Earth-size planet (mass $m \approx 1M_{\oplus}$), both orbiting a $1M_{\odot}$ star. The *top panel* shows the time series for the resonance angle ϕ (blue curve) and the angle of apsides $\Delta\varpi$ (red curve) for the first 25 years ($\approx$ 2000 Hot Jupiter orbits). This system was prepared to obtain a resonance angle nodding state. The *middle panel* shows transit timing variations in seconds for the Hot Jupiter. The TTV amplitude varies in accordance with $\dot{\phi}$ – see equation (4.11) – and attains values as high as $\Delta T \approx 15$ seconds. TTV amplitudes are a factor of 10 smaller than those for a Super Earth (shown in Figure 4.8), demonstrating that TTV amplitudes scale with the outer planet's mass. Three separate 3-year windows highlight the TTV data (corresponding to different nodding modes of the resonance angle) in the colors (from left to right) blue, red, and green. Fourier Transforms for each highlighted portion are shown in the *bottom panel*, and are color coded to match their corresponding progenitive TTV signal. The fundamental frequency of the TTV signal can vary by a factor of ~ 2, depending on the observational time window used.

4.4 Derivation of Model Equations for Nodding

In this section, we turn our attention to a Lagrangian formalism for the scenarios outlined in section 2. We analyze the equation of motion for the resonance angle in the restricted 3-body problem in order to identify the terms that encapsulate the dynamics of nodding. We choose a Lagrangian formulation instead of a Hamiltonian treatment purely for ease of physical interpretation. Consider three point masses that follow a hierarchical arrangement, $m_t \ll m_p \ll m_*$, where we denote orbital elements belonging to the test body with subscript t and those belonging to the planet with p. The three bodies are spatially separated so that m_t and m_p are gravitationally bound to m_*, but not bound to one another. Furthermore, suppose the orbits for m_t and m_p are coplanar, so they orbit m_* in the same plane. In what follows, first we provide a general treatment of the equations where we do not specify whether the planet's orbit is interior or exterior to the test body's orbit, but will later focus on the internal perturber case where $a_p < a_t$. The system sketched in the above outline is the planar restricted 3-body problem. This coming derivation follows a mathematical approach similar to that used in the text by Murray & Dermott (1999).

The argument angles (and hence the resonance angle), ϕ, for the disturbing function in the planar 3-body problem are given by a linear combination of the Eulerian angles

$$\phi = j_t\lambda_t + j_p\lambda_p + k_t\varpi_t + k_p\varpi_p \,, \tag{4.12}$$

where j_t, j_p, k_t, and k_p are integers, which sum to 0, $j_t + j_p + k_t + k_p = 0$. For such a system in resonance, $|j_p| : |j_t|$ is a ratio of small integers, and j_p and j_t are of opposite sign. From simulations, we found that the angle that tends to librate first is the angle corresponding to that of the circular restricted 3-body problem, i.e., where $k_p \equiv 0$ in the case where the perturbing planet's orbit is strictly circular. This is because the strength functions associated with the resonance angle (besides those of the secular angles) are proportional to k_p factors of the planet's orbital eccentricity e_p and k_t factors of the test body's orbital eccentricity e_t. The perturbing planet and the primary mass (star) form a nearly Keplarian system. As a result, we assume that $\dot{\lambda}_p \approx n_p$ in this derivation. From this point forward, we note that orbital elements appearing without a subscript belong to the test body.

We find the first time derivative for the resonance angle

$$\dot{\phi} = j_t\,(n + \dot{\underline{\epsilon}}) + j_p n_p - (j_p + j_t)\dot{\varpi} \;, \tag{4.13}$$

where the quantity

$$\underline{\dot{\epsilon}} = \dot{\epsilon} + \dot{n}\, t \tag{4.14}$$

is introduced to avoid explicit time occurrences in the equation of motion (Brouwer & Clemence, 1961) and where $\dot{n}$ in equation (4.14) may originate from both damping effects and the disturbing function. In the above derivation, it is important to note a few things. From this point forward we use the following notation; partial derivatives written as ∂_q operate only on explicit occurrences of the variable q, and otherwise vanish. Using a lowest eccentricity order form of Lagrange's planetary equations of motion for $\underline{\dot{\epsilon}}$ and $\dot{\varpi}$, we can write

$$\dot{\varpi} = \frac{1}{na^2 e}\partial_e \mathcal{R} \ , \tag{4.15}$$

and

$$\underline{\dot{\epsilon}} = -\frac{2}{na}\partial_a \mathcal{R} + \frac{e}{2na^2}\partial_e \mathcal{R} = \mathcal{S}_A \frac{2\alpha}{na^2}\partial_\alpha \mathcal{R} + \frac{e^2}{2}\dot{\varpi} \ , \tag{4.16}$$

where $\mathcal{R}$ is the disturbing function (for either an interior or an exterior perturber), and where we introduce $\mathcal{S}_A$ with $\mathcal{S}_A = \{1, -1\}$ for an internal or external perturber, respectively; this sign function arises from a change of variables from a_t to α, i.e., $a\partial_a = -\mathcal{S}_A \alpha \partial_\alpha$. We can rewrite equation (4.13) as

$$\dot{\phi} = \left(j_t + \mu \alpha^{\mathcal{S}_B} \mathcal{P}(\mathcal{R})\right) n + j_p n_p \ , \tag{4.17}$$

where $\mu = m_p/m_*$ is the mass ratio between the planet and the star, we introduce the quantity $\mathcal{S}_B$ where $\mathcal{S}_B = \{0, 2\}$ for an internal or external perturber, respectively; we have also introduced the linear differential operator $\mathcal{P}$ defined as

$$\mathcal{P} \equiv \Lambda^{-1}(h_\alpha \partial_\alpha - h_e \partial_e) \ . \tag{4.18}$$

In equation (4.18), $\Lambda \equiv \mathcal{G} m_p / a_p$ is the pre-factor to the disturbing function containing dimensionful constants, and we introduce the quantities h_α, h_e, and β defined by

$$\begin{aligned} h_\alpha &\equiv 2 j_t \ \mathcal{S}_A \ , \\ h_e &\equiv \frac{(j_t + j_p)\beta}{\alpha e} \ , \\ \text{and} \qquad \beta &\equiv 1 - \frac{j_t}{j_t + j_p}\frac{e^2}{2} \ . \end{aligned} \tag{4.19}$$

Note that when substituting Lagrange's planetary equation of motion for $\underline{\dot{\epsilon}}$ in equa-

tion (4.16), we have kept contributions from variations to the disturbing function from α, whereas some treatments will ignore these contributions (e.g., MD99), equivalently asserting that $\partial_\alpha \simeq 0$. However, this contribution can be substantially larger (nearly 40 times greater) than the contribution to $\dot{\underline{\epsilon}}$ from the $\dot{\varpi}e^2/2$ term. The form in equation (4.17) makes it easier to take the second time derivative en route to the resonance angle's equation of motion,

$$\ddot{\phi} = \left[j_t + \mu\alpha^{\mathcal{S}_B}\mathcal{P}(\mathcal{R})\right]\dot{n} + \mu n\alpha^{\mathcal{S}_B}\left[\mathcal{S}_B\frac{\dot{\alpha}}{\alpha}\mathcal{P}(\mathcal{R}) + \frac{d}{dt}\left\{\mathcal{P}(\mathcal{R})\right\}\right] . \tag{4.20}$$

Using the form of the operator $\mathcal{P}$ given in equation (4.18), we can apply the chain rule for the time derivative in the last term of equation (4.20) to obtain

$$\frac{d}{dt}\left[\mathcal{P}(\mathcal{R})\right] = \dot{\mathcal{P}}(\mathcal{R}) + \mathcal{P}(\dot{\mathcal{R}}) . \tag{4.21}$$

The time derivative of the $\mathcal{P}$ operator, for constant primary and secondary masses, and constant semi-major axis for the secondary mass, is given by

$$\dot{\mathcal{P}}(\mathcal{R}) = \Lambda^{-1}h_e\left[\frac{\beta^*}{\beta}\left(\frac{\dot{e}}{e}\right) + \mathcal{S}_A\frac{2}{3}\left(\frac{\dot{n}}{n}\right)\right]\partial_e\mathcal{R} , \quad \text{with} \quad \beta^* \equiv 2-\beta , \tag{4.22}$$

and

$$\mathcal{P}(\dot{\mathcal{R}}) = \dot{e}\mathcal{P}(\partial_e\mathcal{R}) + \mathcal{S}_A\frac{2}{3}\frac{\dot{n}}{n}\alpha\mathcal{P}(\partial_\alpha\mathcal{R}) + \dot{\varpi}\mathcal{P}(\partial_\varpi\mathcal{R}) + \dot{\phi}\mathcal{P}(\partial_\phi\mathcal{R}) . \tag{4.23}$$

Combining the previous two results with equation (4.20) gives

$$\begin{aligned}\ddot{\phi} = {} & \frac{\dot{n}}{n}\left[\dot{\phi} - j_p n_p + \mathcal{S}_A\frac{2}{3}\mu n\alpha^{\mathcal{S}_B}\left\{\mathcal{S}_B\mathcal{P}(\mathcal{R}) + \alpha\mathcal{P}(\partial_\alpha\mathcal{R}) + \Lambda^{-1}h_e\partial_e\mathcal{R}\right\}\right] \\ & + \mu n\alpha^{\mathcal{S}_B}\left[\frac{\dot{e}}{e}\left(e\mathcal{P}(\partial_e\mathcal{R}) + \Lambda^{-1}h_e\frac{\beta^*}{\beta}\,\partial_e\mathcal{R}\right) + \dot{\phi}\mathcal{P}(\partial_\phi\mathcal{R}) + \dot{\varpi}\mathcal{P}(\partial_\varpi\mathcal{R})\right] .\end{aligned} \tag{4.24}$$

Equation (4.24) is arranged so that disk damping effects can be easily included into the equation of motion – all time derivative operations of orbital elements have been collected and accounted for and occur as first order time derivatives. With this form, one can simply substitute Lagrange's planetary equations of motion where necessary and remove all implicit instances of time from the equation of motion, i.e., all remaining operators act only as partial derivatives with respect to the orbital elements, independent of time. Along these lines, one could modify the time derivatives of the

orbital elements to include external forces (e.g., damping)

$$\begin{aligned} \dot{n} &= (\dot{n})_{\rm dist} + (\dot{n})_{\rm damp}\,, \\ \dot{e} &= (\dot{e})_{\rm dist} + (\dot{e})_{\rm damp}\,, \end{aligned} \tag{4.25}$$

where $(\dot{q})_{\rm dist}$ represent variations to the orbital element q due to the disturbing function, and $(\dot{q})_{\rm damp}$ are variations caused by external forces due to interactions with, for instance, a circumstellar disk.

4.4.1 Specialization to the Case of External resonances

We will now focus an external $p+q:p$ resonance. For a given angle ϕ from equation (4.12), The simplest time averaged disturbing function (to second order in eccentricity) for an internal perturber takes the form

$$\mathcal{R}_\phi = \Lambda\left[\alpha\left(\mathcal{S}_1 + \mathcal{S}_2\cos\left(\varpi - \varpi_p\right)\right) + \mathcal{R}_D\cos\phi\right]\,, \tag{4.26}$$

where

$$\begin{aligned} \Lambda &\equiv \frac{\mathcal{G}m_p}{a_p}\,, \\ \mathcal{S}_1 &\equiv \left(e^2 + e_p^2\right) f_{s,1}(\alpha)\,, \\ \mathcal{S}_2 &\equiv e e_p f_{s,2}(\alpha)\,, \\ \mathcal{R}_D &\equiv e^q \mathcal{F}_1(\alpha) \quad \text{where} \quad \mathcal{F}_1(\alpha) \equiv \left(\alpha f_d(\alpha) + f_i(\alpha)\right)\,, \end{aligned} \tag{4.27}$$

(MD99). Under this scenario, the following quantities will have values $j_t = (p+q)$, $j_p = -p$, $\mathcal{S}_A = 1$, and $\mathcal{S}_B = 0$. Using the damping forms given above in equation (4.25), we rearrange equation (4.24) algebraically and use the time averaged form of the disturbing function in equation (4.26), and parse the equation of motion into generalized reoccurring operators, trigonometric functions of ϕ and $\Delta\varpi$, and damping terms. Note that, during this expansion, we expand the equation for $\dot{e}$ to the second lowest order in eccentricity to retrieve a form that utilizes the parameter β. This procedure results in an equation of motion of the form

$$\begin{aligned} \ddot{\phi} = &-\sin\phi\left[\mathcal{N}pn_p + (\mathcal{N} + \mu n\Lambda\mathcal{P}(\mathcal{R}_D))\dot{\phi} + \mathcal{J}(\alpha\mathcal{S}_1) + \mathcal{J}(\alpha\mathcal{S}_2)\cos\left(\Delta\varpi\right) + \mathcal{J}(\mathcal{R}_D)\cos\phi\right] \\ &-\sin\left(\Delta\varpi\right)\left[\mu n\dot{\varpi}\Lambda\mathcal{P}(\alpha\mathcal{S}_2) + \mathcal{K}(\alpha\mathcal{S}_1) + \mathcal{K}(\alpha\mathcal{S}_2)\cos\left(\Delta\varpi\right) + \mathcal{K}(\mathcal{R}_D)\cos\phi\right] \\ &+\left[\tilde{\mathcal{N}}(pn_p + \dot{\phi}) + \tilde{\mathcal{J}}(\alpha\mathcal{S}_1) + \tilde{\mathcal{J}}(\alpha\mathcal{S}_2)\cos\left(\Delta\varpi\right) + \tilde{\mathcal{J}}(\mathcal{R}_D)\cos\phi\right]\,. \end{aligned} \tag{4.28}$$

Here, new operators were introduced to compactify notation

$$\begin{aligned}\mathcal{J}(\mathcal{Q}) &\equiv \mathcal{N}\mathcal{P}_n(\mathcal{Q}) + \mathcal{E}_\phi \mathcal{P}_e(\mathcal{Q}) \ , \\ \mathcal{K}(\mathcal{Q}) &\equiv \mathcal{E}_\varpi \mathcal{P}_e(\mathcal{Q}) \ , \\ \tilde{\mathcal{J}}(\mathcal{Q}) &\equiv \tilde{\mathcal{N}}\mathcal{P}_n(\mathcal{Q}) + \tilde{\mathcal{E}}\mathcal{P}_e(\mathcal{Q}) \ ,\end{aligned} \tag{4.29}$$

with

$$\begin{aligned}\mathcal{P}_n(\mathcal{Q}) &\equiv \frac{2}{3}\mu n \left[\alpha\Lambda\mathcal{P}(\partial_\alpha \mathcal{Q}) + h_e \partial_e \mathcal{Q}\right] \ , \\ \mathcal{P}_e(\mathcal{Q}) &\equiv \mu n \left[e\Lambda\mathcal{P}(\partial_e \mathcal{Q}) + h_e \frac{\beta^*}{\beta}\partial_e \mathcal{Q}\right] \ ,\end{aligned} \tag{4.30}$$

where $\mathcal{Q}$ is some function of eccentricities and α given in equation (4.27),

$$\begin{aligned}\mathcal{N} &\equiv -3\ \mathcal{C}(p+q)\mathcal{R}_D \ , \\ \mathcal{E}_\varpi &\equiv -\mathcal{C}\frac{\alpha}{e^2}\mathcal{S}_2 \ , \\ \mathcal{E}_\phi &\equiv\ \mathcal{C}\frac{q\beta}{e^2}\mathcal{R}_D \ ,\end{aligned} \tag{4.31}$$

where $\mathcal{C} = \mu n/\alpha$, and finally

$$\tilde{\mathcal{N}} \equiv \left(\frac{\dot{n}}{n}\right)_{\text{damp}} \quad \text{, and} \quad \tilde{\mathcal{E}} \equiv \left(\frac{\dot{e}}{e}\right)_{\text{damp}} \ .$$

Each line of equation (4.28) can be analyzed to determine what contributions to the resonance angle's equation of motion come from the disturbing function's secular and direct portions ($\mathcal{S}_1$, $\mathcal{S}_2$, and $\mathcal{R}_D$ from equation (4.26)) and what contributions might be expected to arise from external damping forces. The first line of equation (4.28) contains the immediate contributions from the direct part of the disturbing function – that is to say that each term inside the square brackets includes a factor of $\mathcal{R}_D$, but also included are higher order cross term contributions to the motion arising from secular effects on $\mathcal{R}_D$. The second line contains the contribution from the secular parts of the disturbing function – for the *circular* restricted three body problem, this line vanishes. The final line of equation (4.28) originates from the presence of damping forces like those introduced in equation (4.25).

We can expand each operator and determine to what order the eccentricity con-

tributes to the overall magnitude in each individual term therein:

$$\begin{aligned}\mathcal{J}(\alpha\mathcal{Q}) = &-\mathcal{C}^2\mathcal{R}_D - \mathcal{C}^2\mathcal{R}_D h_\alpha^2 \partial_\alpha(\alpha^2\partial_\alpha\mathcal{Q}) + -\mathcal{C}^2\mathcal{R}_D 2\alpha^2 h_\alpha h_e \partial_e\partial_\alpha\mathcal{Q} \\ &- \mathcal{C}^2\mathcal{R}_D\alpha^2 h_e^2\partial_e^2\mathcal{Q} + -\mathcal{C}^2\mathcal{R}_D\left(\frac{q\beta^*}{e^2} + h_\alpha\right)\alpha h_e\partial_e\mathcal{Q}\ ,\end{aligned} \tag{4.32}$$

$$\begin{aligned}\mathcal{J}(\mathcal{Q}) = &-\mathcal{C}^2\mathcal{R}_D h_\alpha^2\alpha^2\partial_\alpha^2\mathcal{Q} + \mathcal{C}^2\mathcal{R}_D 2\alpha^2 h_\alpha h_e\partial_e\partial_\alpha\mathcal{Q} \\ &- \mathcal{C}^2\mathcal{R}_D\alpha^2 h_e^2\partial_e^2\mathcal{Q} + -\mathcal{C}^2\mathcal{R}_D\left(\frac{q\beta^*}{e^2} - h_\alpha\right)\alpha h_e\partial_e\mathcal{Q}\ ,\end{aligned} \tag{4.33}$$

$$\mathcal{K}(\alpha\mathcal{Q}) = -\alpha\mathcal{C}^2 e^{-1}\mathcal{S}_2\left[\alpha^2 h_\alpha\partial_e\partial_\alpha\mathcal{Q} - \alpha^2 h_e\partial_e^2\mathcal{Q} + \left(\frac{q\beta^*}{e^2} + h_\alpha\right)\alpha\partial_e\mathcal{Q}\right]\ , \tag{4.34}$$

$$\mathcal{K}(\mathcal{Q}) = -\mathcal{C}^2 e^{-1}\mathcal{S}_2\left[\alpha^2 h_\alpha\partial_e\partial_\alpha\mathcal{Q} - \alpha^2 h_e\partial_e^2\mathcal{Q} + \left(\frac{q\beta^*}{e^2} + 0\right)\alpha\partial_e\mathcal{Q}\right]\ , \tag{4.35}$$

$$\begin{aligned}\tilde{\mathcal{J}}(\alpha\mathcal{Q}) = &\frac{\mathcal{C}}{\alpha}\frac{2}{3}\tilde{\mathcal{N}}h_\alpha\partial_\alpha(\alpha^2\partial_\alpha\mathcal{Q}) + \frac{\mathcal{C}}{\alpha}\left(\tilde{\mathcal{E}}e\alpha h_\alpha - \frac{2}{3}\tilde{\mathcal{N}}\alpha^2 h_e\right)\partial_e\partial_\alpha\mathcal{Q} \\ &- \frac{\mathcal{C}}{\alpha}\tilde{\mathcal{E}}q\beta\partial_e^2\mathcal{Q} + \frac{\mathcal{C}}{\alpha}\tilde{\mathcal{E}}\frac{q}{e}\left(6 - 5\beta\right)\partial_e\mathcal{Q}\ ,\end{aligned} \tag{4.36}$$

$$\begin{aligned}\tilde{\mathcal{J}}(\mathcal{Q}) = &\mathcal{C}\frac{2}{3}\tilde{\mathcal{N}}\alpha^2 h_\alpha\partial_\alpha^2\mathcal{Q} + \mathcal{C}\left(\tilde{\mathcal{E}}e\alpha h_\alpha - \frac{2}{3}\tilde{\mathcal{N}}\alpha^2 h_e\right)\partial_e\partial_\alpha\mathcal{Q} \\ &- \mathcal{C}\tilde{\mathcal{E}}q\beta\partial_e^2\mathcal{Q} + \mathcal{C}\alpha\left(\tilde{\mathcal{E}}q\beta^* + \frac{2}{3}\tilde{\mathcal{N}}h_e\right)\partial_e\mathcal{Q}\ .\end{aligned} \tag{4.37}$$

It is important to consider the magnitude of each of these operators to determine their significance in the equation of motion given in equation (4.28). Figures 4.10, 4.11, and 4.12 show the resulting magnitudes as a function of the test body eccentricity e for the terms between the square brackets in line 1, 2, and 3 of equation (4.28), respectively.

4.4.2 Analysis of the Expansion Terms

In this section we focus on the $\sin\phi$ part of equation (4.28) – the first line of the equation of motion for the resonance angle. As written in this compact form, there are only five contributing terms contained within the square brackets. The first term, $\mathcal{N}pn_p\sin\phi$, when considered on its own, has been the focus of intense study in the circular restricted three body problem, and is called the pendulum model for obvious reasons. This model can be generalized by expanding each term within the square brackets via equations (4.31), (4.18), (4.27), (4.32), and (4.33) and keeping only the

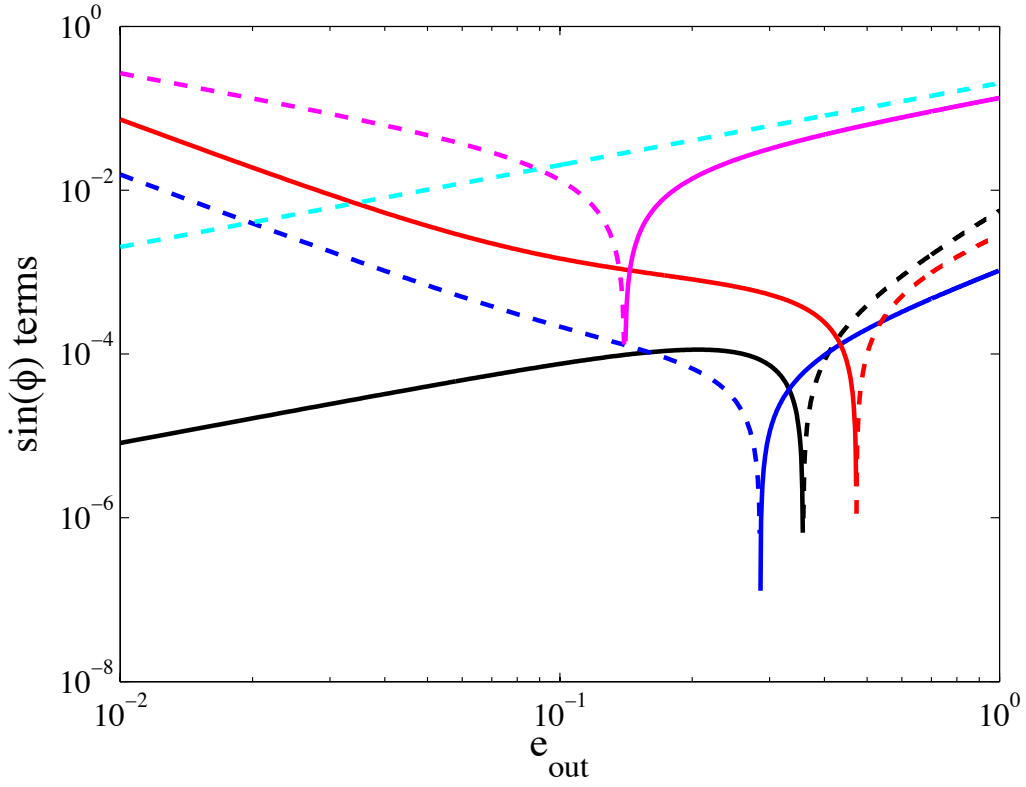

Figure 4.10: Magnitudes of coefficients for $\sin\phi$ terms in equation (4.28). Magnitudes of coefficients for terms appearing in the first line ($\sin\phi$ part) of equation (4.28) as a function of test body eccentricity e. Solid curves represent positive values, and dashed curves negative. The magenta curve is the coefficient to $\dot{\phi}$ (second term in square brackets of line 1 of the equation). The cyan curve is the usual pendulum term (first term). The red curve is $\mathcal{J}(\mathcal{R}_D)$, the coefficient to $\cos\phi$ (last term). The blue curve is $\mathcal{J}(\alpha\mathcal{S}_2)$, the coefficient to $\cos(\Delta\varpi)$ (fourth term). The black curve is $\mathcal{J}(\alpha\mathcal{S}_1)$ (third term). The figure shows that, for low values of eccentricity, the pendulum term is not necessarily the dominant term. The figure depicts values for 2:1 external resonances, with $n = 2\pi$, $\mu = 10^{-3}$, and $e_p = 0.1$.

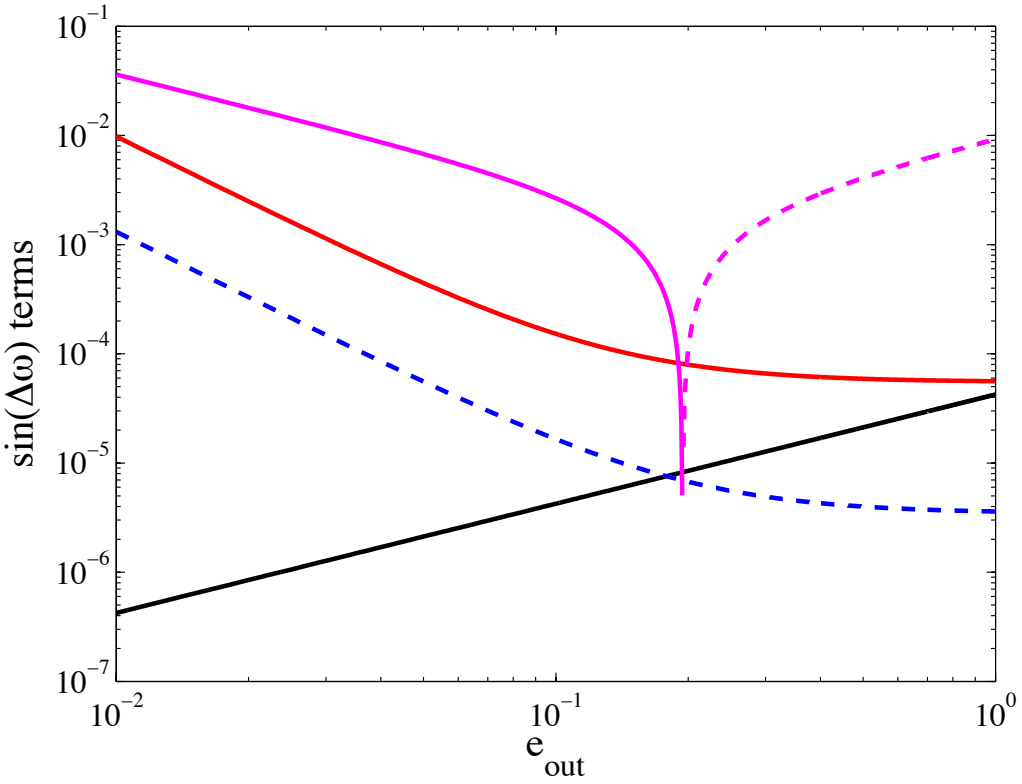

Figure 4.11: Magnitudes of coefficients for $\sin\Delta\varpi$ terms in equation (4.28). Magnitudes of coefficients for terms appearing in the second line ($\sin\Delta\varpi$ part) of equation (4.28) as a function of test body eccentricity e. Solid curves represents positive values, and dashed curves negative. The magenta curve is the coefficient to $\dot{\varpi}$ (first term in square brackets of line 2 of the equation). The red curve is $\mathcal{K}(\mathcal{R}_D)$, the coefficient to $\cos\phi$ (last term). The blue curve is $\mathcal{K}(\alpha\mathcal{S}_2)$, the coefficient to $\cos(\Delta\varpi)$ (third term). The black curve is $\mathcal{K}(\alpha\mathcal{S}_1)$ (second term). The only term independent of additional contributions from the angles (ϕ and $\Delta\varpi$) in this figure is the black curve This figure depicts values for 2:1 external resonances, with $n = 2\pi$, $\mu = 10^{-3}$, and $e_p = 0.1$. The relative magnitudes are dependent on different factors of e_p. All strengths vanish for $e_p = 0$, i.e., for the case of the circular restricted 3-body problem.

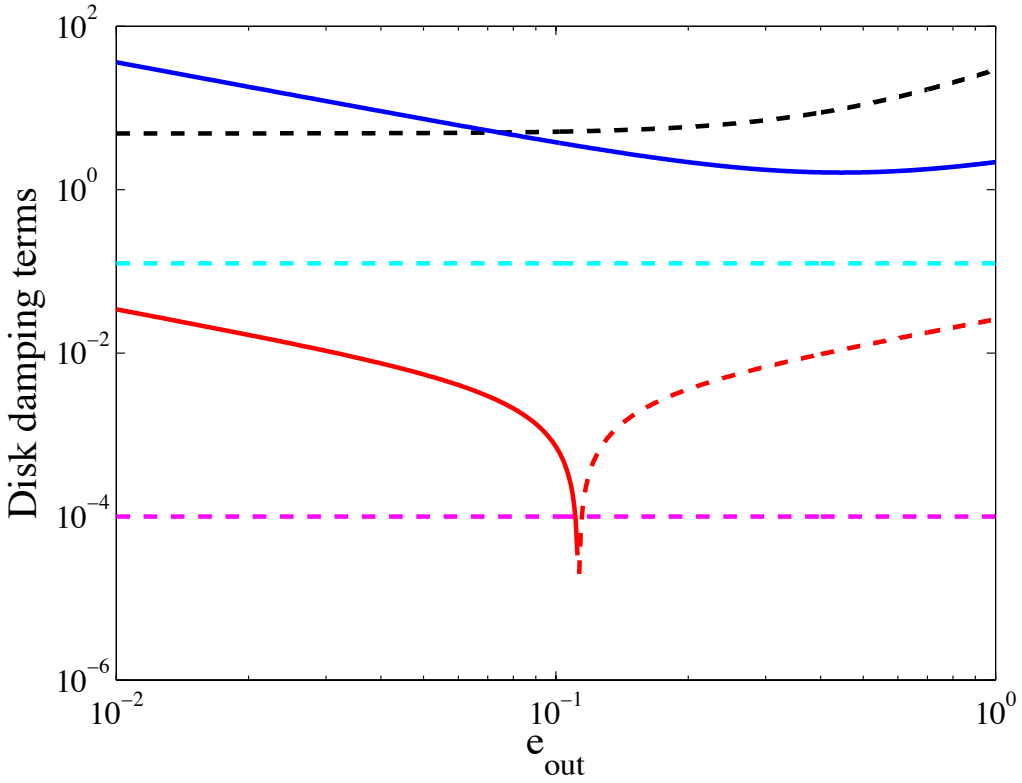

Figure 4.12: Magnitudes of coefficients for damping terms in equation (4.28). Magnitudes of coefficients for terms appearing in the damping terms (third line of the equation) of equation (4.28) as a function of test body eccentricity e, e.g., damping terms that may be considered as contributions to $\dot{n}$ and $\dot{e}$ (in addition to the usual Lagrange planetary equations) as in equation (4.25). Solid curves represent positive values, and dashed curves negative. The magenta curve is the coefficient to $\dot{\phi}$ (the first term). The red curve is $\tilde{\mathcal{J}}(\mathcal{R}_D)$, the coefficient to $\cos\phi$ (fourth term). The blue curve is $\tilde{\mathcal{J}}(\alpha\mathcal{S}_2)$, the coefficient to $\cos(\Delta\varpi)$ (third term) – it is not present in the circular restricted 3-body problem. The black curve is $\tilde{\mathcal{J}}(\alpha\mathcal{S}_1)$ (second term). The cyan curve is $\tilde{\mathcal{N}}pn_p$. This figure depicts values for 2:1 external resonances, with $n = 2\pi$, $\mu = 10^{-3}$, and $e_p = 0.1$. Damping parameters are $\tau_a = 10^4$ years and $\tau_e = 10^3$ years, where we have assumed a simple definition for damping parameters $\dot{a}/a = -\tau_a^{-1}$ and $\dot{e}/e = -\tau_e^{-1}$.

lowest eccentricity order contributions from each. Doing so gives the result

$$\ddot{\phi} \simeq -\sin\phi\big[-3/2 h_\alpha \mathcal{C}(pn_p + \dot{\phi})\mathcal{F}_{\rm I}\, e^q - q^2\mathcal{C}\mathcal{F}_{\rm I}\dot{\phi}\, e^{q-2} + 2\mathcal{C}^2 q h_\alpha \mathcal{F}_{\rm I}(2\alpha\partial_\alpha f_{s,1} + f_{s,1})\, e^q \\ + \mathcal{C}^2 q^2 e_p f_{s,2}\mathcal{F}_{\rm I}\cos(\Delta\varpi)\, e^{q-3} - \mathcal{C}^2 q^3 (q-2)\mathcal{F}_{\rm I}^2\cos\phi\, e^{2(q-2)}\big]\,. \tag{4.38}$$

For non-circular perturber orbits, there is an additional contribution proportional to e_p^2 that has been excluded here, which may be significant given large enough values of e_p. Notice that, depending on the particular value of q, there are up to four different orders of eccentricity that show up, so we collect them in eccentricity order,

$$\ddot{\phi} \simeq -\sin\phi\Big[\mathcal{C}\mathcal{F}_{\rm I} e^q \Big\{2qh_\alpha\mathcal{C}\,(2\alpha\partial_\alpha f_{s,1} + f_{s,1}) - 3(p+q)pn_p - \big(3(p+q) + q^2 e^{-2}\big)\,\dot{\phi}\Big\} \\ + \mathcal{C}^2 q^2 e^{q-3}\mathcal{F}_{\rm I}\left\{e_p f_{s,2}\cos(\Delta\varpi) - q(q-2)e^{q-1}\mathcal{F}_{\rm I}\cos\phi\right\}\Big]\,. \tag{4.39}$$

However, the number of terms shown here can be further reduced. Although we are interested in a lowest eccentricity order study, we must also consider the lowest order terms in $\mathcal{C}\propto\mu$ as well. For a 2:1 period ratio, test body mean motion $n = 2\pi$, mass ratio $\mu \sim 10^{-3}$, and perturber eccentricity $e_p = 0.1$, Figure 4.10 depicts the corresponding relative strengths of each term contributing to the $\sin\phi$ part (first line) of equation (4.28).

For eccentricities $e \sim 0.1$, two terms in the expansion dominate. One term is the usual pendulum term, but the other term is something like a modified damping term (i.e., a term multiplying the time derivative $\dot{\phi}$). Although, $|\dot{\phi}|$ is generally less than unity for instances of libration, contributions from the $\dot{\phi}$ term can become quite large for sufficiently small eccentricities due to its e^{-1} dependence. In the figure, contributions from $\dot{\phi}$ and the pendulum term have the same sign (both curves are dashed lines, meaning less than zero on the log-log plot). To achieve nodding by way of the $\dot{\phi}$ term, one requires $\dot{\phi} < 0$ *in addition to* satisfying the constraint on the upper bound of the eccentricity, $e \leqslant 0.1$. The condition that $\dot{\phi} < 0$ for nodding to occur provides a simple explanation for the observation that the resonance angle tends to circulate on average over secular timescales in a preferred direction, usually resulting in a graph of ϕ versus t which is reminiscent of a stair case. The figure actually shows that this term is comparable to the pendulum term for all values of eccentricity, however it works to counteract the pendulum term for instances where $\dot{\phi} > 0$, and has opportunity to overwhelm the pendulum term only for $|\dot{\phi}| \gtrsim 2$.

Another term of significance appears in equation (4.39). For sufficiently small test body eccentricities, the term that is proportional to $e^{-2}\cos\phi$ plays an important

role. As shown in Figure 4.10, the $\cos\phi$ coefficient (red curve) surpasses the pendulum term (cyan curve) for eccentricities lower than ~ 0.03. The greatest lower bound on eccentricity required for this term to take effect is

$$e \lesssim \left(\frac{\mu \mathcal{F}_{\rm I}\sqrt{\alpha}}{6}\right)^{1/3} .$$

When evaluated using the typical value $\mu = 10^{-3}$ in the external 2:1 case ($\mathcal{F}_{\rm I} \sim 0.27$), the above expression gives the restriction $e \lesssim 0.033$. Note that the $e^{-2}\cos\phi$ term is not present for those resonances with $q = 2$ (e.g., 3:1, 5:3, 7:5, etc...), and has opposite sign for resonances with $q = 3$ (e.g., 4:1, 5:2, 7:4, etc...) and above. However, for resonances of higher rank (higher q values), the eccentricity order increases relative to the order of the pendulum and the $\dot{\phi}$ terms, diminishing its importance.

Keeping only the two largest terms from Figure 4.10, the equation of motion can be reduced to the form

$$\ddot{\phi} \approx \mathcal{C}\mathcal{F}_{\rm I}\sin\phi\left[6n_p e + e^{-1}\dot{\phi} - \mathcal{C}\mathcal{F}_{\rm I}e^{-2}\cos\phi\right] . \tag{4.40}$$

This equation exhibits some of the nodding behaviors we see in the full problem (see section 4.3). The parameters and initial values must be fine-tuned for cases where eccentricities (and periastra) are independent of time (i.e., only special values allow for nodding). Under conditions where the eccentricity has time dependence, however, nodding is a robust phenomenon(it is much easier to find parameters for which nodding occurs). For the sake of simplicity, we adopt the parametric description for the time dependence of eccentricity

$$e(t) = e_0 - e_a \sin^2(\omega_e t) . \tag{4.41}$$

In many instances of nodding found from the numerical studies in section 2 but not featured in the figures, the test body's orbital eccentricity evolves through large swooping double arches, spanning several orders of magnitude, reaching values as high as a few times 10^{-1} and as low as 10^{-2}–10^{-3} (see top panel of Figure 4.6). This double arched pattern exhibited by the test particle's orbital eccentricity is governed by the secular time scale, which typically falls in the range $\sim 10^2 - 10^3$ libration times, but can be much longer (e.g., Michtchenko et al., 2008b). The ansatz of equation (4.41) is used in order to model this behavior.

To demonstrate that this model exhibits some nodding behaviors, we integrate

equation (4.40) using an adaptive fourth order Runge-Kutta integration scheme with e = constant and with $e(t)$ given by equation (4.41). We note that this is a simple study in which the eccentricity evolution being used here is totally prescribed without feedback from the specific orbital parameters, so we do not expect the model to exhibit all of the intricate details exhibited by the full 3-body simulations presented in section 4.3. For the sake of definiteness, we take $n \sim 1$, $\mathcal{C} \sim 10^{-2}$, and $\omega_e \sim 10^{-3}$ yr^{-1} – the precise values of these parameters will depend on the orbital angles and mean motions, and the values we choose corresponds to orbital periods on the order of years, not days. Under the parametrically evolving eccentricity of equation (4.41), nodding is a robust phenomenon, even when considering the pendulum term alone. Guided by the pendulum model of the circular restricted 3-body problem, we take the initial conditions $(\phi, \dot{\phi}) = (\epsilon, 0)$, which places the system in a dynamically vulnerable position near a separatrix – any perturbations that supply additional action should eventually cause the pendulum to circulate rather than oscillate. Figure 4.13 demonstrates how a small amount of eccentricity variation can send such a system into bouts of nodding. However, the system need not be prepared in such a dynamically sensitive manner to see nodding. Figure 4.14 shows a system that would be stable in the absence of variable eccentricity, but where the inclusion of sufficient eccentricity cycling provides enough added action to induce nodding. In both Figures 4.13 and 4.14, we use $\mathcal{F}_{\rm I} \simeq 0.27$, which is the approximate value obtained from equation (4.27) corresponding to a 2:1 period ratio with $\alpha \simeq 0.63$ (see MD99). Figure 4.15 shows the results when taking $\mathcal{F}_{\rm I} = 1$ and using various combinations of the terms in equation (4.40) along with a time varying eccentricity as defined in (4.41). This figure demonstrates that the pendulum model alone is not enough to recover nodding behaviors, but nodding does appear in models that combine the pendulum term with either of the two additional terms in equation (4.40). Taken together, Figures 4.13 – 4.15 show that nodding behavior arises naturally in modified pendulum equations, such as those resulting from the expansion of the previous section.

It may be worth noting that another term in equation (4.39) is of order e^{-2}, which was ignored due to its contribution from e_p. However, this term could be of importance in cases where the test particle's eccentricity is very low ($e \ll e_p$). Including this term leaves us with a form dependent upon $(\Delta\varpi)$,

$$\ddot{\phi} \approx \mathcal{C}\mathcal{F}_{\rm I} \sin\phi \left[6n_p e + e^{-1}\dot{\phi} - \mathcal{C}\mathcal{F}_{\rm I} e^{-2}\cos\phi - \mathcal{C} f_{s,2} e_p e^{-2} \cos\left(\Delta\varpi\right) \right] \ . \qquad (4.42)$$

This equation will exhibit nodding, even for constant eccentricity, as long as the

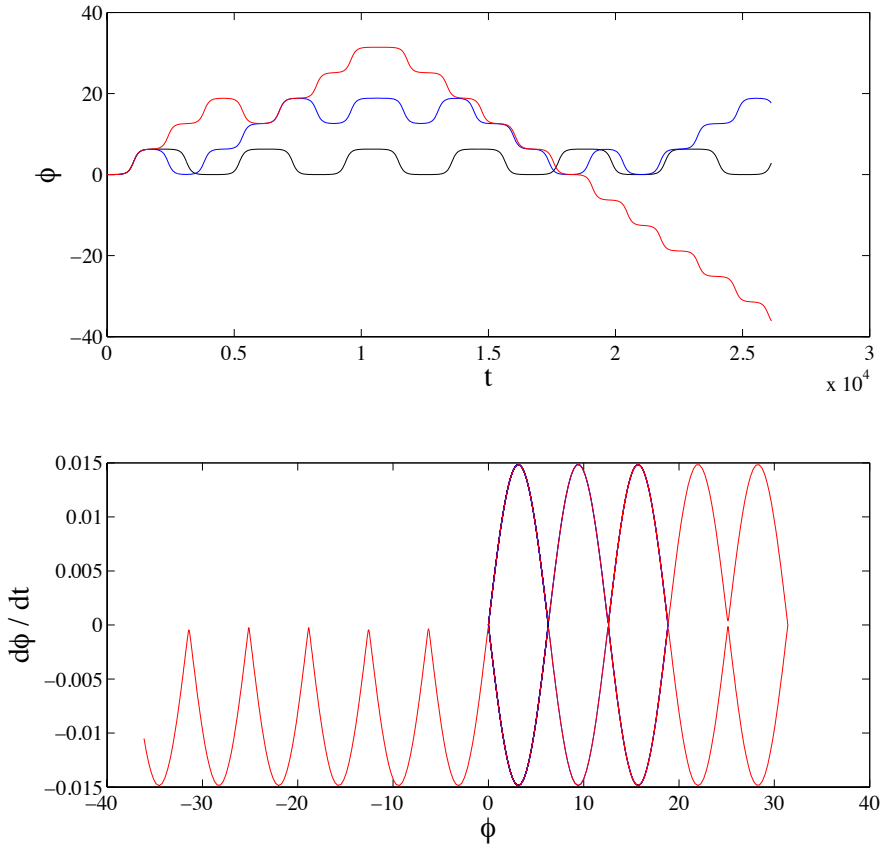

Figure 4.13: Nodding model: pendulum equation with and w/o small eccentricity forcing amplitudes. Solutions to the pendulum equation with constant eccentricity (black curve) and with eccentricity that varies by 0.1% on a secular timescale (blue and red curves). The system is set in a dynamically sensitive state near a separatrix with $\phi = 0.001$ and $\dot{\phi} = 0$ and integrated using 4^{th} order Runge-Kutta scheme for 16 full secular cycles. The eccentricity is initially small ($e = 0.001$), and the pendulum term has no knowledge of the inner body's eccentricity. The introduction of time varying eccentricity (even with small amplitude) induces circulation in the motion of the pendulum. The eccentricity cycle is phase shifted by π between the red and blue curves, where the blue curve begins at peak eccentricity. The bottom panel shows the phase trajectory for the resonance angle solutions in the top panel. The resonance angle is on phase trajectory that is very near a separatrix of the phase space. Note that in the phase diagram, the black curve is confined to $0 \lesssim \phi \lesssim 2\pi$, the blue curve is confined to $0 \lesssim \phi \lesssim 6\pi$, and the red curve is confined to $-12\pi \lesssim \phi \lesssim 10\pi$.

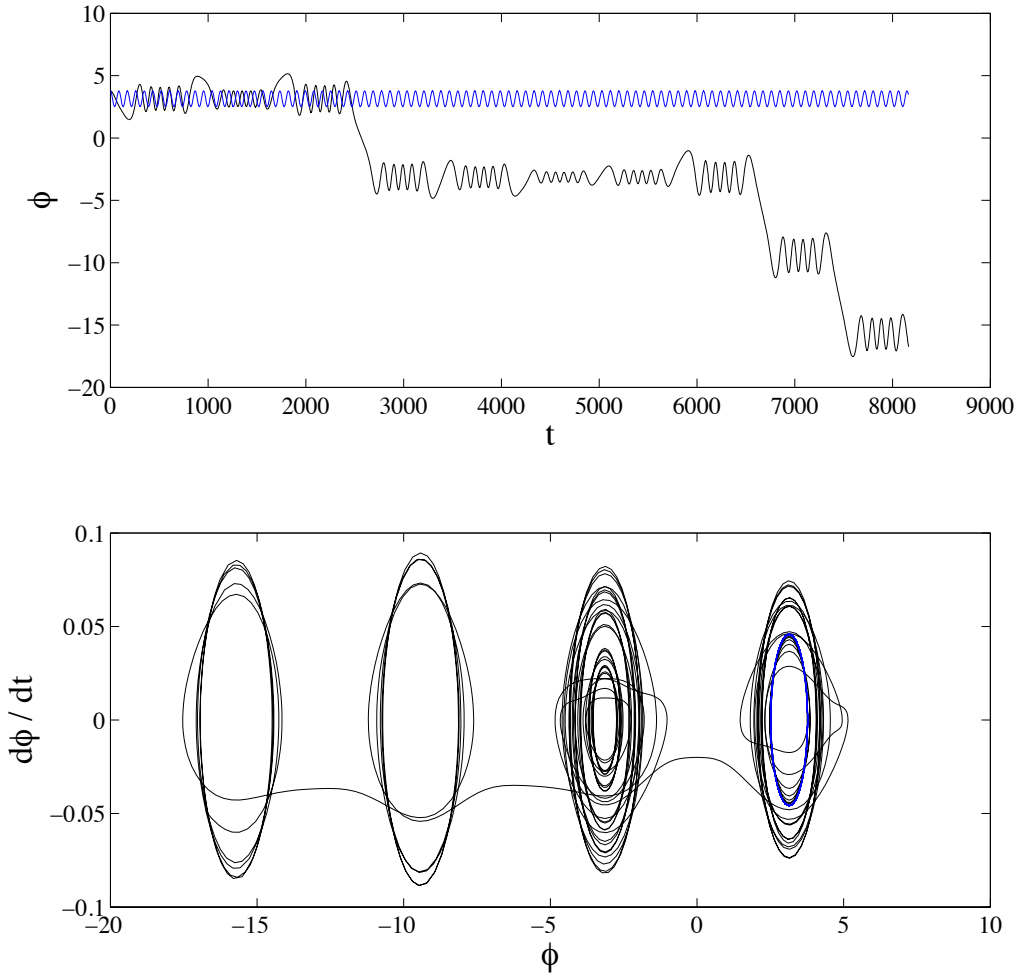

Figure 4.14: Nodding model: pendulum equation with and w/o large eccentricity forcing amplitudes. Solutions to the pendulum equation for initial values $e = 0.1$, $\phi = 1.2\ \pi$, and $\dot{\phi} = 0$. Both solutions presented here are for the pendulum term with (i) constant eccentricity (blue curve) and (ii) with eccentricity that varies by 99% on a secular timescale (black curve). When eccentricity is constant, the system remains in an oscillatory state with amplitude $\Delta\phi \approx \pi/4$ around the point$\phi \simeq \pi$. For time varying eccentricity, the librations of the resonance angle become unbound before 2 complete secular cycles, and nodding ensues. The bottom panel shows the phase trajectory for the resonance angle solutions in the top panel. Oscillations of the resonance angle occur around points that are equivalently located at $\phi = \pi$ (modulo 2π).

eccentricity is sufficiently low and the periastron circulates on secular timescales.

This model contains one deficiency. The inner separatrix of the external resonance problem is completely missing from this model along with the unique characteristics distinguishing the external resonance from the internal one. This separatrix originates because of a bifurcation that occurs for the external resonance when $e \sim 0.1$, and is responsible for asymmetric resonances that have been observed in simulations for that regime (e.g., Callegari et al., 2004; Lee, 2004). As a result, $\phi = \pi$ (or a point nearby) becomes a hyperbolic fixed point. Given that the test body's eccentricity must be sufficiently large before this bifurcation occurs may suggest that more terms of the disturbing function are required in the time averaged treatment to recover these dynamics. More work must be done in order to elucidate this issue.

4.5 Conclusion

This Chapter presents an investigation of nodding behavior for planetary systems that are near mean motion resonance, with a focus on resonance angles corresponding to the 2:1 MMR. For systems that experience the nodding phenomenon, the resonance angle librates (oscillates) for several cycles, then circulates for one or more cycles, and then resumes its oscillatory motion (libration). The process repeats, so that even though the resonance angle is primarily in oscillation, the phase of the resonance angle nonetheless accumulates over time. In the extreme version of this behavior, the resonance angle can oscillate for one cycle, circulate for the next cycle, and then repeat the process; the resonance angle moves continually back and forth between the two types of motion, so that the resonance angle has an effective period of oscillation that is ~ 2 times longer than the usual period for MMR (see Figures 4.3, 4.8, and 4.9).

Nodding can be described as complex motion near a separatrix in the phase space of the resonance angle. Both internal and external resonances can exhibit nodding, but there exist prominent qualitative differences in the nodding signatures between the two configurations. The phase space for internal resonances contain one separatrix, whereas the phase space for external resonances can contain two distinct separatrices. The qualitative differences are mainly due to the existence of asymmetric external resonances, which arise when the orbital eccentricity for the outer (smaller) body becomes sufficiently large. Circulation of the resonance angle over secular times is common when the planet's orbital eccentricity is sufficiently large, i.e., $e_p \gtrsim 0.02$.

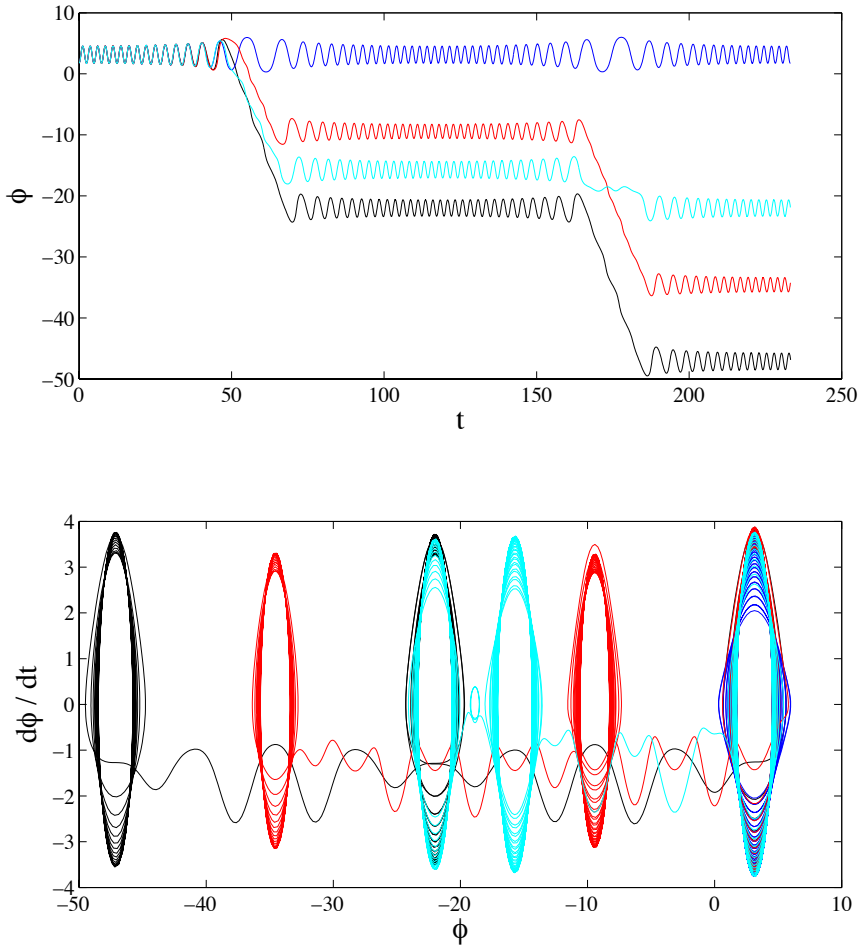

Figure 4.15: Nodding models: including additional lower order terms recovered in equation (4.28). The result of numerically integrating equation (4.40) using parameters $T_{orb} = 100$ days, $T_{sec} = T_{orb} \times 10^{2.94}$, $\mu = 10^{-3}$, $e_0 = 0.32$, $e_a = 0.28$, $\mathcal{F}_{\rm I} = 1$, and the orbiting bodies in a perfect 2:1 orbital period ratio. The blue curve shows the solution for the pendulum term alone; the black curve shows the solution for the pendulum term plus the term that goes like $\dot{\phi}$; the cyan curve includes the pendulum term and the $e^{-2}\cos\phi$ term; the red curve shows the solution when including all terms in equation (4.40). The only model out of the four depicted here that doesn't exhibit nodding is that consisting of the pendulum term in isolation. Inclusion of the two terms of lower eccentricity order and in any combination results in nodding. The timescale depicted in the top panel is in years. The bottom panel shows the phase trajectory for the resonance angle solutions in the top panel.

Exoplanets that transit their host stars are expected to exhibit transit timing variations when additional perturbing bodies are present, and the variations are greatest when the perturbing body is either in or near mean motion resonance with the transiting body. For systems where the perturbing body is near MMR, there is a possibility that the resonance angle may undergo nodding. In such systems, both the amplitude and the period of the TTVs depend on the window of time over which the system is observed (see Figures 4.8 and 4.9). If the observations are made over a time interval where the resonance angle of the system oscillates for many cycles, the TTVs have their usual interpretation. In the limit where the resonance angle goes back and forth between oscillating and circulating every cycle, the effective frequency of the TTVs is lower (than in the purely oscillatory case) by a factor of ~ 2. Nodding behavior that is intermediate between these two cases is also possible, and produces TTVs with intermediate frequencies (see the power spectra in the bottom panels of Figures 4.8 and 4.9). Note that the amplitudes of the TTVs vary with the mode of nodding/oscillation (for the same masses). The added complexity in the dynamics due to nodding can thus introduce corresponding difficulties in interpreting the source of transit timing variations. This possible complexity should be kept in mind when searching for hidden exoplanets through measurements of transit times.

Using Lagrange's planetary equations of motion, we have derived a set of generalized equations of motion for the resonance angle by including additional terms in the expansion in order to account for nodding behavior (see Section 4.4). This derivation uses the time-averaged disturbing function and initially keeps terms up to second order in eccentricity. As expected, the initial expansion includes a large number of terms. We then performed an analysis that uses results from the full numerical treatment to determine the relative sizes of the various terms in the expansion over the parameter space of interest (see Figures 4.10, 4.11, and 4.12). For some parameter values, we found that some of the "higher order" terms (those left out of the MD99 derivation) can dominate over those terms commonly used in deriving the pendulum model, which provides a standard description for MMR.

Given the expected magnitudes of the expansion terms, we have constructed a modified model for MMR, where the equation of motion includes two additional terms and thus allows for more complex dynamics (see equation [4.40]). This equation exhibits the nodding behavior found for interior resonances of the full problem. However, nodding only occurs for particular values of the eccentricity and argument of periastron, where both variables are considered as constants. We then generalized this model one step further by allowing the eccentricity to change with time (see

equation [4.41]), motivated by the secular cycles of eccentricity variation often seen in two planet systems (including the orbits of Jupiter and Saturn in our solar system – see MD99). With this generalization to include eccentricity cycles, nodding is a robust phenomenon and occurs for a wide range of the other parameters. Even when considering the pendulum term in isolation, the cycling of eccentricity on secular timescales can provide sufficient perturbations to induce nodding behaviors in certain dynamically vulnerable configurations.

The model from section 4.4 contains at least one deficiency. The inner separatrix of the external resonance problem is completely missing from the model, along with all of the unique characteristics distinguishing the external resonance from the internal one. This separatrix originates because of an effective bifurcation in the parameter space that occurs for the external resonance when $e \sim 0.1$, which is reminiscent of a pitchfork bifurcation (see Figure 4.7), and is responsible for asymmetric resonances that have been observed for that regime. As a result, some region in the neighborhood of $\phi = \pi$ contains a hyperbolic fixed point. Given that the eccentricity of the test body must be significantly large before this bifurcation occurs, additional terms in the expansion of the disturbing function may be required to recover these dynamics. This issue is left for future work.

The results of this work, and the existence of nodding phenomena in general, have two principal implications: [1] Planetary systems near MMR display complex and sometimes unexpected behavior, so that nodding poses a rich set of dynamical questions for further work. It would be interesting to determine the minimal requirements for a dynamical system to exhibit nodding, and to explore the relationship between nodding and chaotic motion. [2] The main application of this work to observations lies in the interpretation of transit timing variations. If an observed system with TTVs experiences nodding, then the inferred mass and orbital elements of the unseen perturbing body could vary, depending on the time interval of observation (Figures 4.8 and 4.9). A more complete exploration of parameter space, with a focus on the TTV signals (analogous to Veras et al. 2011), should be undertaken in the future.

CHAPTER V

Conclusions

Motivated by the ever-growing database of extrasolar planets, this thesis considers a range of dynamical problems associated with multiple planet systems. More specifically, this work focuses on how planetary systems enter into mean motion resonance, which represents a special dynamical state of the system. The thesis then considers how planetary systems can be removed from such resonant states and how loss of resonance leads to planetary collisions. Finally, this thesis presents a new dynamical effect, called nodding, wherein planetary systems move in and out of purely resonant configurations; this effect can have an interesting observational signature which affects the interpretation of ongoing measurements of Transit Timing Variations. In this final Chapter, we review the aforementioned results is greater detail, and then discuss possible avenues for future work.

5.1 Capture and Maintenance of Mean Motion Resonances

Chapter II of this thesis studies the entry of planetary systems into mean motion resonance by convergent migration (driven by a circumstellar disk), and the subsequent survival of the resonant configurations. Previous work has shown that the distributions of orbital elements (eccentricity and semimajor axis) for observed extrasolar planets can be reproduced by migration models with multiple planets. However, these results depend on resonance locking, and this thesis shows that entry into – and maintenance of – mean motion resonance depends sensitively on migration rate, eccentricity damping, and turbulence.

Overall, the MMR capture rates can be summarized in terms of the problem's four basic timescales: the migration timescale τ_a, the eccentricity damping timescale τ_e, the timescale τ_T for turbulence to act, and timescale of resonant librations τ_R. The system's dynamics are largely determined by the ordering of these timescales.

As shown by numerical integrations (Section 2.3), model equations (Section 2.4), and previous work (Quillen, 2006), planetary systems have difficulty entering and maintaining MMR when $\tau_a < \tau_R$. For instance, the three most common resonances considered were 2:1, 5:3, and 3:2, in increasing order of frequency (decreasing order of resonant libration timescale τ_R). As the migration rate increases, it becomes more likely for planets to migrate through the 2:1 resonance and approach the 5:3 resonance (perhaps capturing into resonance there). For faster migration yet, systems will continue to migrate through the nominal 5:3 resonance location, and approach the 3:2 resonance, possibly entering into resonance there. This basic trend is shown in Figures 2.3 – 2.8, and continues to hold up even in the presence of additional processes like eccentricity damping and turbulent forcing.

Eccentricity damping increases the likelihood of resonant survival provided that $\tau_e < \tau_a$. In general, planets are captured into resonant configurations more often in systems with larger eccentricity damping rates (see Figure 2.5). The probability of resonant capture can approach unity in radiative disk models, where the eccentricity damping parameter attains values of $K \geqslant 100$ (e.g., Bitsch & Kley, 2010). The overall effect of eccentricity damping thus is to promote mean motion resonance capture, in agreement with expectations (see Lecoanet et al. (2009)).

Turbulence acts to destroy resonances when $\tau_T < \tau_a$, which is in agreement with previous studies (Adams et al., 2008; Lecoanet et al., 2009; Rein & Papaloizou, 2009). The timescale for turbulence to act is

$$\tau_T \approx 3 \times 10^4 \text{ yr } \left[\frac{(\Delta J)_k / J_{orb}}{10^{-4}} \right]^{-2} , \tag{5.1}$$

where amplitudes of turbulent fluctuations used in this study are $0 \leqslant (\Delta J)_k / J_{orb} \leqslant 10^{-4}$. Figures 2.6 and 2.7 show that turbulence compromises MMR for slower migration rates, $\tau_a = -a/\dot{a} > 10^5$ yr.

Challenges remain in applying the results of this work to applications of extrasolar planets. As one issue of complication, many systems are expected to have comparable timescales so that $\tau_a \sim \tau_e \sim \tau_T$. Resonant libration times τ_R are often much shorter than all three of these timescales, so MMR is generally compromised by a combination of too rapid migration, too little eccentricity damping, and periods of turbulence that are too lengthy. Secondly, these systems display sensitive dependence on their initial conditions (e.g., Figure 2.13), so that systems in essentially the same regime of parameter space can result in vastly different outcomes. These differences are important, because migrating planets that maintain resonance stand a much greater

chance of survival (see Figures 2.9 and 2.10). Finally, the removal of disk material from the system does not signal the end of a planetary system's evolution. The planet-disk torques that lead to migration, eccentricity damping, and turbulent forcing will vanish forever with the gaseous disk. However, the system will continue to evolve through gravitational forces with the surviving members of the planetary system. Planets that are deep in mean motion resonance are expected to survive over long spans of time; on the other hand, systems that are near — but not in — resonance will often be disrupted over these longer time scales (e.g., Holman & Wiegert, 1999; David et al., 2003).

5.2 Collisions

The observed population of Hot Jupiters displays a wide variety of physical properties, including a wide range of densities and core sizes for a given planetary mass. Motivated by these observations, Chapter III studies one possible channel for increasing the core mass and metallicity of a Hot Jupiter. This scenario begins after the Hot Jupiter has become parked in a ~ 4 day orbit. Later, rocky planets form farther out in the remaining circumstellar disk and then migrate inward. The possible end states for the rocky planet are *(i)* collisions with the Jovian planet, *(ii)* accretion onto the star, *(iii)* ejection from the system, or *(iv)* long-term survival.

The simulations conducted in this thesis show that the probabilities associated with each end state depend on the Hot Jupiter's mass m_{hj}, initial orbital eccentricity e_{hj}, and the outer planet's eccentricity damping rate K. In general, planetary collisions are common when the eccentricity damping rate is sufficiently low, but are rare otherwise. In approximate terms, collisions require the eccentricity damping parameter $K \leqslant K_C \approx 10$, where the threshold K_C depends on the initial orbital eccentricity and mass of the Jovian planet (Figures 3.2, 3.3). For a given circumstellar disk, the K value depends upon its structure, viscosity, and the mass of the migrating rocky planet. Previous studies of planet-disk interactions generally find K values of order unity for migrating planets that clear gaps (Kley et al., 2004), but $K \approx 10 - 30$ for smaller embedded planets (Artymowicz, 1993). The outcomes thus depends upon the degree to which the migrating planet clears a gap. For low-viscosity disks, planets clear gaps when their Hill sphere exceeds the disk scale height, $r_H > H$ (Crida et al., 2008; Papaloizou & Terquem, 2006), which requires $m_P \gtrsim 27 M_\oplus$ for the disk parameters used in these simulations. However, a relatively large rocky planet ($m_P \gtrsim 10 - 20 M_\oplus$) can clear a partial-gap, which in turn can reduce the K below the

threshold K_C, and thus increase the chance for collisions. On the other hand, smaller planets with $m_P \lesssim 10 M_\oplus$ are expected to have $K \gtrsim K_C$ and readily avoid collision.

These results outline a region of parameter space where rocky planet collisions with Hot Jupiters is a viable outcome. The question of interest becomes "How do these collisions affect the physical characteristics of the Hot Jupiter?" While a collision here almost certainly increases the total metallicity of the Hot Jupiter, detailed planetary structure calculations (beyond the scope of this work) are required to determine where mass/energy is deposited as well as the long-term transfer of heat/energy out of the planetary body. Previous studies containing such detailed planetary structure models shows that incoming rocky planets with $m_P \gtrsim 1 - 10 M_\oplus$ remain sufficiently intact, and penetrate deep enough into a Jovian planet to increase its core mass (Anic et al., 2007). This result has been verified by subsequent calculations (Anderson & Adams, 2012), which also determine the expected cross sections for planetary capture in this dynamical regime. Thus, both the occurrence of collisions and subsequent survival to reach the core require $m_P \gtrsim 10 M_\oplus$. In addition to increasing the metallicity and (potentially) the core mass, the Hot Jupiter's energy budget will also be affected. Using an expected collision velocity $v \sim 60$ km/s (determined from Figure 3.4) and some back of the envelope calculations, a single collision accounts for $\sim 5 - 10\%$ of the binding energy of a Hot Jupiter. This energy, if deposited at optically thick depths of the Hot Jupiter, is large enough to help inflate the planetary radius (Bodenheimer et al., 2003; Batygin & Stevenson, 2010). On the other hand, if the energy is deposited into the optically thin upper atmosphere of the planet, it quickly radiates away and cannot inflate the radius. Although changes in planetary structure due to the collisions considered in this work should be determined more rigorously, the results show that larger rocky planets have a greater potential influence (per unit mass) on the structure of a Hot Jupiter than smaller ones. Recent calculations also show that Hot Jupiters are expected to behave differently than older, colder Jovian planets like those in our Solar System. Due to both stellar irradiation and internal energy sources, Hot Jupiters have larger radii, for a given mass, than planets in the outer solar system. This increase in radius, and the corresponding decrease in density, allow colliding rocky planets to survive tidal disruption as they plummet to the planetary core.

5.3 Observational Dynamical Signatures

As planetary systems move in and out of mean motion resonance, they can produce an interesting observational signature. Chapter IV contains an investigation of nodding behavior for planetary systems near the 2:1 mean motion resonance. For systems that experience the nodding phenomenon, the resonance angle undergoes a repeating process of libration (oscillation) for several cycles, then circulation for one or more cycles. Although the resonance angle is primarily in oscillation, due to the intermittent bouts of circulation, its phase may accumulate significantly over time. In an extreme version of this behavior, the resonance angle can oscillate for one cycle, circulate for the next cycle, and then repeat the process; the resonance angle moves continually back and forth between the two types of motion, so that its effective period of oscillation is ~ 2 times longer than the usual period for MMR (see Figures 4.3, 4.8, and 4.9).

The complicated motions exhibited by a nodding resonance angle arises due to cyclic separatrix crossings in phase space. Both internal and external resonances may experience nodding. However, the nodding signatures for the two configurations display prominent qualitative differences. These differences are mainly due to the existence of asymmetric external resonances, which arise when the orbital eccentricity for the outer (smaller) body becomes sufficiently large. Because of this asymmetry for external resonances, its phase space includes two distinct separatrices. In contrast, the phase space for internal resonances includes one separatrix, and resembles the phase space of a simple pendulum. Circulation of the resonance angle over secular times is common when the planet's orbital eccentricity is sufficiently large, i.e., $e_p \gtrsim 0.02$, thus separatrix crossings occur once per secular cycle (i.e. during epochs of orbital apses alignment).

Exoplanets that transit their host stars exhibit transit timing variations (TTV) when additional perturbing bodies are present, where (near) resonant configurations portray enhanced TTV amplitudes (Agol et al., 2005). Systems near MMR may undergo nodding, in which case the TTV's amplitude and the period can be affected (see Figures 4.8 and 4.9). If transit observations are made during a time that the resonance angle strictly oscillates, then the TTVs have their usual interpretation. In the limit that the resonance angle circulates every other cycle, the TTV's effective frequency is lower (than in the purely oscillatory case) by a factor of ~ 2. Intermediate frequencies are attainable as well given the appropriate nodding cycle (see the power spectra in the bottom panels of Figures 4.8 and 4.9). Nodding thus adds complexity

to the dynamics which introduces corresponding difficulties in interpreting the source of transit timing variations, and should be kept in mind when searching through measurements of transit times for otherwise undetectable exoplanets. For instance, if an observed system with TTVs experiences nodding, then the inferred mass and orbital elements of the unseen perturbing body could vary, depending on the time interval of observation. A more complete exploration of parameter space, with a focus on the TTV signals (analogous to Veras et al. 2011), should be undertaken in the future to resolve such complications.

In an attempt to sufficiently model this nodding behavior, I derived a set of generalized equations of motion for the resonance angle using the time-averaged disturbing function and considering terms up to second order in eccentricity. The relative sizes of the various terms in this expansion were determined using results from the full numerical treatment (see Figures 4.10, 4.11, and 4.12) where, in some instances, higher order terms dominate over those used in the standard description for MMR (Murray & Dermott, 1999). This treatment resulted in a modified model for MMR that allows for more complex dynamics (see equation [4.40]). This equation, in combination with a prescription for time varying eccentricities, exhibits the nodding behavior found for interior resonances of the full problem. Moreover, even when considering the standard prescription for MMR, the cycling of eccentricity on secular timescales can provide sufficient perturbations to induce nodding behaviors in certain dynamically vulnerable configurations.

Although the model is somewhat successful in that it exhibits nodding behaviors for the expected orbital parameters, it fails to replicate certain phase space structures. Specifically, the inner separatrix of the external resonance problem, along with all of the characteristics distinguishing it from the internal one, is completely missing from the model. The missing separatrix is responsible for asymmetric resonances, and arises due to an effective dynamical bifurcation when the outer eccentricity $e \gtrsim 0.1$. Given that the eccentricity of the test body must be significantly large before this bifurcation occurs, additional terms in the expansion of the disturbing function may be required to recover these dynamics. Planetary systems near MMR display complex and sometimes unexpected behavior, so that nodding poses a rich set of dynamical questions for further work. It would be interesting to determine the minimal requirements for a dynamical system to exhibit nodding, and to explore the relationship between nodding and chaotic motion.

5.4 Future Directions

Although this thesis has addressed a number of dynamical issues related to planetary systems, the dynamics of these entities is incredibly rich, and much more work remains.

[1] One basic issue is the question of the probability of planetary systems being in a state of mean motion resonance purely by chance. We have addressed this issue with preliminary work, which suggests the following: If a two planet system is constructed with the orbits in exactly a 2:1 period ratio, but with all of the other orbital elements chosen at random, the probability of the system staying in a resonant state is of order 10 percent. This estimate is uncertain for a number of reasons, including dependencies upon the planetary mass ratio, the Hill radius of the larger planet, the particular mode of 2:1 resonance considered, and many other complicating issues.

[2] The internal structure of planets is extremely diverse, and affects the dynamics in a variety of ways. If one constructs a star, basically by putting about one solar mass of gas into a sphere, then the subsequent structure and evolution of that object is largely the same for all stars. Metallicity affects the evolution, but only modestly. In contrast, exoplanets are observed to have an enormous range of radii for a given mass (e.g., Laughlin et al., 2011). This diversity is driven by composition (e.g., how much rock the planet contains), environment (e.g., how much radiation is intercepted by the star), and by additional power sources (e.g., ohmic dissipation and tidal heating). These latter two effects, in turn, depend sensitively on the physical structure of the planet. As a result, one important avenue for future research is to couple the dynamics to the planetary structure.

[3] We have explored nodding and shown that it affects TTVs. With the success of the Kepler mission, a great deal of attention is being given to planet transits. As a result, theoretical studies involving transits and transit timing variations will be rich and fruitful in the immediate future (Deck et al., 2012; Beaugé & Nesvorný, 2013). In order to take advantage of the current and upcoming data, more in-depth phenomenological study should be carried out. One such need for further dynamical understanding of transiting planetary systems can be summarized as follows: Observations show that a substantial fraction of planet pairs in multiple planet systems are close to, but not exactly in, mean motion resonance (MMR), with the most common period ratio found being the 2:1 (Lithwick & Wu, 2012; Batygin & Morbidelli, 2013). Further, the systems that are most easily observed via transit timing variations are those that are in, or near, mean motion resonance. The existence of the nodding phe-

nomena (described above) has important implications in this context. For example, in actively nodding planetary systems, both the amplitude and frequency of transit timing variations depend on the observational time window. The presence of nodding will thus affect the inferred properties of planets discovered via transit timing variations. As a result, a full understanding of nodding is necessary to characterize systems exhibiting transit timing variations.

APPENDICES

APPENDIX A

RV Analysis

Consider the orbital angular momentum per unit mass for a two body system is $h = rv$, where r is the radial coordinate, and v the velocity of the reduced mass particle. Only the perpendicular component of the orbital angular momentum vector will yield doppler shifts in spectroscopic measurements of the star, $h \sin i$. The stellar velocity is related to the reduced mass' velocity by $v_* = m/(M_* + m)v$. For Keplerian systems, we have expressions for the orbital angular momentum, $h = na^2\sqrt{1-e^2}$, the mean motion $n = 2\pi/T$, semi-major axis $a = (n^{-2}\mu)^{1/3}$, and the radial coordinate $r = a(1-e^2)F(t)$. Here, T is the orbital period, $\mu = \mathcal{G}(M_* + m)$, e is eccentricity, and $F(t)$ is a period function of time ($F(0) = F(T)$) dependent upon eccentricity e, longitude of periapse ω, and the true longitude f of the planet (see Figure A.1). Combining these expressions gives the relationship between the star's line-of-sight velocity and these important orbital parameters,

$$v_{perp}(t) = \left(\frac{2\pi\mathcal{G}}{T}\right)^{1/3} (1-e^2)^{-1/2} \frac{m \sin i}{(M_* + m)^{2/3}} F(t) \ .$$

The period T is taken directly from the periodicity of the signal itself. The eccentricity e and longitude of periapse ω is found from a Keplerian fit of the time dependent part $F(t) \equiv \cos(f + \varpi) + e\cos(\varpi)$ (see Figure A.1). Finally, the stellar mass is inferred from spectroscopic measurements of the star. However, the inclination angle i and the line of the ascending node Ω escape measurement. Because the orbit inclination escapes measurement, the planet's *minimum mass*, $m \sin i$, is measured. ‘

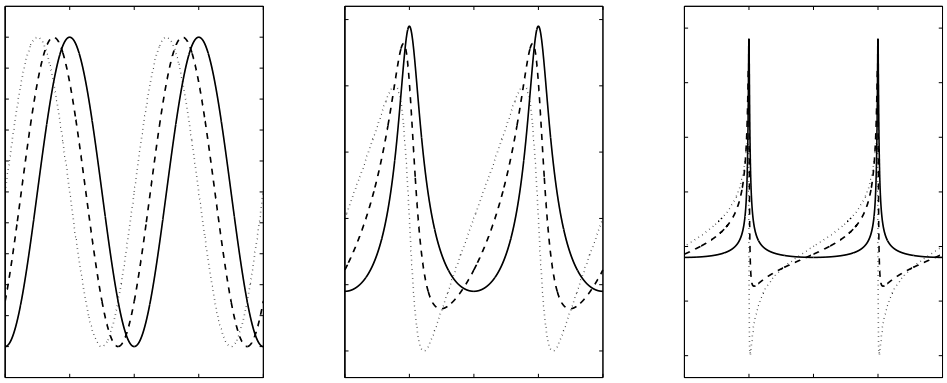

Figure A.1: Keplerian (2-body) RV curves for various eccentricities e and longitude of periapse ω. Amplitudes are normalized to unity. In each panel, $\omega = 0$, 45, and 90 depicted by the solid, dashed, and dotted curves respectively. *Left: RV signal for circular orbits,* $e = 0$. *Middle:* $e = 0.4$. *Right:* $e = 0.8$.

APPENDIX B

Transit Time Analysis

At the moment the planet begins its ingress eclipse (at location 1 in Figure B.1), the center to center line makes an angle α with the vertical, given by

$$\tan^2 \alpha = \frac{(1-k^2)\cos^2 i}{k^2 - \cos^2 i} \ , \tag{B.1}$$

where $k \equiv (R_* + R_p)/a$, a is the orbit radius, and i is angle between the line of sight and the orbital plane's normal. In the plane of the orbit, the total angle of the orbit subtended by the star's disk θ is given by $\sin\theta/2 = X_T/a$, or

$$\theta = 2\sin^{-1}\left(\frac{k^2 - \cos^2 i}{\sin^2 i}\right)^{1/2} \ . \tag{B.2}$$

Since the orbit is circular, the planet's angular velocity at any point along the orbit equals its mean motion n, and so the planet traverses the angle θ in a time $t_c = \theta/n$, otherwise known as the *transit time*. The transit time is the expected duration of reduced stellar luminosity per orbit, i.e. the time it takes the planet to move from point 1 to point 4 in Figure B.1. Written in terms of the orbital period T, the transit time is

$$t_c = \frac{T}{\pi}\sin^{-1}\left(\frac{k^2 - \cos^2 i}{\sin^2 i}\right)^{1/2} \ . \tag{B.3}$$

Note that the factor k inside the arcsine argument contains the orbit radius, and hence the orbital period, so in this simple, idealized picture, full transit depth is achieved when the planet's boundary is located fully within the boundary of the stellar disk, and thus blocks out the maximum amount of starlight. Transit time at full depth is

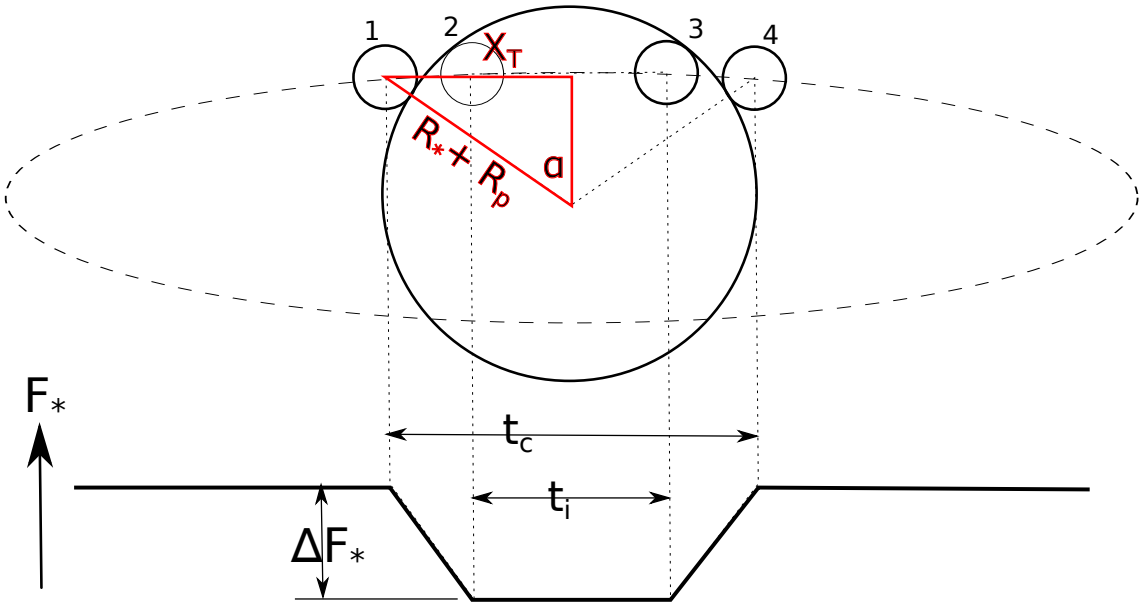

Figure B.1: A simplified diagram depicting the geometry of a planet's ingress and egress eclipse during a stellar transit and the schematic representation of the stellar luminosity decrement during the transit event. The star and planet are assumed to be spherical and the two bodies orbit the common center of mass in circular orbits. The dashed ellipse represents the circular orbit of the planet around the star projected into the plane of the sky. Below is a schematic representation of the stellar luminosity received at different moments during the transit. The transit depth ΔF_* is on the order of 0.1 - 1% during planetary transit.

given by

$$t_i = \frac{T}{\pi} \sin^{-1} \left(\frac{k_2^2 - \cos^2 i}{\sin^2 i} \right)^{1/2} , \tag{B.4}$$

where $k_2 = (R* - R_p)/a$. Requiring the times given by t_c and t_i to be real immediately sets the constraint that $a \cos i \leqslant R_* + R_p$ in order for a planet to transit its host star, and $a \cos i \leqslant R_* - R_p$ in order for the transit to reach its full depth in luminosity decrement.

APPENDIX C

Phase Space Analysis

This Appendix discusses the phase plane for the model equations developed in Section 2.4. This analysis determines the number of allowed regions in phase space, and hence places constraints on the allowed dynamics. Given the equations of motion (2.30) and (2.31), the basic equation for curves in phase space has the form

$$\frac{dp}{d\phi} = -\frac{\sin\phi}{4p^2 + 2b - (\cos\phi)/p}\,. \tag{C.1}$$

If we consider the parameter b to be fixed, this equation can be integrated directly to find an implicit solution of the form

$$p\cos\phi = \left(p^4 - p_0^4\right) + b\left(p^2 - p_0^2\right) + p_0\,, \tag{C.2}$$

where $p_0 = p(\phi = 0)$, by definition. This equation can be written in the alternate form

$$p^4 + bp^2 - p\cos\phi = E \qquad \text{where} \qquad E \equiv p_0^4 + bp_0^2 - p_0 = constant\,. \tag{C.3}$$

In the limit of large $p \gg 1$, we can ignore the cosine term in the denominator of equation (C.1) and find the approximate solution

$$\frac{4}{3}\left(p^3 - p_0^3\right) + 2b(p - p_0) = \cos\phi - 1\,. \tag{C.4}$$

This result can be rewritten in the form

$$-\sin^2(\phi/2) = (p - p_0)\left\{\frac{2}{3}\left[p^2 + pp_0 + p_0^2\right] + b\right\} \approx (p - p_0)\left\{2p_0^2 + b\right\}\,. \tag{C.5}$$

Note that in the limit of large p, $|p - p_0| \ll p$, and the two expressions in the above equation are the same to leading order in the parameter $|p - p_0|/p$.

In the limit of small $p \ll 1$, we can ignore the p^2 term in equation (C.1) and find the solution

$$p \cos\phi = b\left(p^2 - p_0^2\right) + p_0 \,. \tag{C.6}$$

For sufficiently small p, this expression reduces to the simpler form

$$p \cos\phi = p_0 \,. \tag{C.7}$$

The solution for the phase space curves, given by equation (C.3), can allow for multiple roots. We first note that the parameters b, E, and $\cos\phi$ can all be both positive and negative. As a result, the number of roots for p will vary.

Case I: $b > 0$, $E > 0$: In this case, only one root for p exists for all values of the angle ϕ (or $\cos\phi$). For small values of the energy E, the solutions for p get small for negative values of $\cos\phi$.

Case II: $b < 0$, $E > 0$: For $\cos\phi > 0$, only one solution for p exists. For $\cos\phi < 0$, however, there can be multiple roots provided that $|b|$ is large enough and the energy E is small enough. The conditions required for multiple roots is that

$$|b| > \frac{8}{27}\cos^2\phi \qquad \text{and} \qquad 4|b|E < \cos^2\phi \,. \tag{C.8}$$

In the regime where the "extra" roots arise, $p \ll 1$, and the solutions reduce to the approximate form

$$p = \frac{\cos\phi \pm \left[\cos^2\phi - 4|b|E\right]^{1/2}}{2|b|} \,. \tag{C.9}$$

Case III: $b > 0$, $E < 0$: There are no solutions for $\cos\phi < 0$. For the case $\cos\phi > 0$, there are either two solutions for small E, or no solutions.

Case IV: $b < 0$, $E < 0$: For $\cos\phi > 0$, there are two solutions for small E and no solutions if E is too large and negative. For the case $\cos\phi < 0$, the two solutions disappear if $|b|$ is too small, where the critical value (for the limiting case $\cos\phi = -1$) is given by

$$|b|_c = \frac{3}{4^{1/3}} \approx 1.587 \,. \tag{C.10}$$

For cases of interest, the parameter b becomes large and negative. For bound states, the energy also becomes large and negative. In this regime, the phase curves become

almost independent of angle ϕ, with

$$p^2 \approx \frac{|b| \pm \left[b^2 + 4E\right]^{1/2}}{2} \,. \tag{C.11}$$

Figure C.1 shows one sample phase plot for the case where $b = 0$, which corresponds to systems that are passing through the resonant condition. For this case, as the energy variable E decreases from positive to negative values, the phase curves change their shape: For positive E, solutions for the momentum variable p exist for all values of the angle ϕ; for negative E, solutions for p exist for a limited range of angles. These isolated regions, which become narrower as the energy E grows more negative, correspond to oscillatory solutions in ϕ (such as that shown in Figure 2.11).

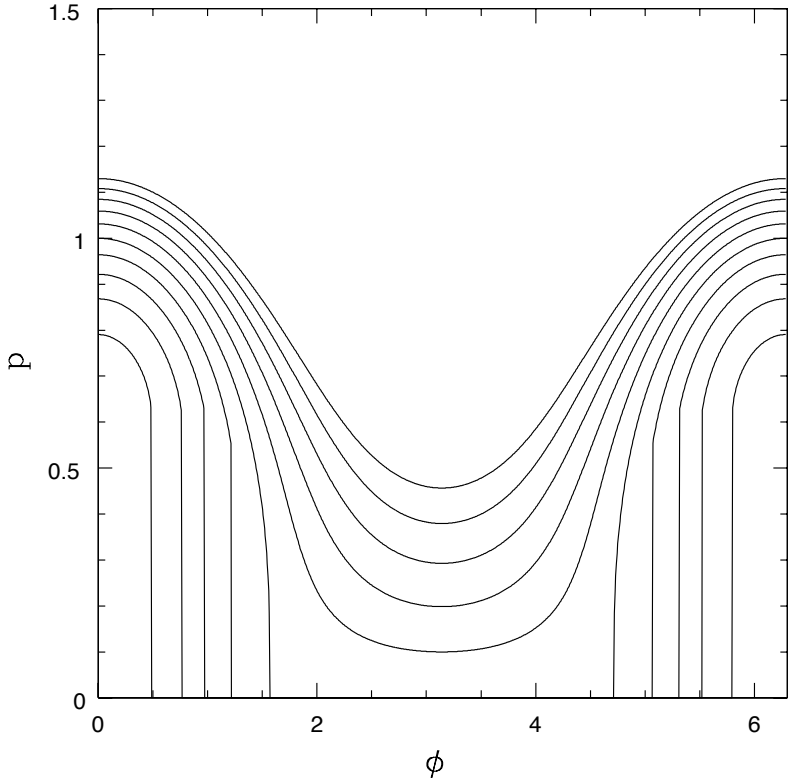

Figure C.1: Phase plot for the case $b = 0$ where systems can enter resonance. The various curves show decreasing values of energy from $E = 0.5$ (top) down to $E = -0.4$ (bottom). Note that as E falls below zero, solutions for p do not exist for negative values of $\cos\phi$.

BIBLIOGRAPHY

BIBLIOGRAPHY

Abramowitz, M., & Stegun, I. A. 1965, Handbook of mathematical functions with formulas, graphs, and mathematical tables (Dover Books on Advanced Mathematics, New York: Dover, —c1965, Corrected edition, edited by Abramowitz, Milton; Stegun, Irene A.)

Acheson, D. J. 1995, Proceedings: Mathematical and Physical Sciences, 448, pp. 89

Adams, F. C. 2010, ARA&A, 48, 47

Adams, F. C., Cai, M. J., & Lizano, S. 2009, ApJ, 702, L182

Adams, F. C., Hollenbach, D., Laughlin, G., & Gorti, U. 2004, ApJ, 611, 360

Adams, F. C., Lada, C. J., & Shu, F. H. 1987, ApJ, 312, 788

Adams, F. C., & Laughlin, G. 2003, Icarus, 163, 290

Adams, F. C., Laughlin, G., & Bloch, A. M. 2008, ApJ, 683, 1117

Adams, F. C., Ruden, S. P., & Shu, F. H. 1989, ApJ, 347, 959

Adams, F. C., & Shu, F. H. 1986, ApJ, 308, 836

Agol, E., Steffen, J., Sari, R., & Clarkson, W. 2005, MNRAS, 359, 567

Anderson, K. R., & Adams, F. C. 2012, PASP, 124, 809

Anic, A., Alibert, Y., & Benz, W. 2007, A&A, 466, 717

Armitage, P. J. 2000, A&A, 362, 968

Artymowicz, P. 1993, ApJ, 419, 166

Balbus, S. A., & Hawley, J. F. 1991, ApJ, 376, 214

Baruteau, C., & Masset, F. 2008, ApJ, 672, 1054

Batygin, K., & Morbidelli, A. 2011, Celestial Mechanics and Dynamical Astronomy, 111, 219

—. 2013, AJ, 145, 1

Batygin, K., & Stevenson, D. J. 2010, ApJ, 714, L238

Beaugé, C., & Nesvorný, D. 2013, ApJ, 763, 12

Bitsch, B., & Kley, W. 2010, A&A, 523, A30

Bodenheimer, P., Laughlin, G., & Lin, D. N. C. 2003, ApJ, 592, 555

Bodenheimer, P., & Pollack, J. B. 1986, Icarus, 67, 391

Boss, A. P. 1997, Science, 276, 1836

—. 1998, ApJ, 503, 923

Brouwer, D., & Clemence, G. M. 1961, Methods of celestial mechanics (New York: Academic Press, 1961)

Callegari, Jr., N., Michtchenko, T. A., & Ferraz-Mello, S. 2004, Celestial Mechanics and Dynamical Astronomy, 89, 201

Carter, J. A., Agol, E., Chaplin, W. J., et al. 2012, Science, 337, 556

Chatterjee, S., Ford, E. B., Matsumura, S., & Rasio, F. A. 2008, ApJ, 686, 580

Chiang, E. I., & Goldreich, P. 1997, ApJ, 490, 368

Cochran, W. D., Fabrycky, D. C., Torres, G., et al. 2011, ApJS, 197, 7

Cresswell, P., & Nelson, R. P. 2008, A&A, 482, 677

Crida, A., Sándor, Z., & Kley, W. 2008, A&A, 483, 325

David, E.-M., Quintana, E. V., Fatuzzo, M., & Adams, F. C. 2003, PASP, 115, 825

Deck, K. M., Holman, M. J., Agol, E., et al. 2012, ApJ, 755, L21

Dumusque, X., Pepe, F., Lovis, C., et al. 2012, Nature, 491, 207

Durisen, R. H., Boss, A. P., Mayer, L., et al. 2007, Protostars and Planets V, 607

Fabrycky, D. C., & Winn, J. N. 2009, ApJ, 696, 1230

Fabrycky, D. C., Lissauer, J. J., Ragozzine, D., et al. 2012, ArXiv e-prints

Ferraz-Mello, S., Beaugé, C., & Michtchenko, T. A. 2003, Celestial Mechanics and Dynamical Astronomy, 87, 99

Ford, E. B., & Rasio, F. A. 2008, ApJ, 686, 621

Fortney, J. J., Saumon, D., Marley, M. S., Lodders, K., & Freedman, R. S. 2006, ApJ, 642, 495

Friedland, L. 2001, ApJ, 547, L75

Gammie, C. F., & Ostriker, E. C. 1996, ApJ, 466, 814

Goldreich, P., & Sari, R. 2003a, ApJ, 585, 1024

—. 2003b, ApJ, 585, 1024

Goldreich, P., & Tremaine, S. 1980, ApJ, 241, 425

Grillmair, C. J., Burrows, A., Charbonneau, D., et al. 2008, Nature, 456, 767

Guckenheimer, J., & Holmes, P. 1983, Nonlinear Oscillations, Dynamical Systems, and Bifurcations of Vector Fields, Applied Mathematical Sciences No. v. 42 (Springer-Verlag)

Hartmann, L. 2002, ApJ, 578, 914

Hartmann, L., & Kenyon, S. J. 1987, ApJ, 322, 393

Hatzes, A. P., Cochran, W. D., McArthur, B., et al. 2000, ApJ, 544, L145

Hayashi, C. 1981, Progress of Theoretical Physics Supplement, 70, 35

Hollenbach, D., Johnstone, D., Lizano, S., & Shu, F. 1994, ApJ, 428, 654

Holman, M. J., & Murray, N. W. 2005, Science, 307, 1288

Holman, M. J., & Wiegert, P. A. 1999, AJ, 117, 621

Holman, M. J., Fabrycky, D. C., Ragozzine, D., et al. 2010, Science, 330, 51

Howard, A. W., Johnson, J. A., Marcy, G. W., et al. 2011, ApJ, 726, 73

Ikoma, M., Guillot, T., Genda, H., Tanigawa, T., & Ida, S. 2006, ApJ, 650, 1150

Johnson, E. T., Goodman, J., & Menou, K. 2006, ApJ, 647, 1413

Kennedy, G. M., & Kenyon, S. J. 2008, ApJ, 673, 502

Kenyon, S. J. 2002, PASP, 114, 265

Kenyon, S. J., & Hartmann, L. 1987, ApJ, 323, 714

Ketchum, J. A., Adams, F. C., & Bloch, A. M. 2011a, ApJ, 741, L2

—. 2011b, ApJ, 726, 53

—. 2013, ApJ, 762, 71

Kley, W., Peitz, J., & Bryden, G. 2004, A&A, 414, 735

Knutson, H. A., Charbonneau, D., Allen, L. E., Burrows, A., & Megeath, S. T. 2008, ApJ, 673, 526

Koenigl, A. 1991, ApJ, 370, L39

Konacki, M., Torres, G., Jha, S., & Sasselov, D. D. 2003, Nature, 421, 507

Kuchner, M. J. 2004, ApJ, 612, 1147

Larson, R. B. 1985, MNRAS, 214, 379

Laughlin, G., & Adams, F. C. 1998, ApJ, 508, L171

Laughlin, G., Crismani, M., & Adams, F. C. 2011, ApJ, 729, L7+

Laughlin, G., Steinacker, A., & Adams, F. C. 2004, ApJ, 608, 489

Lecoanet, D., Adams, F. C., & Bloch, A. M. 2009, ApJ, 692, 659

Lee, M. H. 2004, ApJ, 611, 517

Lee, M. H., & Peale, S. J. 2002, ApJ, 567, 596

Levison, H. F., Morbidelli, A., & Dones, L. 2004, AJ, 128, 2553

Levison, H. F., Morbidelli, A., Tsiganis, K., Nesvorný, D., & Gomes, R. 2011, AJ, 142, 152

Lin, D. N. C., Bodenheimer, P., & Richardson, D. C. 1996, Nature, 380, 606

Lin, D. N. C., & Papaloizou, J. 1986, ApJ, 309, 846

Lithwick, Y., & Wu, Y. 2012, ApJ, 756, L11

Lubow, S. H., & Ida, S. 2011, Planet Migration, ed. S. Seager, 347–371

Mac Low, M.-M., & Klessen, R. S. 2004, Reviews of Modern Physics, 76, 125

Marcy, G. W., & Butler, R. P. 1996, ApJ, 464, L147+

—. 2000, PASP, 112, 137

Masset, F. S., & Casoli, J. 2009, ApJ, 703, 857

Masset, F. S., Morbidelli, A., Crida, A., & Ferreira, J. 2006, ApJ, 642, 478

Masset, F. S., & Papaloizou, J. C. B. 2003, ApJ, 588, 494

Matsumura, S., Thommes, E. W., Chatterjee, S., & Rasio, F. A. 2010, ApJ, 714, 194

Mayor, M., & Queloz, D. 1995, Nature, 378, 355

McKee, C. F. 1989, ApJ, 345, 782

McKee, C. F., & Ostriker, E. C. 2007, ARA&A, 45, 565

McKee, C. F., Zweibel, E. G., Goodman, A. A., & Heiles, C. 1993, in Protostars and Planets III, ed. E. H. Levy & J. I. Lunine, 327

Michtchenko, T. A., Beaugé, C., & Ferraz-Mello, S. 2008a, MNRAS, 387, 747

—. 2008b, MNRAS, 391, 215

Moorhead, A. V. 2008, PhD thesis, University of Michigan

Moorhead, A. V., & Adams, F. C. 2005, Icarus, 178, 517

—. 2008, Icarus, 193, 475

Morbidelli, A., Tsiganis, K., Crida, A., Levison, H. F., & Gomes, R. 2007, AJ, 134, 1790

Mordasini, C., Alibert, Y., & Benz, W. 2009, A&A, 501, 1139

Murray, C. D., & Dermott, S. F. 1999, Solar system dynamics (Cambridge University Press)

Nakano, T. 1998, ApJ, 494, 587

Nelson, R. P. 2005, A&A, 443, 1067

Nelson, R. P., & Papaloizou, J. C. B. 2002, MNRAS, 333, L26

—. 2004, MNRAS, 350, 849

Nesvorný, D., & Morbidelli, A. 2008, ApJ, 688, 636

Ogilvie, G. I., & Lubow, S. H. 2003, ApJ, 587, 398

Oishi, J. S., Mac Low, M.-M., & Menou, K. 2007, ApJ, 670, 805

Paardekooper, S.-J., Baruteau, C., Crida, A., & Kley, W. 2010, MNRAS, 401, 1950

Paardekooper, S.-J., & Papaloizou, J. C. B. 2008, A&A, 485, 877

Papaloizou, J. C. B., & Larwood, J. D. 2000, MNRAS, 315, 823

Papaloizou, J. C. B., Nelson, R. P., Kley, W., Masset, F. S., & Artymowicz, P. 2007, Protostars and Planets V, 655

Papaloizou, J. C. B., & Terquem, C. 2006, Reports on Progress in Physics, 69, 119

Pepe, F., Lovis, C., Ségransan, D., et al. 2011, A&A, 534, A58

Perna, R., Menou, K., & Rauscher, E. 2010, ApJ, 724, 313

Perryman, M. A. C. 2000, Reports on Progress in Physics, 63, 1209

Pollack, J. B., Hubickyj, O., Bodenheimer, P., et al. 1996, Icarus, 124, 62

Press, W. H., Teukolsky, S. A., Vetterling, W. T., & Flannery, B. P. 1992, Numerical recipes in FORTRAN. The art of scientific computing (Cambridge: University Press, —c1992, 2nd ed.)

Pringle, J. E. 1981, ARA&A, 19, 137

Quillen, A. C. 2006, MNRAS, 365, 1367

Rein, H., & Papaloizou, J. C. B. 2009, A&A, 497, 595

Sackett, P. D. 1999, in NATO ASIC Proc. 532: Planets Outside the Solar System: Theory and Observations, ed. J.-M. Mariotti & D. Alloin, 189

Santos, N. C., Israelian, G., & Mayor, M. 2004, A&A, 415, 1153

Shakura, N. I., & Sunyaev, R. A. 1973, A&A, 24, 337

Shu, F., Najita, J., Ostriker, E., et al. 1994, ApJ, 429, 781

Shu, F. H., Adams, F. C., & Lizano, S. 1987, ARA&A, 25, 23

Tanaka, H., Takeuchi, T., & Ward, W. R. 2002, ApJ, 565, 1257

Terebey, S., Shu, F. H., & Cassen, P. 1984, ApJ, 286, 529

Tsiganis, K., Gomes, R., Morbidelli, A., & Levison, H. F. 2005, Nature, 435, 459

Udry, S., Fischer, D., & Queloz, D. 2007, Protostars and Planets V, 685

Veras, D., Ford, E. B., & Payne, M. J. 2011, ApJ, 727, 74

Ward, W. R. 1997a, Icarus, 126, 261

—. 1997b, ApJ, 482, L211

Weidenschilling, S. J. 1977, Ap&SS, 51, 153

Wetherill, G. W. 1975, in Lunar and Planetary Science Conference Proceedings, Vol. 6, Lunar and Planetary Science Conference Proceedings, 1539–1561

Williams, J. P., & Cieza, L. A. 2011, ARA&A, 49, 67

Winn, J. N. 2011, in IAU Symposium, Vol. 276, IAU Symposium, ed. A. Sozzetti, M. G. Lattanzi, & A. P. Boss, 230–237

Woolfson, M. M. 1993, QJRAS, 34, 1

Wright, J. T., & Gaudi, B. S. 2013, Exoplanet Detection Methods, ed. T. D. Oswalt, L. M. French, & P. Kalas, 489

Wu, Y., Murray, N. W., & Ramsahai, J. M. 2007, ApJ, 670, 820

Zhu, Z., Hartmann, L., Nelson, R. P., & Gammie, C. F. 2012, ApJ, 746, 110